Numerical modelling of plasma-spacecraft charging effect by using particle-in-cell method

by

Shafa Aria

Thesis

for the degree of

Master of Science

Faculty of Mathematics and Natural Sciences
University of Oslo

Sep 2016

Abstract

In this thesis we conduct numerical studies on plasma-spacecraft interactions by examining two different shapes of spacecrafts, a rocket and a satellite. They are simulated by a cylinder and a box corresponding to the rocket and the satellite respectively. We will make use of the DiP3D code developed by Miloch, 2006 with modification to the object handling of the code. Our simulation objects have different dimensions and different shapes and we discover that this has profound impact on the spacecraft. The charging over the spacecrafts turn out to be anisotropic and we retrieve different potential profiles for the two objects. The anisotropic potential results in a dipole electric field which also seems to differ in intensity for the two objects. For the cylinder we yield a stronger electric field in the upstream than in the downstream while in the case of the box the intensity does not seem to differ by much.

Furthermore the study shows agreement with the previous work concerning the temperature ratio and the wake structures forming behind the object. The wake structures in particular seem to depend on the flow and the object dimension as the electrostatic wake structure is also significantly different in the two cases.

We present the problem in the introduction of this thesis and go through the specifications of the object implementation in the main part of the thesis.

To my loved ones.

Acknowledgements

My parents and my sister, without your continuous support and encouragement, this would not have been possible. I love you all. Thank you for being with me through everything that has happened in the past year, all the highs and all the lows.

I would like to express my sincere gratitude to my supervisor, Dr. Wojciech J. Miloch, for his continuous guidance and support throughout this thesis, for his patience, enthusiasm and immense knowledge that radiated through the countless discussions we have had. Thank you for finding the time to guide me when you had no time. You truly are Superman.

I am forever thankful to Dr. Miyake Yohei and Dr. Usui Hideyuki for granting me the opportunity to do my thesis in Japan. The creative ideas and insights that both of you emitted during our discussions is something that I will treasure and look up to forever.

I am thankful for the space physics group for having created such a warm environment with highly skilled, and loving individuals. Thank you Bjørn Lybekk for the technical lessons and for helping me whenever I encountered one technical problem or n technical problems. Thank you Gullik for coming into the office as moral support during the marathon weekends. I appreciate that.

Contents

List of Figures

Chapter 1

Introduction

Space is a very complex environment consisting of charged particles of different species, plasmas, electric and magnetic fields, space-debris, and radiation from external sources, such as cosmic rays that arise from supernovae. All of these can affect a spacecraft and cause significant damage to the spacecraft, its performance and operation lifetime, and in some cases even cause loss of mission which was the recent case for the spacecraft ADEOS II (Cho, 2005) and many others (Bedingfield, Richard D. Leach, and Margaret B. Alexander, 1996). Spacecraft charging is thus a very important aspect of the physics involved and needs to be taken into consideration in the design of a spacecraft, since it can have critical effects on the mission. With the advancements of electronic circuits that operate at low voltage and low current, the study of spacecraft charging has become ever so important resulting in significant development in both theories and simulations to predict and prevent charging effects (Mikaelian, 2009). Furthermore, spacecraft charging can result in modulation of measurements as was the case in the measurements of the Cluster satellites. This is a very important aspect of spacecraft charging and its effect and has been covered both numerically and analytically by Y. Miyake et al., 2013; N. Meyer-Vernet, 1976.

In the following thesis we will delve into the study of the space-environment, how it can affect the spacecraft, the methods that are in use to analyse the problem and finally, analysis of the plasma-spacecraft interactions. More specifically, the numerical method particle in cell (PIC), which we will be using to simulate a system in which a body is submerged in a plasma flow and study the charging of the spacecraft. The object shapes will consist of a cylinder and a box, corresponding to a rocket and a satellite respectively. There are essentially two regions of plasma simulations that are of interest. There is the case in which the object is larger than the Debye length Λ_D at a low voltage and then there is the case in which we concern ourselves to electric probes such as Langmuir probes in which the size of the object is smaller than the Debye length. The size of the objects can range from dust particles (Y. Miyake et al., 2013) to as large bodies as the Moon (Holmström et al., 2012). In the former the sheath that is formed

by the plasma is of the order of the Debye length while in the latter case the sheath will be much smaller than the Debye length and thus are of particular interest when it comes to laboratory experiments. We will confine ourselves to the LEO region of space and we will use the parameters corresponding as close to the region as possible.

The thesis is organised as follows, we will start with the background theory covering the basics of the Earth's space environment from the solar wind to the ionosphere (which is the region of interest for sounding rockets simulations). We will then briefly go through the basics of plasma physics covering the two extreme descriptions of the plasma, namely the fluid description and the kinetic description. Following the kinetic description we then cover the fundamental equations used in plasma physics and how the particles interaction with the electric and magnetic fields change their trajectories. After the section covering plasma physics we will briefly look into orbital mechanics as we will be using the basic equations in this section to calculate velocity from the altitude to be used later as parameter in the simulation. We then get to the theory covering the issue at hand, namely plasma and spacecraft interactions. In the section concerning the plasma spacecraft interaction we will go thoroughly through the theory of the charging mechanism and examine the fundamental regions in which the equations of said charging are valid and their limitations. We will finally go over the different charging processes in the two different regions, LEO and GEO, however in the subsequent chapters we will solely focus on the LEO region.

Having covered the theory, we will delve into the numerical part of this thesis. The method of choice, arguments for using the chosen method, implementation and the used parameters are covered in the first section of the this chapter. In the second section we will cover the results of the simulations with the used parameter and in the subsequent section go through the discussion of the results. Finally we will summarise the results. conclude our observations and analysis, and include thought for future work in the fifth, and final chapter of this thesis.

Chapter 2

Theoretical background

This chapter is meant to lie the foundation for the upcoming chapters. We will look at different space environments and focus on what they consist of. Furthermore we will elaborate the theory and equations that govern these regions of space and their interconnectivity.

We will however not go through detailed calculations and for further theoretical insight into the problems, we refer the reader to the references provided.

2.1 Earth's space environment

Before we thoroughly study the problem of spacecraft charging, we will consider the definitions and constrains in what we here define as the Earth's space environment and the designated subject *space physics*. In the following, space physics is understood as the physics of charged and neutral particles and their interaction with the force fields within the space region of the solar system and its vicinity. Once again when we say particles, we here mean a gas which is composed of atoms, molecules, ions and electrons. The term field here is mainly appointed to the magnetic and electric fields; although the gravitational field is also present, we assume it as a given quantity. Furthermore the electric and magnetic fields will play a much larger role in the coming sections than the gravitational field. There are many regions of interest in space, but we constrain ourselves in which region we would like to study. We do not deal with planetary bodies, moons, planetary rings or interplanetary dust. That would be the domain of planetary science. The same goes for the solar interior, which is evaluated by solar physics (Prölss, 2012). We will also not discuss lower atmospheres of the Earth which would be in the realm of meteorology. In some ways one could say space physics handles the physics that takes place between the field of astronomy and the fields mentioned above (Prölss, 2012).

2.1.1 Electromagnetic radiation from the Sun

The regions of space in part of our solar system is illustrated in fig. 2.1. Important to note here is the charged gas that envelopes the different bodies. Let us break down each region starting from the Sun and down to Earth. Looking at the whole solar system, an interstellar medium comes in contact with the interplanetary magnetic field of the Sun. We refer to this medium as *interstellar wind*, the pressure of the interstellar wind constrains the charged particles and fields of interplanetary space to a finite volume, which we call the *heliosphere*. The boundary of this region is called the heliopause and it defines the border of our solar system. The concepts we have described here (interstellar wind and heliosphere) can similarly also be considered around Earth.

Figure 2.1: Sun-Earth space environment depicting the different regions.

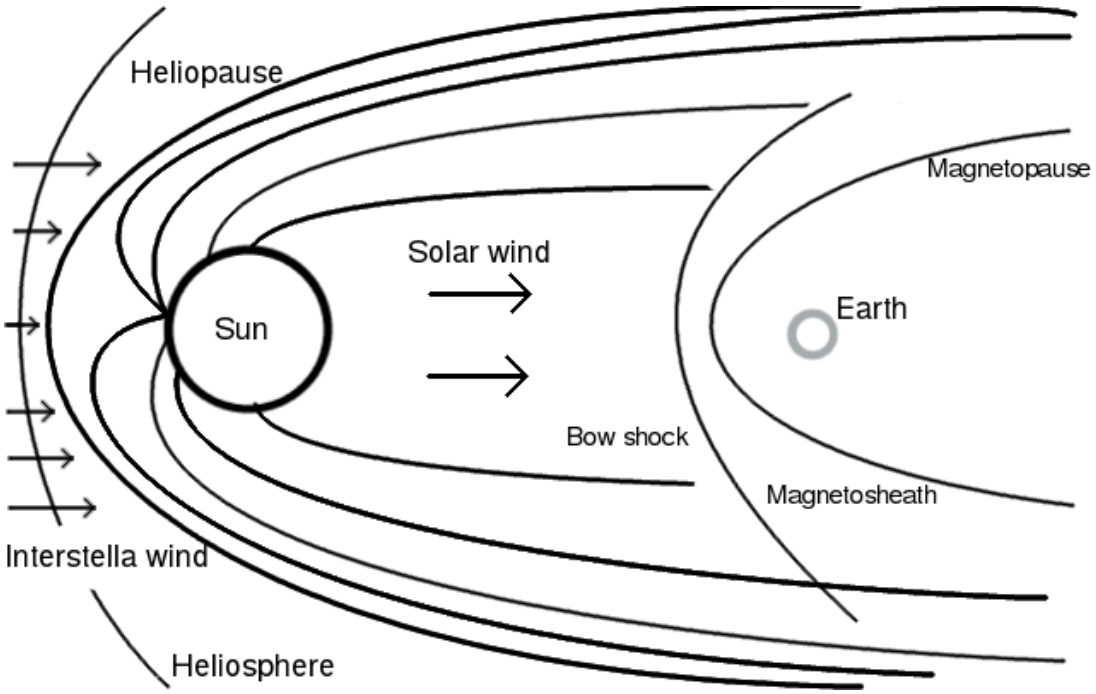

Solar wind

The Sun emits highly conducting fluid at supersonic speeds in the range of $400\,\mathrm{km\,s^{-1}}$ to $800\,\mathrm{km\,s^{-1}}$ (Nicole Meyer-Vernet, 2007) depending on the region of space and the type of emission, into interplanetary space (Baumjohann and Treumann, 1996). We say supersonic when it exceeds the speed of sound, c_s, of the conducting fluid, which is approximately $1.17 \times 10^4\,\mathrm{m\,s^{-1}}$, this usually happens at a certain distance, $r_c \equiv Gm_\odot/2c_s^2$, where $m_\odot$ is the mass of the Sun and G the gravitational constant. This distance is the critical distance from

Figure 2.2: Earth's magnetosphere and radiation belts (Davies, K., Ionospheric Radio, Peter Peregrinus, London, 1990).

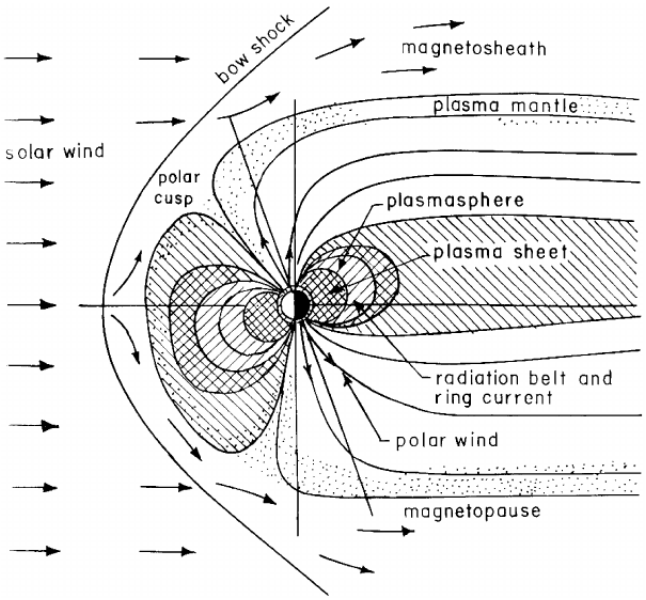

the Sun at which point its speed transcends into supersonic speed (see Brekke, 2013). This highly conducting flow is called the *solar wind* and it is comprised mainly of electrons and ions. As the solar wind propagates and comes in contact with the Earth's magnetic field, it is not stopped, but rather slowed down and deflected around it as shown in fig. 2.2. Through the *frozen in* concept the particles are attached to the magnetic field lines so they cannot just escalate to another magnetic field line such as that of the Earth's. As a consequence of this concept, the Earth's magnetic field is compressed and the particles are slowed down. Since this interaction takes place at such a high velocity, it gives rise to a bow shock, which is a shock wave that occurs at supersonic speeds as in the current case. This, in return, results in the particles being slowed down and their kinetic energy being converted into thermal energy. The region that is formed as a result of this is called *magnetosheath* and is just behind the bow shock region as seen in fig. 2.2. The particle density is higher in this region than in the solar wind (Prölss, 2012).

2.1.2 Earth's magnetic field lines and the atmosphere

Just like in the case of the Sun, we have a region called *magnetopause* which lies between the magnetosheath and magnetosphere. As seen in fig. 2.2 the outer part of the planetary magnetic field is distorted, the interconnection between the interplanetary magnetic field lines and the planetary field lines is complex and we will not go into details as this is not the main topic of this thesis. We

will however note that the front side of the planetary field that faces the Sun is compressed due to the kinetic pressure from the solar wind, while the nightside of it is stretched out far beyond the position of the Earth and into the lunar orbit. This is called the *magnetotail*. Within the magnetosphere, which consists mainly of protons and electrons, is a radiation belt, the *Van Allen belt*, which stretches from $2\,R_\oplus$ to $6\,R_\oplus$ or approximately from 1000 km to 60 000 km. The belt consists of energetic electrons and protons that travel along the field lines of the two magnetic poles and acts as a wall so that it can even halt the most energetic electrons coming in from the Sun. The belt can be divided into inner and outer belts, the former containing more high energy protons usually in the order of and larger than 10 MeV and the latter containing more high energy electrons in range 7 MeV (Mikaelian, 2009). As we have seen there are different regions in space with different properties, the same can be said about the Earth's atmosphere as it consists of several layers.

Atmosphere

When it comes to Earth, we have to distinguish between the different layers of the atmosphere as they too exhibit different properties. The main layers are: Troposphere, Stratosphere, Mesosphere, Thermosphere and Exosphere. While the four former are regarded as the *neutral upper atmosphere* and have a range from 10 km to 600 km, the latter, has range from 600 km to 10 000 km. Which as we can already tell, coincides with the inner Van Allen belt. As the solar UV penetrates the Earth's atmosphere and ionises parts of the neutral atmosphere, collisions of particles become too infrequent and thus result in a permanent ionised region which we refer to as the *ionosphere*, this layer stretches from 80 km to the edge of space well above 900 km.

At high latitudes at around 55° to 90° high energy electrons can precipitate along the magnetic field lines down to ionospheric altitudes and this results in the ionisation of the neutral atmospheric particles. Consequently, because of the transition between the different energy levels, photon emission occurs, which we refer to as the aurorae. The colours of the aurorae depend on the excited constituents and their emission characteristics. At times when there is a strong solar wind, the aurorae will be visible at lower latitudes as well. The ionospheric region is usually densely packed with particles, albeit low energy in comparison to the outer space region where we have high energy, but low density e.g. the outer Van Allen belt. Our region of interest, LEO, as well as the outer region GEO are summarised in fig. 2.3.

The interconnectivity of the fields and the forces of the Earth is very complex and gives rise to many different hazardous regions in space for artificial satellites. We say hazardous because significant damage can be inflicted on the electronic and optical components of the spacecraft, measurements that are conducted might entail induced background noise and spacecraft charging that could

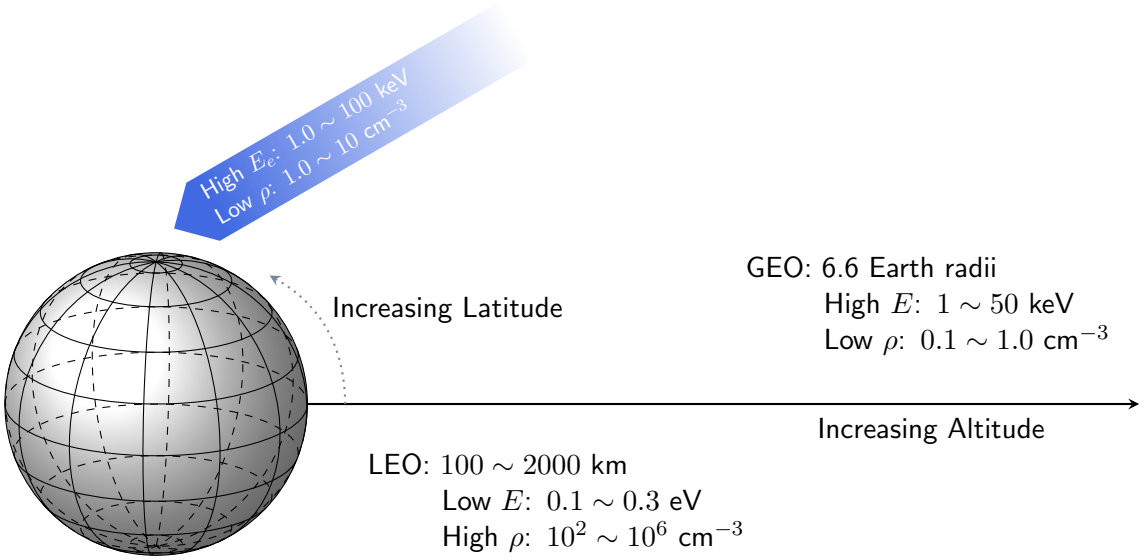

Figure 2.3: Space plasma properties in LEO and GEO.(Inspired by Bedingfield, Richard D. Leach, and Margaret B. Alexander, 1996).

potentially lead to mission failure could occur under substantial radiation. We went through some of the implications the space weather has on Earth's atmosphere, i.e. the affects of solar activities, such as the solar wind and its interaction with the Earth's magnetic fields. A better understanding of the physics behind the kind of interactions we have mentioned could lead us into developing and foreseeing the interactivity between Earth and its surrounding area in space, such as that between the Earth's magnetic field lines and the solar wind.

2.2 Plasma physics

In the previous section we kept referring to the medium that surrounds the Sun and much of the space as charged gas. In this section we are going to define this medium as *plasma*. It is the fourth state of matter and also the most common form of matter in the observable universe. A plasma, as we have seen in the previous section, consists of electrons, ions and neutral atoms, usually at temperatures above 10^4 K. The Sun and stars, Solar wind, Van Allen belts, magnetosphere and the Earth's ionosphere, etc., are all plasmas. In its stationary state it is *quasineutral*, meaning there are roughly the same number of particles within the same volume element with opposite signs (Baumjohann and Treumann, 1996). This quasineutrality will depend on the region of space and parameters as we will be introducing in this section. We will also elaborate on some of the different plasmas and models.

2.2.1 Plasma parameters

Above we mentioned that the quasineutrality will depend on the type of plasma, thus the aforementioned volume element or the confined region of space in which the plasma resides in, must be large enough for sufficient number of particles, yet small enough in comparison to the characteristic length variations of the macroscopic parameters such as temperature and density (Baumjohann and Treumann, 1996). For the macroscopic neutrality to be upheld, the microscopic space charge fields of the individual charge carriers must cancel each other out. The criteria for the neutrality is that the electric Coulomb potential field of every charge, q

$$\phi_C(r) = \frac{q}{4\pi\varepsilon_0 r} \tag{2.2.1}$$

is shielded by other charges in the plasma and takes the form of the *Debye potential*

$$\phi(r) = \phi_C e^{-\frac{r}{\lambda_D}} \tag{2.2.2}$$

where ε_0 is the permittivity in vacuum and

$$\lambda_D = \sqrt{\frac{\varepsilon_0 kT}{e^2 n}} \tag{2.2.3}$$

is called the *Debye length*, where k is the Boltzmann constant, T is the plasma temperature and n is the plasma density. In the above we have assumed that the ions are immobile, if we do include this minor effect then we will get the *effective Debye length*

$$\frac{1}{\lambda_{D,ef}^2} = \frac{1}{\lambda_D^2} + \frac{1}{\lambda_{Di}^2} \tag{2.2.4}$$

where for λ_{Di} we replace the electron temperature and mass with the ion, T_i and m_i (Pécseli, 2012; Baumjohann and Treumann, 1996). Physically the Debye length characterises the shielding distance (Pécseli, 2012). In other words, the distance over which a balance is obtained between the kinetic energy of the particle which tends to perturb the electrical neutrality and the electrostatic potential energy that results from any charge separation which restores charge neutrality. We note that $\phi(r \to \infty) \to 0$ and close to the charge q we retain the Coulomb potential ϕ_C. For the shielding to occur we require that the system be much larger than the Debye length, otherwise there will not be sufficient space for the shielding to occur and we are left with a simple ionised gas.

As we mentioned we require enough space for the shielding to take effect and inside a Debye sphere, a sphere with radius λ_D, the number of particles is given by $\frac{4\pi}{3} n\lambda_D^3$. From this we can deduct a dimensionless number called the *plasma parameter*

$$\Lambda = n\lambda_D^3 \tag{2.2.5}$$

and it plays an important role in classifying plasma conditions of interest. For plasmas of interest we expect $\Lambda \gg 1$ as then it will be hot and dilute. We will come back to this later when we look into the different systems (Pécseli, 2012).

If there happens to be some disturbance on the quasineutrality of the plasma by some external force, the electrons are accelerated to restore the charge neutrality since they are far more mobile than the heavier ions. They will be in motion around the equilibrium position, back and forth, and this results in fast collective oscillations around the more massive ions. This oscillation frequency is the *electron plasma frequency*

$$\omega_{pe} = \sqrt{\frac{ne^2}{m_e \varepsilon_0}} \tag{2.2.6}$$

where m_e is the electron mass. Now that we have introduced the frequency, we can argue that eq. (2.2.3) is valid because $\omega_{pe} \gg \omega_{pi}$, i.e. that there is a time interval where the electrons have reached the isothermal Boltzmann quasi-equilibrium and we can consider the ions as immobile. This is because the time it takes for the electrons to reach the Boltzmann equilibrium is of the order of the Debye length divided by its characteristic velocity, under Maxwellian distribution that would be the thermal velocity $v_{th} \equiv \sqrt{\frac{kT_e}{m}}$ such that $\tau_{pe} \sim \frac{1}{\omega_{pe}}$ and hence $\tau_{pe} \ll \tau_{pi}$ or that the process time for the electrons to reach the equilibrium is far shorter than the ions.

As we outlined before, the ionosphere also contains neutral particles so that if there are frequent charge particles and neutral particles collisions, the electrons will be forced into equilibrium and we will no longer have plasma, but neutral gas. In order for the electrons to remain unaffected the average time between the collisions must be larger than the reciprocal of the plasma frequency.

2.2.2 Single particle motion

Since plasma consists of charged particles, they are heavily affected by the fields and their motion are dependent on it. As referred to earlier, the different plasma regions of space have different properties such as density and temperature. In the limits where the plasma is very dilute, i.e. the particle density is low resulting in fewer particle collisions and where they do not affect the external magnetic field significantly, we can treat the motion of the particles individually. Our problem is then reduced to the motion of charged particles given an initial velocity and position. This approximation is only valid when we can neglect the collective effect of the plasma and when the external magnetic field is much stronger than the magnetic field produced by the charged particle motion i.e. electric current.

Field equations

The equations of motion are basically governed by Newton's second law, $\mathbf{F} = ma$ and the Lorentz force, $\mathbf{F} = q[\mathbf{E} + \mathbf{v} \times \mathbf{B}]$, which is the force experienced by a particle moving in the presence of a magnetic and electric field. For a particle with velocity $\mathbf{v}(t)$, position $\mathbf{r}(t)$ and mass m we have

$$m\frac{\mathrm{d}\mathbf{v}(t)}{\mathrm{d}t} = q[\mathbf{E}(\mathbf{r}(t), t) + \mathbf{v}(t) \times \mathbf{B}(\mathbf{r}(t), t)] \tag{2.2.7a}$$

$$\frac{\mathrm{d}\mathbf{r}(t)}{\mathrm{d}t} = \mathbf{v}(t) \tag{2.2.7b}$$

where $\mathbf{E}$ and $\mathbf{B}$ are the electric and magnetic fields respectively. There is a close relationship between the motion of the charged particles and the fields, even though they are strongly influenced by the fields they are also the source of the fields. This is given by *Maxwell's equations*

$$\nabla \cdot \mathbf{E} = \frac{\rho}{\varepsilon_0} \qquad \nabla \cdot \mathbf{B} = 0 \tag{2.2.8a}$$

$$\nabla \times \mathbf{E} = -\frac{\partial \mathbf{B}}{\partial t} \qquad \nabla \times \mathbf{B} = \mu_0 \mathbf{J} + \mu_0 \varepsilon_0 \frac{\partial \mathbf{E}}{\partial t} \tag{2.2.8b}$$

where $\mathbf{J}$ is the electric current density, ρ, the charge density and finally μ_0 the vacuum permeability. Let us break down the equations. The equation to the left side of 2.2.8a is the Poisson's equation and it expresses that the dielectric displacement lines can begin or end on charges or in other words, the source of the electric field is the electric space charge density $\rho = e(n_i - n_e)$, the difference between the charge densities of ion and electron (Prölss, 2012). The equation to the right of eq. (2.2.8a) is Gauss's law, it expresses among other things that there exists no magnetic monopoles. The divergence of $\mathbf{B}$ is zero also implies that magnetic field lines of finite length close on themselves, and those with infinite length continuing to infinity. This is the case in majority of the physics, however, in some cases such as in tokamak-devices the magnetic field lines continue to wind around a torus with finite surface area (Pécseli, 2012). The left equation of 2.2.8b is Faraday's law of induction and it states that rotation of an electric field is induced by a time-varying magnetic field. Finally, the equation on the right of 2.2.8b is Ampere's law. We see from the equation that the electric current density turns out to be the source for the magnetic field and circles around the current. In cases in which we can ignore the electromagnetic wave propagation we can safely ignore the latter part of the right hand side eq. (2.2.8b). This is because $\varepsilon_0 \mu_0 = c^{-2}$ hence the term will be minimal and can be neglected if no rapid oscillations are present in the system (Baumjohann and Treumann, 1996; Pécseli, 2012).

Particle orbits

Determining the orbits of charged particles in an arbitrary electromagnetic field is very complex, even if the fields are time stationary. Trying to find the trajectories of the particles in space plasma will not be discussed here, we will however look into some simple cases.

$\mathbf{E} \parallel \mathbf{B}$

Let us assume that the electric and the magnetic fields are homogeneous, i.e. $\mathbf{B}$ and $\mathbf{E}$ are constant vectors independent of the time and the spatial coordinate (Pécseli, 2012). If the component of the $\mathbf{E}$, $E_\parallel$, is parallel to the magnetic field then we can have an acceleration in this direction given by

$$\begin{aligned} \mathbf{v}_\parallel &= \frac{q}{m} E_\parallel t + v_{0\parallel} \\ \mathbf{r}_\parallel &= \frac{q}{2m} E_\parallel t^2 + v_{0\parallel} t + r_{0\parallel} \end{aligned} \tag{2.2.9}$$

where $v_{0\parallel}$ and $r_{0\parallel}$ denotes the parallel initial velocity and position respectively. Equation 2.2.9 is derived from the Coulomb force by integrating the equation of motion $m\mathbf{a} = q\mathbf{E}$. The particle remains unaffected by the magnetic field and thus will keep accelerating in the positive direction if it is an ion or in the negative direction if we have an electron.

Now if we assume that there is no electric field component in the direction of $\perp \mathbf{B}$, then the particle will gyrate in a circular orbit with a radius set by the initial velocity. The equation of motion becomes

$$\frac{\mathrm{d}\mathbf{v}_\perp}{\mathrm{d}t} = \frac{q}{m} \mathbf{v}_\perp \times \mathbf{B} \tag{2.2.10}$$

Taking the dot product with $\mathbf{v}$ and noting from vector calculus that $\mathbf{v} \cdot (\mathbf{v} \times \mathbf{B}) = 0$ we obtain

$$m \frac{\mathrm{d}\mathbf{v}}{\mathrm{d}t} \cdot \mathbf{v} = \frac{\mathrm{d}}{\mathrm{d}t} \left(\frac{mv^2}{2} \right) = 0 \tag{2.2.11}$$

Since the force and the displacement are perpendicular to each other, a magnetic field cannot impart energy to a charged particle (Pécseli, 2012). As the equation above states, the kinetic energy and $|\mathbf{v}_\perp|$ are constant. For a particle with constant velocity and a point mass in circular motion of radius R we have an acceleration towards the centre as $\mathbf{a} = \frac{\mathbf{v}^2}{R}$ with its magnitude in the direction perpendicular to the velocity vector. In a homogeneous magnetic field, the charged particle orbit is a circle with radius r_g, the Larmor radius, and an angular frequency ω_g, the cyclotron frequency

$$\omega_g = \frac{qB}{m} \qquad\qquad r_g = \frac{mv_\perp}{qB} \tag{2.2.12}$$

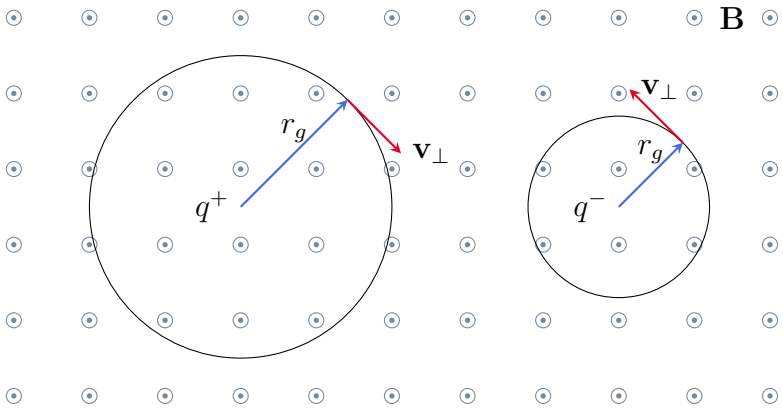

Figure 2.4: Illustration of the direction of rotation of a positive and a negative charged particle with the centre of rotation being the guiding centre.

where $v_\perp$ is the constant speed in the plane perpendicular to $\mathbf{B}$. The direction of rotation of the particle around the magnetic field depends on the charge with the centre of the orbit called the guiding centre as shown in fig. 2.4.

$\mathbf{E} \perp \mathbf{B}$

Now let us look at the case when $\mathbf{E} \perp \mathbf{B}$ as in fig. 2.5 where both fields are constant in space and time. This will be as the two previous cases added together, on one hand you have the electric field accelerating the charged particle and on the other hand you have the magnetic field turning the charged particle around. The equation of motion in this case would be

$$m\frac{\mathrm{d}\mathbf{v}}{\mathrm{d}t} = q[\mathbf{E} + \mathbf{v} \times \mathbf{B}] \tag{2.2.13}$$

In the previous case when there was no electric field the parallel velocity was constant, however now we see that the parallel velocity would be

$$\frac{\mathrm{d}\mathbf{v}_\parallel}{\mathrm{d}t} = \frac{q\mathbf{E}_\parallel}{m} \tag{2.2.14}$$

which when solved, gives us the equation of motion as given in eq. (2.2.9). We initially described the affect of the two fields on the charged particle, we can safely see it implies that the gyro centre moves perpendicular to both fields or in other words, it *drifts*. The perpendicular part of the velocity gives us the equation of motion

$$m\frac{\mathrm{d}\mathbf{v}_\perp}{\mathrm{d}t} = q[\mathbf{E}_\perp + \mathbf{v}_\perp \times \mathbf{B}] \tag{2.2.15}$$

The appropriate frame of reference is the one moving with a constant velocity, $\mathbf{v}_E$, so we shift from our rest frame to this and we write the perpendicular velocity

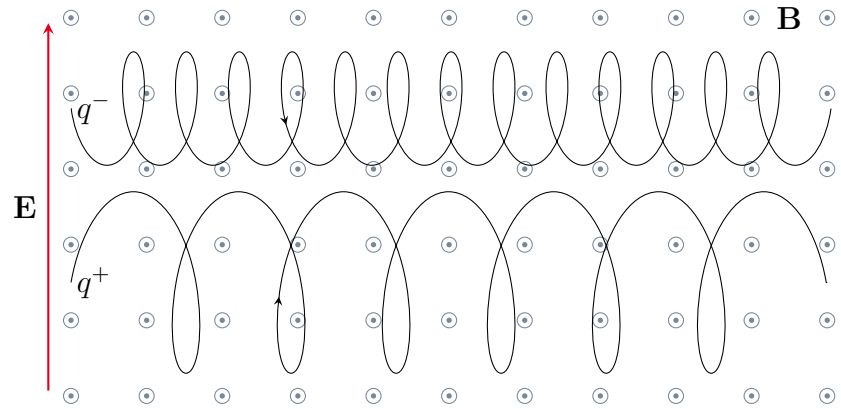

Figure 2.5: Illustration of the $\mathbf{E} \times \mathbf{B}$ drift felt by a negative and a positive charged particle across a constant homogeneous magnetic and electric field.

as $\mathbf{v}_\perp = \mathbf{v}_L + \mathbf{v}_E$ and insert it into the equation of motion 2.2.15, giving us

$$m\frac{\mathrm{d}\mathbf{v}_L}{\mathrm{d}t} = q[\mathbf{E}_\perp + \mathbf{v}_L \times \mathbf{B} + \mathbf{v}_E \times \mathbf{B}] \tag{2.2.16}$$

where $\frac{\mathrm{d}\mathbf{v}_E}{\mathrm{d}t} = 0$ since it's stationary. Now if we choose $\mathbf{v}_E$ in a way that it satisfies

$$\mathbf{E}_\perp + \mathbf{v}_E \times \mathbf{B} = 0 \tag{2.2.17}$$

Then eq. (2.2.16) becomes

$$\begin{aligned} m\frac{\mathrm{d}\mathbf{v}_L}{\mathrm{d}t} &= q[-(\mathbf{v}_E \times \mathbf{B}) + \mathbf{v}_L \times \mathbf{B} + \mathbf{v}_E \times \mathbf{B}] \\ \frac{\mathrm{d}\mathbf{v}_L}{\mathrm{d}t} &= \frac{q}{m}[\mathbf{v}_L \times \mathbf{B}] \end{aligned}$$

which we might notice is the gyration velocity eq. (2.2.10), that describes uniform rotation with Larmor radius r_g and cyclotron frequency, ω_g. The full solution for the motion of the charged particle would then be composed of three parts,

$$\mathbf{v} = \mathbf{v}_L + \mathbf{v}_\parallel + \mathbf{v}_E \tag{2.2.18}$$

the gyration, motion along the magnetic field, and the uniform drift $\mathbf{v}_E$. This uniform drift is called the *E cross B drift* and is given by

$$\mathbf{v}_E = \frac{\mathbf{E}_\perp \times \mathbf{B}}{B^2} \tag{2.2.19}$$

which follows by taking $\times\mathbf{B}$ of eq. (2.2.17) and simplifying. Physically, the magnetic field cannot change the velocity of the charged particle, it is solely affected by the electric field and it accelerates the charged particles in different

direction depending on their charge. Electrons are accelerated towards the negative field direction and ions towards the positive. Since we know that the ions and electrons have different mass, they will also have different velocities (Pécseli, 2012; Baumjohann and Treumann, 1996). In general, the higher the velocity the smaller the radius of the curvature of trajectory and vice versa, as shown in fig. 2.5.

2.2.3 Fluid description of plasma

Now that we have established the parameters we can proceed to the fluid description of plasma. The fluid description of plasma is necessary when dealing with solar physics such as the solar wind medium or generally any plasma system in which the information of individual particles is unnecessary. Typical plasma densities for ion-electron pairs are in the order of $10^{12}\,\mathrm{cm}^{-3}$ (Chen, 1984) and each of these have complicated trajectories as we investigated some of the simple cases in the previous subsection. It would therefore impose an immensely difficult task to follow the trajectories for each of these particles. Accordingly we confine ourselves to macroscopic quantities such as flux, density, temperature and the flow velocity. The plasma frequency eq. (2.2.6) and the corresponding plasma period $\tau_p \equiv \frac{2\pi}{\omega_{pe}}$ is applied to an ensemble of particles and not to individual particles. We will here introduce the various conservation equations for the plasma and the assumptions we have to make to get there. For a more in-depth analysis of the equations here see Fitzpatrick, 2015; Shu, 2009.

Solving Maxwell's equations gives us $\mathbf{B}$ and $\mathbf{E}$ for a given state of a plasma. So in order for us to solve the self-consistent problem we need an equation that gives us the plasma's response to $\mathbf{B}$ and $\mathbf{E}$. The fluid model allows us to have two or more interpenetrating fluids for each species s, such that for an ion and an electron. The fluids would then interact with each other by the generation of the fields $\mathbf{B}$ and $\mathbf{E}$ within themselves even in the absence of collisions as the forthcoming equations will state.

We start off with the *Boltzmann transport equation* (BTE) in tensor form

$$\frac{\partial f_s}{\partial t} + v_i \frac{\partial f_s}{\partial x_i} + a_i \frac{\partial f_s}{\partial v_i} = C_s(f) \tag{2.2.20}$$

where f_s is the distribution function for the specie s, it is the actual distribution of the particles and not the probability of finding said particle in a spatial interval (Pécseli, 2012). $C_s(f)$ is the correlation operator of which the most important one is the collision, hence it is the collision operator for the species s. The subscript inside the argument is omitted because usually the collision term requires the distribution function of each colliding species (Fitzpatrick, 2015).

Since we are dealing with plasma we can denote the acceleration term with the Lorentz force $\mathbf{a}_s = \frac{q_s}{m_s}(\mathbf{E}+\mathbf{v}\times\mathbf{B})$ and thus the flow in the velocity space under the

Lorentz force is incompressible (Fitzpatrick, 2015) and we can rewrite eq. (2.2.20) as

$$\frac{\partial f_s}{\partial t} + \frac{\partial}{\partial x_i}(f_s v_i) + \frac{\partial}{\partial v_i}(f_s a_i) = C_s(f) \tag{2.2.21}$$

since $\nabla \cdot \mathbf{a}_s = 0$. We can then find the continuity equation for the species s by taking the zeroth moment of eq. (2.2.21). In fact, we can find any nth moment of the BTE by multiplying it with $\mathbf{v}^n$ and integrating it over velocity space (Fitzpatrick, 2015). For each moment we will get a new equation, such that the equations leading up to the second moment are given by

$$\frac{\partial \rho_s}{\partial t} + \frac{\partial}{\partial x_i}(\rho_s u_{i,s}) = 0 \tag{2.2.22a}$$

$$\frac{\partial}{\partial t}(\rho_s u_{j,s}) + \frac{\partial}{\partial x_i}(\rho_s u_{j,s} u_{i,s} + P\delta_{ij} - \nu_{ij}) = \rho_s a_j \tag{2.2.22b}$$

$$\frac{\partial}{\partial t}\left(\frac{1}{2}\rho_s |\mathbf{u}|^2 + \frac{3}{2}P\right) + \frac{\partial}{\partial x_i}\left[\frac{1}{2}\rho_s |\mathbf{u}|^2 u_i + u_j(P\delta ij - \nu_{ij}) + \frac{3}{2}P u_i + F_i\right] \tag{2.2.22c}$$

The first one, eq. (2.2.22a), is the continuity equation or the conservation of mass equation. In short, it tells us that the fluid mass at some local point cannot arbitrarily vanish and reappear at a completely different point, it is continuous, see Appendix B. Next, eq. (2.2.22b) tells us that the mean momentum is a result of the external forces applied on the fluid (the right-hand side), the viscosity ν and the pressure forces of the fluid itself P. Finally we have eq. (2.2.22c) the energy conservation equation. We have here introduced an additional term: the conduction heat flux F. The detailed derivation of the conservation energy equation can be found in Bittencourt, 2004; Shu, 2009.

As we have derived the above equations we took the moments of the BTE, so that even though the equations in themselves are exact they unfortunately build a hierarchy of equations that depend on each other, in other words, they are incomplete (Bittencourt, 2004). If we examine eq. (2.2.22a) we see that we can easily solve it once we have the flow velocity, however, the flow velocity is found by solving eq. (2.2.22b), but this again in return delivers us with new unknowns such as the pressure and the viscosity. We can solve this again once we have the solution for the next moment, the energy conservation, eq. (2.2.22c), which depends on the heat flux, requiring us knowing the next higher order moment equation. As we have already implied the equations would just evolve into a higher order moment equation which might very well not have any physical interpretation (Bittencourt, 2004). In order for us to cut the hierarchy at some point we would need to express the higher order equations in terms of some of the lower order equations, i.e. we need to find closure (Fitzpatrick, 2015).

There are two ways this can be done, either by using *truncation schemes* or *asymptotic schemes*. The former is done by either assuming that the higher order moments vanish or prescribed in terms of lower order moments (Fitzpatrick,

2015). The latter is more mathematically demanding and depends on the exploitation of some small parameters such as the ratio of mean-free path between collisions to the macroscopic variation associated with Maxwellian distribution (Chapman-Enskog Closure) see Fitzpatrick, 2015.

2.2.4 Kinetic theory

In the fluid description of plasma we used space and time as independent variables that is to say at an arbitrary point in time t in the vicinity of a position $\mathbf{r}$ we characterised the plasma by its local density ρ, average velocity $\mathbf{u}$ and a temperature T. We assume a priori that the actual velocity distribution of a particle to be Maxwellian within a small volume element (Pécseli, 2012). Due to the long range of Coulomb force, a charged particle can interact simultaneously with other particles despite Debye shielding in effect. Now for plasmas of interest as we have mentioned we would want the plasma parameter to be very large and this in return results in many charged particles within a Debye sphere. The a priori assumption comes from the central limit theorem which states that the distribution of a sum of a large number of statistically independent variables is approximated by such a distribution, but the theorem falls apart when we are dealing with many charged particle interactions that happen simultaneously which are not independent (Pécseli, 2012; Chen, 1984).

As we have elaborated, the fluid description would be inadequate for some applications. To solve it we require an equation that can describe time, space and velocity variations of a distribution function f_s. This equation is nothing more than the BTE in which the right-hand side is omitted yielding us the *Vlasov equation*

$$\frac{\partial f_s}{\partial t} + v_i \frac{\partial f_s}{\partial x_i} + \frac{F_i}{m} \frac{\partial f_s}{\partial v_i} = 0 \tag{2.2.23}$$

where $f_s = f(x_i, v_i, t)$ is the distribution of particles of species s with mass m, in motion under a force field $F_i = F(x_i, t)$.

Maxwell's equations together with the Lorentz force in section section 2.2.2 are used in the following in which we define the density and current density by integrating the distribution function $f_s = f(\mathbf{r}, \mathbf{v}, t)$ over velocity space

$$\rho = \sum_s q_s \int f_s \mathrm{d}^3\mathbf{v} \qquad \mathbf{J} = \sum_s q_s \int f_s \mathbf{v} \mathrm{d}^3\mathbf{v}$$

Where q_s is the charge of the specie s.

We will later revisit the kinetic description when we exploit the numerical methods for simulation.

2.3 Spacecraft plasma interaction

In the previous sections we examined how different regions of space are characterised by different plasma. Some were far from Earth, such as the outer Van Allen belt and some very close to Earth such as the ionosphere and the inner Van Allen belt. Furthermore we introduced what a plasma consists of and how it reacts to the different fields. As the previous sections have shown, the space environment can pose dangers to the spacecraft in various forms among them degrading the electronics on-board and the optics. In order for us to get our spacecrafts operational in the orbit we need to take into account these harsh environments and their effect on our spacecraft. As spacecrafts consist of conducting materials and the plasma is composed of charged particles, we can see that there are many ways things could go wrong if it is not taken into account, and with the recent advancements in sophisticated instruments on board the spacecraft that use low voltage and low current, *spacecraft charging* has become of utmost importance in the development of space missions.

In this section we will establish the different orbits a spacecraft can have and then we will elaborate the different charging effects on the spacecraft in the different space environments such as low Earth orbit (LEO) and geosynchronous equatorial orbit (GEO). We have so far ambiguously used the word spacecraft without specifying what type of spacecraft we can consider. As the different plasma regions of space have different altitudes different spacecraft would need to be designed for the different altitudes and hence, for LEO we can consider spacecraft in the form of sounding rockets and satellites, and in GEO we can exclusively consider satellites. As we will later see the simplifications for the two shapes will come in the form of a cylinder and a box for the rocket and the satellite respectively.

2.3.1 Orbital mechanics

Before studying the plasma spacecraft interactions, let us shortly examine the different orbits obtainable by a spacecraft such as a satellite. The orbit of a spacecraft is crucial as the situation could arise where at one point the spacecraft is in a cold plasma region and at another, it is in a hot plasma region. This should ultimately be taken into account at the design phase of the mission to avoid complications that arise from the different charging processes on the spacecraft giving rise to different surface potential. We will make use of the *orbit equation* derived in detail in Appendix A. We will here only make use of the main points. We can easily derive an equation of motion for two bodies of mass m_1 and m_2, such as that of Earth and a satellite. If we assume an inertial frame of reference with an origin that is moving with a constant velocity, then the position vectors of the two bodies with respect to the origin of the coordinate system are $\mathbf{r}_1$ and $\mathbf{r}_2$. Then, the position vector of m_2 relative to m_1 becomes $\mathbf{r} = \mathbf{r}_2 - \mathbf{r}_1$.

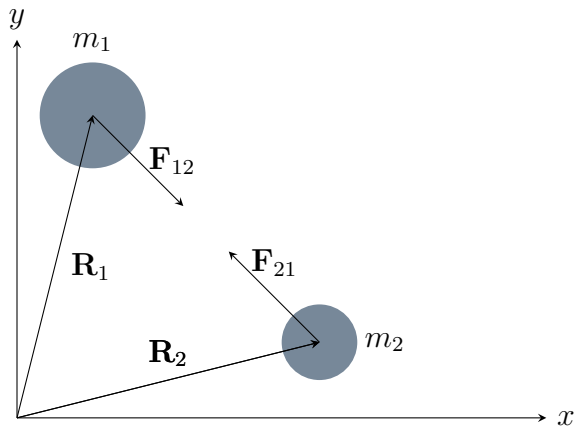

Figure 2.6: Free-body diagram of the two bodies.

We also have the unit vector from m_1 to m_2 as $\hat{\mathbf{u}} = \frac{\mathbf{r}}{\|\mathbf{r}\|}$. We know then from Newton's law of universal gravitation that the force between the two bodies is directly proportional to the product of their masses and inversely proportional to the square of the distance between them. So the force acted on m_2 by m_1 as in fig. 2.6 is given by

$$\mathbf{F}_{21} = -\frac{Gm_1m_2}{\|\mathbf{r}\|^2}\hat{\mathbf{u}} = -\frac{Gm_1m_2}{r^2}\hat{\mathbf{u}} \tag{2.3.1}$$

where G is the gravitational constant and we have the Euclidean norm as $\|\mathbf{r}\| = r$ (Curtis, 2010).

We will use eq. (2.3.1) together with the *specific angular momentum* equation

$$\mathbf{h} = \mathbf{r} \times \mathbf{v} \tag{2.3.2}$$

to arrive at the orbit equation (see appendix A for details)

$$r = \frac{h^2}{\mu}\frac{1}{1 + e\cos(\theta)} \tag{2.3.3}$$

where h is the magnitude of the specific angular momentum, e is the eccentricity and $\mu = G(m_1 + m_2) = Gm_\oplus$ is the gravitational parameter. Taking the derivative of eq. (2.3.3), $\frac{\mathrm{d}r}{\mathrm{d}t}$, and simplifying gives us the radial velocity

$$v_r = \frac{\mu}{h}e\sin(\theta) \tag{2.3.4}$$

The velocity component normal to the position vector is $v_\perp = r\dot{\theta}$, where $\dot{\theta}$ is the rate of change of the true anomaly. We also have the angular momentum $h = rv_\perp$ which we can derive by decomposing the velocity, $\mathbf{v} = v_r\hat{\mathbf{u}}_\mathbf{r} + v_\perp\hat{\mathbf{u}}_\perp$ and position,

$\mathbf{r} = r\hat{\mathbf{u}}_\mathbf{r}$ in eq. (2.3.2) (Curtis, 2010). By using the above relations together with eq. (2.3.3) we get

$$v_\perp = \frac{\mu}{h}(1 + e\cos(\theta)) \tag{2.3.5}$$

Now we let us look at two simple cases of the motions a spacecraft can have from what we have arrived at above.

Circular orbits

For circular orbits the eccentricity e is zero and eq. (2.3.3) becomes

$$r = \frac{h^2}{\mu}$$

However, the derivative of this is zero, $\frac{\mathrm{d}r}{\mathrm{d}t} = 0$. It follows that $v = v_\perp$ and we can use the relations we had above to acquire

$$v_{\text{circular}} = \sqrt{\frac{\mu}{r}}$$

with its period being

$$T = 2\pi\sqrt{\frac{r}{\mu}}$$

Many remote sensing, imagining and navigation satellites occupy nominally circular LEO (Curtis, 2010). At an altitude of 183 km we have velocities at around $7800\,\mathrm{m\,s^{-1}}$. Majority of the weather satellites and communication satellites are in GEO with the advantage that we do not need ground tracking because the orbital period is usually of one sidereal day which is the time it takes for Earth to complete one rotation relative to inertial space (Curtis, 2010). Furthermore, at that altitude most of the Earth's surface is visible and thereby the satellites are able to cover more surface area. Relative speeds in the orbit is around $3000\,\mathrm{m\,s^{-1}}$ at altitudes of circa 36 000 km above Earth's surface.

Parabolic trajectory

In the case of a parabolic trajectory we have $e = 1$ and we retain the orbit equation

$$r = \frac{h^2}{\mu}\frac{1}{1 + \cos(\theta)}$$

When nearing $\theta = 180°$ the denominator goes to zero so that $r \to \infty$. The velocity is then obtained from the *specific orbital energy* $\epsilon = -\frac{\mu^2}{2h^2}(1 - e^2) = \frac{v^2}{2} - \frac{\mu}{r}$ (Curtis, 2010)

$$v_{\text{esc}} = v = \sqrt{\frac{2\mu}{r}}$$

The reason we have written v_{esc} is because if a body is launched in a parabolic trajectory it will drift away into infinity arriving there with zero velocity relative to the reference mass m_1, therefore the velocity is also called the escape velocity.

Sounding rockets are usually launched in a parabolic trajectory with velocities around $1\,\text{km}\,\text{s}^{-1}$ to $2\,\text{km}\,\text{s}^{-1}$ to an altitude of 100 km to 1500 km above the Earth's surface (*NASA Sounding Rockets User Handbook* 2015). Depending on the type of rocket and mission, the rocket may, after reaching apogee, free fall back to Earth or deploy parachute for soft landing to protect the data. This does not mean that the parabolic trajectories are the only form of trajectories the rockets may achieve. As the equations state a spacecrafts trajectory ultimately depends on its velocity.

2.3.2 Sheath theory

Before we proceed further we will first introduce the different concepts in sheath theory such as plasma sheath and the different sheath regions in space that will affect the spacecraft charging differently.

Plasma sheath

Let us first confine ourselves to a one-dimensional model and see what happens to a plasma in the immediate vicinity of vessel wall. When the particles, the electrons and ions, hit the wall they recombine and are thus lost to the plasma so we can treat the wall as a perfect sink of particles (Fitzpatrick, 2015). Since the thermal velocity of the electrons are much higher than the ions we will initially have a large flux of electrons that exceed that of ions. If we start off with an unbiased potential of the wall with respect to the plasma, the imbalance of the flux will give rise to a negatively charged wall. This generates a potential barrier that will then repel the electrons and reduce the influx of electrons. This potential cannot be distributed over the entire plasma and will be confined by Debye shielding to a layer of several Debye lengths, eq. (2.2.3), in thickness (Chen, 1984). We refer to this layer as a *plasma sheath*. Its role is to build up a potential barrier so that the mobile particles, such as the electrons, are confined electrostatically. The process then comes to an end once the height of the sheath is large enough to equal the electron flux to that of ion flux at which point a steady-state is attained (Fitzpatrick, 2015). We can also observe a *pre-sheath* which has a scale larger than the Debye length in which the ions are accelerated by a potential drop $|\Phi| \geq \frac{1}{2}kT_e/e$ to a definitive velocity towards the probe (Chen, 1984).

Sheath regions

As we examined in section 2.1 at low altitudes and LEO the plasma is dense and eq. (2.2.3) gives us a short Debye length in the order of millimetres. This region of space which includes the ionospheric plasma is referred to as *thin sheath regime* and in contrast to this, at higher altitudes where we have sub-storms and high-energy particles making up the hot plasma such as in GEO, we have a *thick sheath regime* (Mikaelian, 2009).

2.3.3 Charging mechanism

In near-Earth orbits many processes can affect the spacecraft ranging from atmospheric pressure, space debris and cosmic rays to eclipses, but from these the most prominent one this thesis is dedicated to is the charging process that arise from geomagnetic storms, radiation belts, eclipses (spacecraft in Earth's shadow during orbit), and solar flares (Mikaelian, 2009). These can result in two types of charging, external and internal (R. D. Leach and M. B. Alexander, 1995). Surface charging is considered external, and dielectric, internal. Both types can lead to electrostatic discharge (ESD) which could potentially harm the instruments and/or lead to mission failure. At present however the latter has been hard to simulate and there are still many challenges to overcome (R. D. Leach and M. B. Alexander, 1995). In this thesis we will confine ourselves to the study of the former, i.e surface charging.

Spacecraft charging occurs when a spacecraft is in a region of space which contains plasma and electric current due to electrons and ions flows to the spacecraft resulting in charge accumulation on the exposed surfaces. The surface can either be a conducting surface or an insulating surface, in the former the charge equilibrium is reached globally while in the latter case it is established on a point-to-point basis. The process is visualised in fig. 2.7 where electrons and ions are shown to be accelerating towards the conducting plate. As the charged particles hit the surface, the charge starts to accumulate on the surface and gives rise to an electric field. This electric field decelerates like-charged particles and accelerates opposite-charged particles thereby increasing the negative or positive current. This accumulation process continues until the charged particles are collected to balance the currents. This continues until charge equilibrium is reached and no more charge accumulates. Since the capacitance is finite the process takes a finite time and at GEO altitudes, it takes a few milliseconds (Henry B. Garrett and A. C. Whittlesey, 2012) to reach equilibrium or as we will soon define it, *floating potential*.

Once it has reached equilibrium we can then apply Kirchhoff's circuit law which states that all currents coming in, equal all currents going out at every node in equilibrium (Mikaelian, 2009). In our case, the surface of the spacecraft can be seen as a node in a circuit in space. This means that the surface potential,

Φ, must be such that the sum of all currents must add up to zero

$$\sum_j I_j = 0 \tag{2.3.6}$$

Where $j = 1, 2, 3 \ldots$ is the counter for the different currents such as the incoming electron current, I_e, incoming ion current, I_i, outgoing secondary electrons current due to the incoming ions or electrons, I_{se} and I_{si} respectively, photoelectron current due to sunlight, I_{ph}, backscattered electron current, I_{bse}, or other forms of current present such that

$$I_{net}(\Phi) = I_e(\Phi) - (I_i(\Phi) + I_{se}(\Phi) + I_{si}(\Phi) + I_{bse}(\Phi) + I_{ph}(\Phi)) = 0$$

where we have Φ as the surface potential relative to the plasma.

Figure 2.7: Surface charging process.

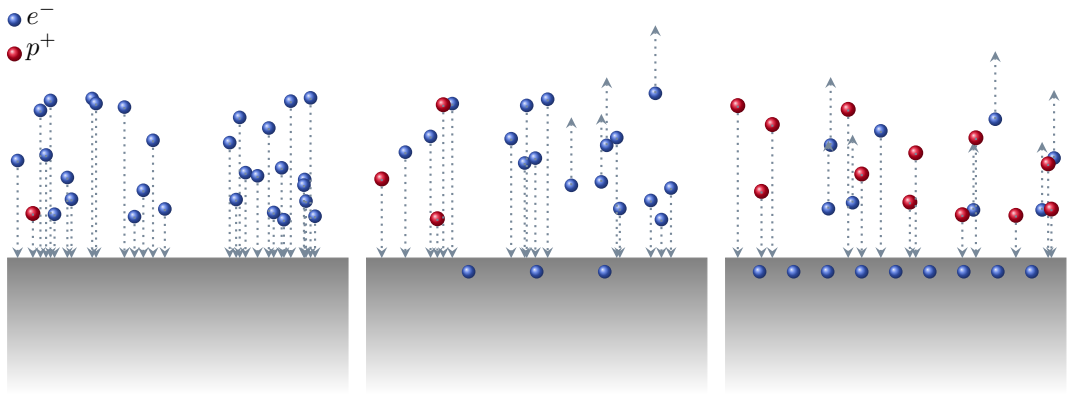

(a) Charing begins **(b)** Charging accumulates **(c)** Equilibrium reached

2.3.4 Langmuir probe theory

As aforementioned in the previous subsection and visualised in fig. 2.7 some electrons will get repelled and some collected by the surface or probe. Now we will look at it in more detail with the Langmuir probe theory in which we will introduce the planar probe and orbit theory for cylindrical probes.

Planar probe

Let us assume we have a strongly magnetised plasma with the plasma potential Φ_p, furthermore we have a probe inside the plasma with a biased potential Φ. Now there are three scenarios we can think of. The first is when the probe is biased to the plasma potential i.e. $\Phi = \Phi_p$. In this case there will be no plasma sheath and the probe is in direct contact with the plasma, so all species of the

charged particles with velocities directed towards the probe will be absorbed by the probe with the electron current being the dominating current since we have a higher flux of electrons than ions. Second, if the biased potential is less than the plasma potential, $\Phi < \Phi_p$, then we will have a scenario as in fig. 2.7 where electrons are reflected, but some electrons do hit the surface so there must be a minimum velocity the electrons must have in order to hit the surface. We can find this $v_{e,\min}$ by conservation of energy

$$\begin{aligned} \frac{1}{2}m_e v_{e,\min}^2 - e\Phi_p &= -e\Phi \\ \frac{1}{2}m_e v_{e,\min}^2 &= e(\Phi_p - \Phi) \\ v_{e,\min} &= \sqrt{\frac{2e(\Phi_p - \Phi)}{m_e}} \end{aligned}$$

All electrons below this velocity are reflected. Lastly, we have the scenario, $\Phi \gg \Phi_p$. In this case, all electrons are absorbed and all ions reflected. In essence, the physical definition of the plasma potential is that a particle at rest has the potential energy $q\Phi_p$ with respect to a suitable defined ground (Pécseli, 2012).

We can now write the current collected by the probe under steady state conditions as

$$I_{ep} = -en\mathcal{A}\int_{v_{e,\min}}^{\infty} u f_e(u)\,\mathrm{d}u \tag{2.3.7}$$

$$I_{ip} = -en\mathcal{A}\int_{0}^{\infty} u f_i(u)\,\mathrm{d}u \tag{2.3.8}$$

where $f_e(u)$ is the electron velocity distribution function and $\mathcal{A}$ is the probe surface area. The ion current is constant as long as we are in the regime, $\Phi < \Phi_p$, however, the current in eq. (2.3.7) will continue to grow due to the expanding sheath region. Thus, it is normal to neglect the ion current in this regime, unless we have $\Phi \ll \Phi_p$. So in order for us to detect the ion current we would need a very large negative probe potential.

Assuming Maxwellian velocity distribution for both the electrons and ions, we can solve the above equations to generate an analytical expression for the probe current contributions I_{ep} and I_{ip} as a function of the probe potential Φ (Pécseli, 2012)

$$I_{ep}(\Phi) = \begin{cases} I_{0,e}e^{-\frac{e|\Phi-\Phi_p|}{kT_e}} & ,\Phi < \Phi_p \\ I_{0,e} & ,\Phi \geq \Phi_p \end{cases} \tag{2.3.9}$$

Similarly for the ion we have

$$I_{ip}(\Phi) = \begin{cases} I_{0,i}e^{-\frac{e|\Phi-\Phi_p|}{kT_i}} & ,\Phi > \Phi_p \\ -I_{0,i} & ,\Phi \leq \Phi_p \end{cases} \tag{2.3.10}$$

Figure 2.8: Illustration of an idealised probe characteristic for a 1D model. Dashed lines are the ion and electron contribution to the total probe current which is depicted by the solid line. Mass ratio of $m_i/m_e = 100$. Taken (from Pécseli, 2012, p.192).

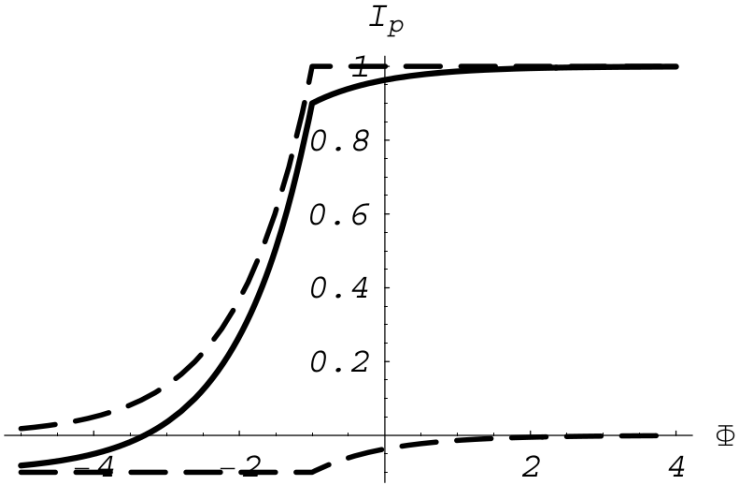

where we have $I_{0,e,i} = \frac{1}{4}\langle|u|_{e,i}\rangle ne\mathcal{A}$ and we also note that we do not necessarily require the same temperature. The total probe current $I_p = I_{ep} + I_{ip}$ can be seen in fig. 2.8 . When we have reached the floating potential, Φ_{fl}, then eq. (2.3.6) is satisfied and the net probe current vanishes. For this to happen we must have less electrons hitting the surface over time as the thermal velocity of the electrons is far greater than that of the ion and thus it has a larger contribution to the probe current compared to the ion. Now if we set the probe potential to the floating potential, $\Phi = \Phi_{fl}$, with respect to the plasma potential then we can find for a Maxwellian velocity distribution

$$\begin{aligned}\frac{1}{4}\langle|u|_e\rangle ne\mathcal{A}e^{-\frac{e|\Phi-\Phi_p|}{kT_e}} &= \frac{1}{4}\langle|u|_i\rangle ne\mathcal{A} \\ |\Phi_{fl}| &= \frac{kT_e}{e}\ln\left(\sqrt{\frac{T_e m_i}{T_i m_e}}\right)\end{aligned}$$

where normally $T_e m_i \gg T_i m_e$. We can use the variation in Φ_{fl} as indicators for variations in Φ_p if we can assume that the sheath regions are in local equilibrium with isothermal electrons (Pécseli, 2012).

In the above derivations and definitions we have assumed steady-state conditions and the criteria of validity of the above is that the wave frequencies are so long that both the ions and electrons have time to propagate through the sheaths with negligible perturbation (Pécseli, 2012) and that the wavelengths of the waves are larger than the probe diameter and sheath combined.

Orbital motion limit theory (OML)

Aside from the simple geometry above we can also derive an analytical solution for a cylindrical probe. We can assume a cylindrical probe with a radius $r_p \ll \lambda_D$ and neglecting the end effects of the probe by considering the probe being very long thereby also neglecting parallel motion along the probe. Let us consider ions with mass m_i moving towards the attracting probe with velocity v_0 from one direction with different impact parameters p such that we can base our derivation in conservation of energy and angular momentum

$$\varepsilon = \frac{1}{2} m_i (u^2 + v^2 + w^2) + q\Phi(r) \tag{2.3.11a}$$

$$L = m_i v_y p \tag{2.3.11b}$$

where we have $\Phi(r)$ as the electrostatic potential valid at $r > r_p$ and for the angular momentum eq. (2.3.11b) we have the velocity component $u = 0$ (Pécseli, 2012).

We have already assumed that the probe is very long and we want the ion velocity w, along the probe, to become immaterial so that we can integrate over it, and this can be satisfied by symmetry as there are no forces along the probe axis (Pécseli, 2012). Using cylindrical geometry gives us

$$\frac{1}{2} m_i v^2 = \frac{1}{2} m_i \left[\left(\frac{\mathrm{d}R}{\mathrm{d}t} \right)^2 + R^2 \left(\frac{\mathrm{d}\theta}{\mathrm{d}t} \right)^2 \right] + q\Phi(r) \tag{2.3.12a}$$

$$m_i v p = m_i R^2 \frac{\mathrm{d}\theta}{\mathrm{d}t} \tag{2.3.12b}$$

where $R = R(t)$ is the particle position with the corresponding velocity v. Using the two above equations eliminating $\frac{\mathrm{d}\theta}{\mathrm{d}t}$ gives for particle entering the sheath

$$\frac{\mathrm{d}R}{\mathrm{d}t} = \frac{v}{R} \sqrt{R^2 \left(1 - \frac{2q\Phi(R)}{m_i v^2} \right) - p^2} \tag{2.3.13}$$

The potential can either be reflecting $q\Phi > 0$ or attracting $q\Phi < 0$. The first term inside the square root $R^2 \left(1 - \frac{2q\Phi(R)}{m_i v^2} \right) > 0$ for a full orbit to exist inside the sheath $r_p < R < r_s$ in order for us to retrieve real values of R (Pécseli, 2012). As we can see the from the equation above there is a minimum distance, r_m, from the particle to the probe, namely when $\frac{\mathrm{d}R}{\mathrm{d}t} = 0$ giving us the impact parameter $p^2 = r_m^2 \left(1 - \frac{2q\Phi(r_m)}{m_i v^2} \right)$ with the velocity determined at $r = r_s$. This again has the condition $r_m < r_s$ as shown in fig. 2.9. For an impact parameter in which the particle marginally avoids collection we have a similar expression

$$p_m^2 = r_p^2 \left(1 - \frac{2q\Phi_p}{m_i v^2} \right)$$

Figure 2.9: Illustration of orbits around a cylindrical Langmuir probe. Figure a) depicts attracting potential while figure b) is the reflecting potential. Taken (from Pécseli, 2012, p.195).

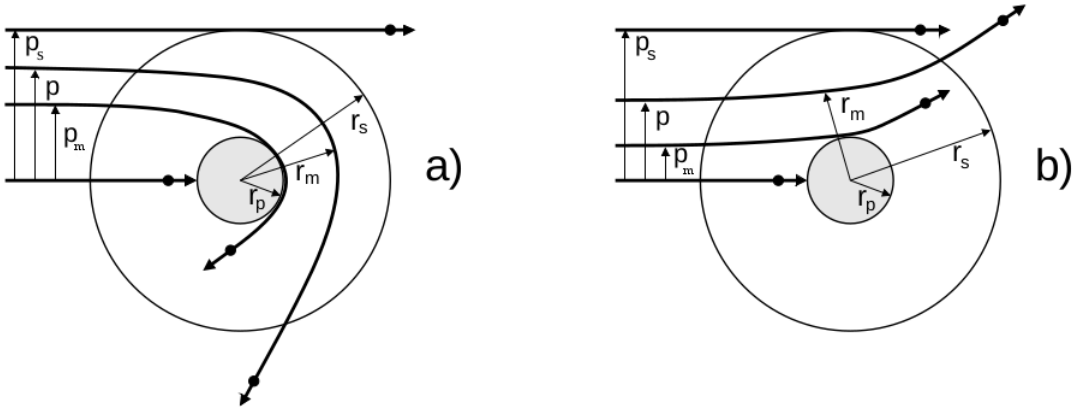

where Φ_p is the probe potential. Ultimately we end up with two scenarios, the reflecting $q\Phi > 0$ fields and the accelerating $q\Phi < 0$. In the former all particles with velocities larger than $\sqrt{2q\Phi/m_i}$ will reach the probe surface. In the latter we have two possibilities which we will denote by the critical velocity v_c satisfying $r_s = p_s$

$$v_c = \sqrt{-2\frac{q\Phi_p}{m_i}\frac{r_p^2}{r_s^2 - r_p^2}}$$

thus, all particles entering the sheath with $v < v_c$ will be absorbed by the probe. If $v > v_c$ we will still have particles reaching the probe surface as long as $p \leq p_m < r_s$, if however $p > p_m$ we will have orbit limitation in which the particles will not reach the surface (Pécseli, 2012).

We can now derive the current equations for the two scenarios. We define the contribution per unit probe length to a long cylinder such as the one in our case in the interval $[v, v + \mathrm{d}v]$ as $\mathrm{d}I = p_m q n v \mathcal{F}(v)\,\mathrm{d}v$ where n is the plasma density and p_m is the cross-section from particle perspective. Furthermore we have the normalised velocity distribution $\int \mathcal{F}(v) = 1$. For the first scenario of reflecting potential the cross section is given by the geometrical cross section and in the following current equation we have omitted the constant factor accounting for the probe surface

$$I(\Phi_p) = nqr_p \int_x^\infty \left(1 - \frac{2q\Phi_p}{m_i v^2}\right) v\mathcal{F}(v)\,\mathrm{d}v \tag{2.3.14}$$

where $x = \sqrt{2q\Phi_p/m_i}$. For the second case we have two terms consisting of the orbital limit and the sheath limit, the latter is when all particles with impact parameter less than r_s reach the probe surface. The current in this case is given

by

$$I(\Phi_p) = nq\left[r_s\int_0^{v_c} v\mathcal{F}(v)\,\mathrm{d}v + r_p\int_{v_c}^{\infty}\left(1-\frac{2q\Phi_p}{m_i v^2}\right)v\mathcal{F}(v)\,\mathrm{d}v\right] \tag{2.3.15}$$

where first integral is the sheath limit contribution and the second one orbit limit contribution (Pécseli, 2012).

Elaborating on where we left, we can consider now a negative biased probe for ion collection in which we assume a two-dimensional Maxwellian distribution outside the probe sheath as (see Pécseli, 2012)

$$\mathcal{F}(v) = \frac{vm_i}{kT_i}e^{-\frac{1}{2}\frac{m_i v^2}{kT_i}}$$

As once again for the first case of reflecting probe we have

$$I_i = -I_0 e^{-\frac{q\Phi_p}{kT_i}}$$

where $I_0 = 2\pi lnq\sqrt{kT_i/(2\pi m_i)}$ and in which we have the surface of the probe as $2\pi r_p l$ with $l \gg r_p$. Integrating eq. (2.3.15) for accelerating probes with $q\Phi_p < 0$ and assuming $r_s \gg r_p$ with $\xi \equiv \frac{q\Phi_p}{kT_i}$ gives us

$$I_i = -I_0\frac{r_s}{r_p}\left(1-\mathrm{erf}\left(\frac{r_p}{r_s}\sqrt{-\xi}\right)\right) - I_0 e^{-\xi}\mathrm{erf}\left(\sqrt{-\xi}\right) \tag{2.3.16}$$

where we have the error-function $\mathrm{erf}(x) = \frac{2}{\sqrt{\pi}}\int_x^{\infty} e^{-y^2}\,\mathrm{d}y$. From this, one can deduce that the collecting area of the probe is different than the geometrical surface area (Pécseli, 2012). For $\xi < -1$ one can simplify this further to

$$I_i = -I_0\sqrt{1-\xi}$$

The corresponding formula for the electron could be arrived at in the same way (see Allen, 1992). One could derive the same equations for a spherical probe which might be practical in some cases where the object sizes are $\ll \Lambda_D$ but it will not be discussed here. For an explicit explanation of the derivations above see Allen, 1992.

The probe theories above was based on the assumption of equal temperature between the electron and ions and that the ions and electrons arrive independently to the probe surface. If we have a case in which the temperature is not the same i.e. $T_i \neq T_e$ we get a negatively charged sheath around the negatively biased probe which will accelerate the ions making them arrive at velocities greater than the acoustic velocity (Chen, 1984). This is the *Bohm sheath condition* for a mathematical analysis of this see Fitzpatrick, 2015; Chen, 1984; Pécseli, 2012.

2.3.5 Charging effects in LEO

Charging in LEO is relatively more complex than the charging that occurs in GEO. For one we have the different layers of the atmosphere that make up LEO and as discussed previously the particles in these layers tend to have different density and energy. For example in ionosphere a significant charging cannot occur, on the other hand, if we increase the latitude we end up in the polar region where it can lead to significant charging on the spacecraft.

The Debye length is very short in these regions giving us thin sheath regime which means the spacecraft potentials are screened more effectively from the surrounding plasma and we will look into some of the implications of these plasma characteristics.

Since the plasma is cold, the effects of the spacecraft motion through the plasma become considerably more important. We cannot ignore the space charge effects here and thus need to solve Poisson's equation $\nabla^2\phi = \frac{\rho}{\varepsilon_0}$ for calculating the potential around the spacecraft.

2.3.6 Charging effects in GEO

Once again in reference to fig. 2.3 and the previous section we see that we are dealing with a region of high energy and low density plasma. The high energy is a result of the geomagnetic substorms, the Debye length as we have seen is also very large in this region stretching several hundred metres (thick sheath regime). We will note a few key differences and approximations in this region.

We can consider the spacecraft as immobile relative to the surrounding plasma, thus the motion of the spacecraft is less important here than in LEO. Concerning the charging, the spacecrafts can become charged up to 10000V during eclipse and as high as 200V in sunlight (DeForest, 1972). Since we are dealing with several hundred metres of Debye length we can safely consider the spacecraft to be small compared to the sheath. In contrast to LEO however, we cannot ignore photoelectron emission by solar UV/EUV. Furthermore we can use Laplace's equation, $\nabla^2\phi = 0$ to solve the potential around the spacecraft as space charge effects can be ignored (Mikaelian, 2009). The charging of both LEO and GEO are depicted in fig. 2.10

Figure 2.10: From LEO to GEO worst case surface charging hazard level for spacecrafts in the designated altitude and latitudes. Colourised, courtesy of (A. Whittlesey, H. B. Garrett, and Robinson, 1992).

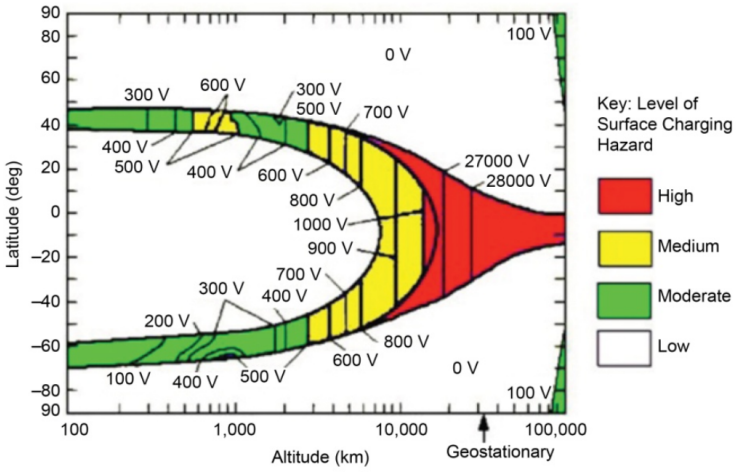

Chapter 3

Methods

In this chapter we will examine the numerical approach for some of the concepts in the previous chapter, the kind of models we have for the fluid description and kinetic description and why one is preferred over the other. We will however mostly focus on the *particle-in-cell* method, which is the main method for our spacecraft-plasma simulation.

In the previous chapter we introduced the different space environments and the different plasma regions. Naturally, we will here introduce the parameters for our simulations, the DiP3D code and the implementation of the spacecrafts in the code.

3.1 Numerical models

In the following section we will introduce the different models used in the different plasma simulations such as MHD and ES, their strengths, their weaknesses and which one we choose to use in our simulation and why.

We have already previously introduced the theoretical background and which equations governs the plasma, namely Maxwell's equations (see section 2.2.2), to which the fields are related to the charge and current density

$$\rho = \sum_{i=1}^{N} \frac{q_i}{V} \tag{3.1.1a}$$

$$\mathbf{j} = \sum_{i=1}^{N} \frac{q_i \mathbf{v}_i}{V} \tag{3.1.1b}$$

in a small mesh cell V with N particles with charge q_i and velocity v_i where $i = 1, \ldots, N$. Combined with the Lorentz force, $\mathbf{F} = q(\mathbf{E} + \mathbf{v} \times \mathbf{B})$, gives us the equations of motion eqs. (2.2.7a) and (2.2.7b). We rewrite the above equations

here for convenience

$$\nabla \cdot \mathbf{E} = \frac{\rho}{\varepsilon_0} \tag{3.1.2a}$$

$$\nabla \cdot \mathbf{B} = 0 \tag{3.1.2b}$$

$$\nabla \times \mathbf{E} = -\frac{\partial \mathbf{B}}{\partial t} \tag{3.1.2c}$$

$$\nabla \times \mathbf{B} = \mu_0 \mathbf{J} + \mu_0 \varepsilon_0 \frac{\partial \mathbf{E}}{\partial t} \tag{3.1.2d}$$

and the corresponding equations of motion

$$m \frac{\mathrm{d}\mathbf{v}_i}{\mathrm{d}t} = \mathbf{F} \tag{3.1.3a}$$

$$\frac{\mathrm{d}\mathbf{r}_i}{\mathrm{d}t} = \mathbf{v}_i \tag{3.1.3b}$$

A full blown three-dimensional simulations of the above system of equations would require a computer with a high-level computational capacity and the computational time to simulate a realistic scenario would be too long for most purposes (Hockney and Eastwood, 1988). It is thus necessary to develop approximations for the above system of equations by either using a fluid model such as *magnetohydrodynamics* (MHD) or a kinetic model such as the electro static approximation (ES). We will now look into these two extreme cases in more detail and in both cases assume timescales much larger than the time it takes light to travel across the system, this assumption allows us to eliminate electromagnetic waves (by ignoring second term in eq. (3.1.2d)) in the system and consequently implies that **E** and **B** fields adjust themselves instantaneously to the present distribution of charges and currents (Hockney and Eastwood, 1988).

3.1.1 Magnetohydrodynamics

Here we will present a model for the dynamics of a fully ionised plasma, the type of plasma found for example in the ionosphere. This model as the name hints, assumes the plasma as a medium which follows the fundamental laws of any other continuum and hence is subject to equations such as Navier-Stokes, and the continuity equation. This model is often *single-fluid model* i.e. we ignore that there are two different species and instead see it characterised as one conductive medium (Pécseli, 2012).

In this approximation we consider a low density and low frequency plasma in which the space scales are much larger than the Debye length and we can assume charge neutrality and thereby ignore the right-hand side of eq. (3.1.2a) eliminating the mechanism for plasma oscillations and the resulting high frequencies related to them. In other words, we can regard the MHD plasma as a neutral

fluid through which current flows (Hockney and Eastwood, 1988). Furthermore the system is dominated by currents and the magnetic forces upon them and the magnetic fields are large and imposed. From eq. (3.1.2d) the currents in the fluid themselves produce magnetic fields while the electric field arises from the induction effect from the time variation of $\mathbf{B}$. From the above we can summarise the equations to the much simplified version

$$\begin{aligned}\boldsymbol{\nabla}\cdot\mathbf{B} &= \boldsymbol{\nabla}\cdot\mathbf{E} = 0\\ \boldsymbol{\nabla}\times\mathbf{E} &= -\frac{\partial\mathbf{B}}{\partial t}\\ \boldsymbol{\nabla}\times\mathbf{B} &= \mu_o\mathbf{B}\end{aligned}$$

The Lorentz force can be changed in terms of the conductivity σ (Hockney and Eastwood, 1988) to

$$\mathbf{j} = \sigma[\mathbf{E} + \mathbf{v}\times\mathbf{B}]$$

where $\mathbf{v}$ is the bulk velocity, but if we assume that the conductivity is high and $\mathbf{j}$ is finite then the above can be simplified to

$$\mathbf{E} + \mathbf{v}\times\mathbf{B} = 0$$

If we now use eq. (3.1.2c) in combination with the above we retrieve the condition

$$\boldsymbol{\nabla}\times(\mathbf{v}\times\mathbf{B}) = \frac{\partial\mathbf{B}}{\partial t}$$

which tells us that the magnetic flux is constant through any surface moving with the velocity $\mathbf{v}$ of the fluid i.e. the magnetic lines of force are "frozen into" and thus constrained to move with the fluid (Hockney and Eastwood, 1988).

We can complete the MHD equations by including the Navier-Stokes equation and the continuity equation (Pécseli, 2012)

$$\frac{\partial\rho}{\partial t} = -\boldsymbol{\nabla}\cdot(\mathbf{v}\rho) \tag{3.1.4a}$$

$$\rho\frac{\mathrm{D}\mathbf{v}}{\mathrm{D}t} = -\boldsymbol{\nabla}p + \mathbf{j}\times\mathbf{B} \tag{3.1.4b}$$

Where we have made use of the hydrodynamic derivative $\frac{\mathrm{D}}{\mathrm{D}t} \equiv \frac{\partial}{\partial t} + \mathbf{v}\cdot\boldsymbol{\nabla}$ where ρ is the mass density and p is the pressure which is related to the density by $\frac{p}{\rho^\gamma}$ = constant in which γ is the ratio of specific heat at constant pressure to that at constant volume (Hockney and Eastwood, 1988).

The MHD equations described above are usually solved by finite-difference method, which is well described in Jardin, 2010. The MHD model can further be expanded to the *two-fluid MHD* in which we have to treat the ion and electron momenta separately because of the non-negligible Hall electric field. This, among other approximations within the MHD model are described in Jardin, 2010.

The MHD model can either be used as a stand-alone or as a hybrid model together with its kinetic counterpart for simulation. The former is used in simulation of fusion machines while the latter has applications within astrophysics and space-physics e.g. the solar wind interaction with the Earth's magnetic dipole (Hockney and Eastwood, 1988).

3.1.2 Electrostatic model

On the other end of the spectrum we have the electrostatic model (ES) which involves individual particles and which deals, contrary to MHD, with plasma frequency and length scales of the order of the Debye length. The physics in this model consists of essentially two parts, the fields that are produced by the individual particles and the motion produced as a consequence of the fields (Hockney and Eastwood, 1988). As before, the fields are calculated by Maxwell's equations and the motion caused by the forces is found by the Newton-Lorentz equation of motion (Birdsall and Langdon, 2004).

As a result of the above we can now no longer ignore the charge separation that can arise and we therefore retain the right-hand side of eq. (3.1.2a). However, the currents in this model are presumably small and thus we can set the right-hand side of eqs. (3.1.2c) and (3.1.2d) to zero, thus reducing the equations to (Hockney and Eastwood, 1988)

$$\begin{aligned} \boldsymbol{\nabla} \cdot \mathbf{E} &= \frac{\rho}{\varepsilon_0} \\ \boldsymbol{\nabla} \cdot \mathbf{B} &= 0 \\ \boldsymbol{\nabla} \times \mathbf{B} = \boldsymbol{\nabla} \times \mathbf{E} &= 0 \end{aligned}$$

retaining the definition of ρ as described in section 3.1, namely charge density. From electromagnetism we can now introduce the electrostatic potential

$$\mathbf{E} = -\boldsymbol{\nabla}\phi$$

such that

$$\boldsymbol{\nabla} \cdot \mathbf{E} = -\boldsymbol{\nabla} \cdot \boldsymbol{\nabla}\phi = -\nabla^2\phi$$

We have thereby reduced Maxwell's equations to the one above, *Poisson's equation*. The equations for the fields in this model are thus

$$\nabla^2\phi = -\frac{\rho}{\varepsilon_0} \tag{3.1.5}$$

$$\mathbf{E} = -\boldsymbol{\nabla}\phi \tag{3.1.6}$$

$$\rho = \sum_i \frac{q_i}{V} \tag{3.1.7}$$

as for the motion we use the Newton-Lorentz force, only that we retain $\mathbf{B}_0$ as a fixed external magnetic field

$$m_i \frac{\mathrm{d}\mathbf{v}_i}{\mathrm{d}t} = q_i[\mathbf{E} + \mathbf{v}_i \times \mathbf{B}_0]$$
$$\frac{\mathrm{d}\mathbf{r}_i}{\mathrm{d}t} = \mathbf{v}_i$$

As we have mentioned the model follows the trajectories of the individual particles, it is therefore very well suited for particle-mesh simulations. Among the applications it is well fitted for the study of the diffusion of plasma across a strong magnetic field (Hockney and Eastwood, 1988). For a more in-depth analysis of this model and development see (Birdsall and Langdon, 2004).

3.1.3 Interacting systems

We will briefly examine the two different systems, *strongly coupled system* and *weakly coupled system* and why the later is preferred for our simulation.

Let us imagine a box with length of a Debye length, λ_D. Furthermore we now assume we can measure the local electric field in one spatial position where at each point of the box the electric field is the superposition of the contribution of each particle. Now if our box has few particles in it that are in constant motion we will notice that our measurements will be very jumpy and since we are measuring one specific point, we can see that on average there will be very few particles coming towards or away from our measurement point. We would thereby only measure strong effects when a particle is nearby as opposed to far away from our measurement point. The same argument could be used for the particles themselves, in other words, there would only be a jump in the trajectory of the particle when a close encounter with another particle has taken place, i.e. a collision. This is what we would call a *strongly coupled system*. In summary we can say a strongly coupled system is one in which there are few particle interactions, particle motion is determined by near neighbour interaction and in which the Boltzmann and Klimontvich equations are valid (Lapenta, 2016; Lyu, 2014).

For plasmas of interest we would like the plasma parametre Λ, eq. (2.2.5) to be very large, as opposed to strongly coupled systems (in which Λ is small). If that is the case then we have a *weakly coupled system*. This system is characterised by an extremely large number of particles in which at any given point, the number of particles contributing to the electric field is very large (Lapenta, 2016). As we would anticipate, by simply averaging the effects of all the particles contributing to the measurements, the results would come out as smooth and not jumpy. The same applies to the trajectory of a particle, since at any time the particle is affected by a large number of other particles. Thereby the trajectory would come out as smooth and without jumps. As we have introduced, we could say

that one of the main differences between a weakly coupled system and a strongly coupled system is the mean field approximation. In summary a weakly coupled system is one in which the motion of a particle is largely determined by the collective behaviour of the other particles, many particle interactions, mean field approximation is used and that the Vlasov equation is valid (Lapenta, 2016).

3.1.4 Simulation methods

For the two systems we have described in section 3.1.3 we can implement two different types of simulation models. For a strongly coupled system we would rely on the *particle-particle* (PP) approach, which describes the motion of N particles by conjoining Newton's equations for each of the N particles taking as a force acting on the particle by the sum of the effect of all the other particles.

Discretisation can be done by having a small time step Δt chosen such that the particle is moved only a small distance by computing the position and velocity of the particle and after each move the force is recomputed and a new move is made for the particle. In three dimension we could write this as

$$\mathbf{r}_{i+1} = \mathbf{r}_i + \Delta t \mathbf{v}_i$$
$$\mathbf{v}_{i+1} = \mathbf{v}_i + \Delta t \mathbf{F}$$

where $\mathbf{r}$ is position and $\mathbf{v}$ the velocity of the particle. As we have mentioned before, we would need to do the force calculation for N particles. This is the main cost of the computation, which requires to sum over all the particles in the system, with $\mathbf{F}$ being

$$\mathbf{F}_n = \sum_m \mathbf{F}_{nm}$$

where $\mathbf{F}_{nm}$ is the interaction force between two particles n and m. This model is widely used in molecular dynamics and bimolecular studies. The number of terms to sum to compute the force for each particle is $N-1$, but since we have N particles and only need to compute the force once for each pair we get $N(N-1)/2$. The cost is thus $\propto N^2$ and scales badly as N increases. We can now see why this is a very unfavourable approach to use in a weakly coupled system where we have an extremely large number of particles to compute the force of. Fortunately there is a better way.

The other model is to make us of the particle-mesh (PM) method. In this model we exploit the force-at-a-point formulation and make use of the field equations for the potential e.g. Poisson's equation and the potential energy field. This will result in less computation time, but also lower resolution (Hockney and Eastwood, 1988) than PP method.

We represent here the physical values approximately on a regular array of mesh points and replace the differential operators such as the laplacian with a numerical approximation for differentials such as finite-element or finite-difference

method on the mesh (Hockney and Eastwood, 1988). The essential difference between the PP and PM method lies in the calculation of the forces. The force calculation of a charged-particle can be divided into three steps as (Hockney and Eastwood, 1988)

1. Assign charge to mesh
2. Apply Poisson solver on the mesh
3. Compute forces from the mesh-defined potential and interpolate the forces at particle positions.

The first and last step have operation counts equal to that of the number of particles involved in the calculations while the second one depends on various factors such as the number of mesh points and the particular form of PM scheme. For a detailed comparison between the two methods see Hockney and Eastwood, 1988, chap.1-5-2.

Between the two methods above the one used extensively for the studies of a weakly coupled system is a particular form of PM, the *particle-in-cell* method. We will elaborate on it in the next section, but here we will outline that we make use of a cloud of charged point particles to diminish the close encounter force experienced by each particle and thereby greatly reducing collisions rate. The particles at small distances is corrected by a potential resembling the Coulomb potential. As we mentioned in section section 3.1.3 a weakly coupled system will have smooth measurements. In this case, however, it is not because that a very large number of particles will average each other, but rather that effect of the few particles near the measurement point is weak. Similarly, the trajectories are smooth because the few near neighbours produce weak interactions and not because each particle is surrounded by a vast number of particles.

To sum up this section we can visualise the choice of methods by looking at fig. 3.1 summarising the models by frequency level. At high frequencies we would be dealing with electron plasma frequency while at the lower frequency level we have the electron-ion collision frequency

Figure 3.1: Simple diagram depicting choice of models.

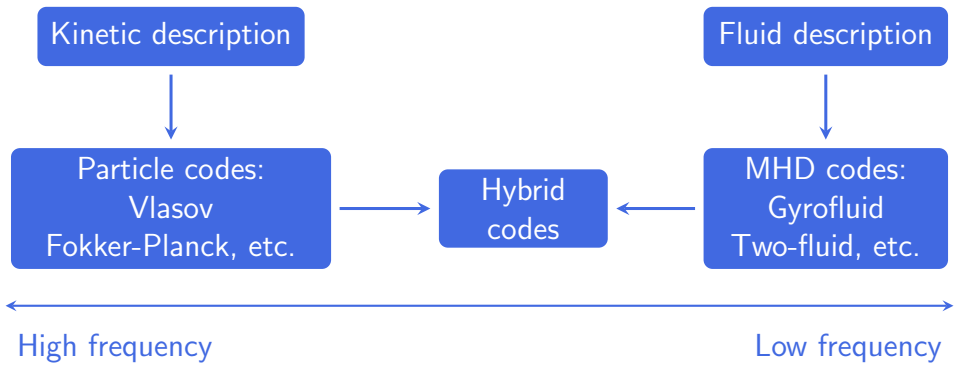

3.2 PIC

In this section we will go more in-depth in the PIC method and see how it is implemented. We will take a look at how the equations in section 2.2 are conjoined with the Vlasov equation and its numerical approach as well the implementation and algorithm.

We have here introduced the general cycle of PIC in fig. 3.2 and we will in this section go through each node in the cycle in depth and then shift our focus to the DiP3D code in the coming section.

Figure 3.2: A general PIC cycle, one time step. Here, $n = 1 \dots N_p$ is the number of particles and i, j, k are the grid indices.

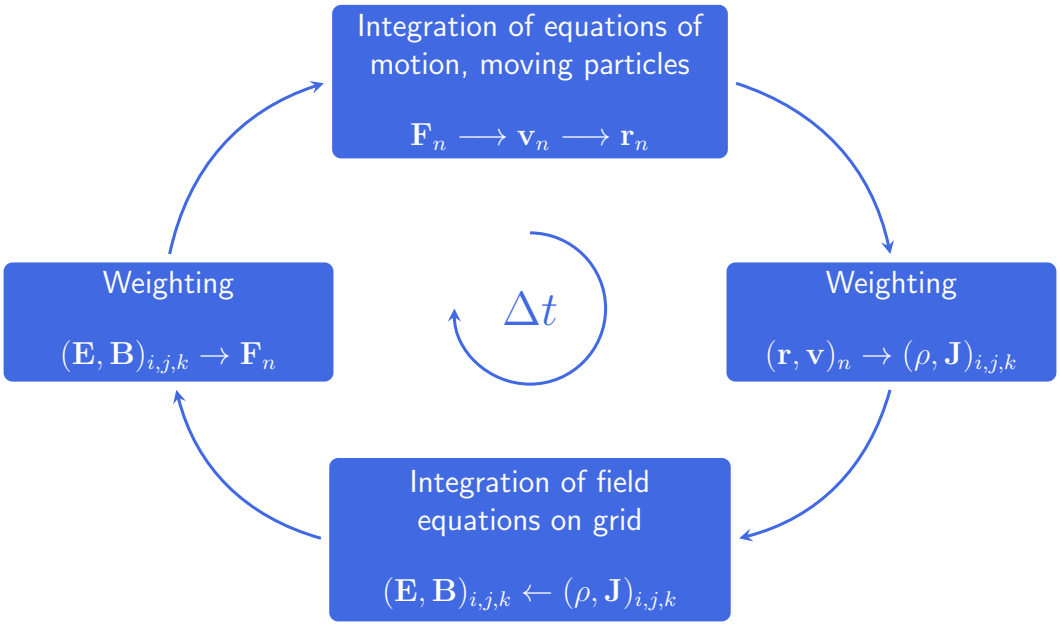

The foundation of the PIC method lies in utilising the full set of Maxwell's equations together with the Vlasov equation described in section 2.2.4.

3.2.1 Fininte-size particles

Newtonian mechanics tells us that two particles will always feel force between each other, but opposite direction and depending on the distance the force will be varying in strength. If the particles pass each other, each will feel a large force when they are close to each other. Impulses associated with such a close encounter give rise to the collisional effects, on the other hand, once they have passed the force will fall off with distance. In the latter region where the force falls off the particles can interact simultaneously and this is the region of interest for our simulation (Dawson, 1983). Thus we wish to diminish the close encounter

Figure 3.3: Coulomb force experienced by particles in two and three dimensions. (From Dawson, 1983).

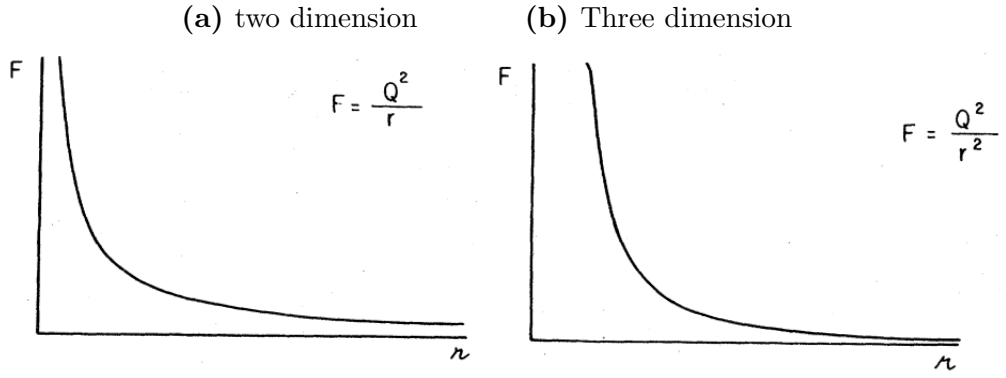

force such that we can achieve a force behaviour as in fig. 3.4. This is done with the concept of *super-particles*. A super-particle is a cloud of charge point particles which are free to pass through each other. As in figs. 3.3a and 3.3b the force is Coulombic when they are far apart, but when they get close the force starts to drop off and it will be zero when the particles are exactly on top of each other (Dawson, 1983; Birdsall and Langdon, 2004; Lapenta, 2016). For the computational particles that we have now described above, we would

Figure 3.4: Two-dimensional graph depicting the force experienced between finite-sized particles of various lengths. (From Dawson, 1983).

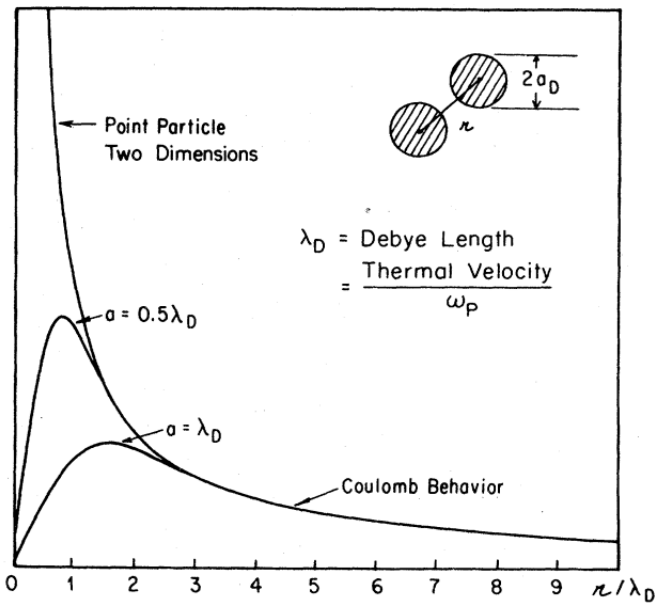

need grid spacing of the order of the super-particles since their charge is smeared

over a region of a finite space, and density variations cannot be resolved for regions smaller than the size of a particle (Dawson, 1983) we would need grid spacing about equal to the size of the particle, in other words $\Delta x \approx \Delta p$. Since computationally we are using fewer particles than the physical system, it will result in reducing the potential energy for the kinetic energy. The consequence is that correct coupling parameter is achieved by fewer particles interacting more weakly (Lapenta, 2016).

Now from the above we can write out the phase space distribution function as a sum of super-particles, i.e. the distribution function of each species is given by the superposition of several super-particles:

$$f_s(\mathbf{r}, \mathbf{v}, t) = \sum_p f_p(\mathbf{r}, \mathbf{v}, t)$$

For each super-particle there will be assigned a specific functional form for its distribution. The functional form will contain several free parametres whose time evolution will then determine the numerical solution of the Vlasov equation. The free parametres in question will then acquire the physical meaning of position and velocity of the super-particle p:

$$f_p(\mathbf{r}, \mathbf{v}, t) = N_p S_{\mathbf{r}}(\mathbf{r} - \mathbf{r}_p(t)) S_{\mathbf{v}}(\mathbf{v} - \mathbf{v}_p(t))$$

where $S_{\mathbf{r}}$ and $S_{\mathbf{v}}$ are the shape functions for the super-particles and N_p is the number of physical particles that are present in the element of phase space represented by the super-particle (Lapenta, Brackbill, and Ricci, 2006; Dawson, 1983). For the shape functions there are several properties of which not all are required.

- The support of the shape function is compact, in other words it is zero outside a small range.
- The integral results in unity:

  $$\int_{-\infty}^{\infty} S_\xi(\xi - \xi_p) \mathrm{d}\xi = 1$$

  where ξ is any coordinate in the phase space.
- Favour of symmetry $S_\xi(\xi - \xi_p) = S_\xi(\xi_p - \xi)$

In the normal PIC method one usually chooses the velocity space shape functions to be Dirac's delta

$$S_{\mathbf{v}}(\mathbf{v} - \mathbf{v}_p) = \delta(\mathbf{v} - \mathbf{v}_p)$$

This will have the advantage that the super-particles describing the particles within the element of phase space have the same speed and thereby remain closer

in phase space during the subsequent evolution, i.e. spatial shape function remains constant in time (Lapenta, Brackbill, and Ricci, 2006).

The spatial shape function makes use of b-splines. These are given by b-splines of some order l

$$b_{l+1}(\xi) = \int_{-\infty}^{\infty} b_0(\xi - \xi')b_l(\xi')\mathrm{d}\xi'$$

such that for a grid with spacing Δx in the direction x we could have $S(x - x_p)b_l[(x - x_p)/\Delta x]$, equivalently in the other directions (Lapenta, Brackbill, and Ricci, 2006). The *first-order* b-spline is given by

$$b_l(\xi) = \begin{cases} 1 - |\xi| & \text{if} \quad \xi < 1 \\ 0 & \text{otherwise} \end{cases}$$

which is the *cloud-in-cell* (CIC) and ξ is some arbitrary coordinate in phase space. Generalising the above case the spatial shape function can be written as

$$S_{\mathbf{r}}(\mathbf{r} - \mathbf{r}_p) = b_l\left(\frac{\mathbf{r} - \mathbf{r}_p}{\Delta p}\right) \tag{3.2.1}$$

where Δp is the size of the super-particle or as we mentioned is more or less equal to the grid spacing in either direction e.g. Δx (Lapenta, Brackbill, and Ricci, 2006). For a more elaborate study on this topic see see Hockney and Eastwood, 1988, chap. 5. In fig. 3.5 we have plotted the first three shape functions.

3.2.2 Integration of the equations of motion

The choice of a scheme for the particle mover is perhaps one of the most crucial aspects of the simulations. Let us imagine a problem in which 100000 particles may have to be run for 10000 time steps, this means the equations of motion must be integrated 10^9 times. That will require a lot of computation time and thereby running such a program on a rented supercomputer can quickly become costly if one does not consider the right scheme (Birdsall and Langdon, 2004).

There are two type of schemes: *explicit* and *implicit*. In an implicit scheme we would calculate the particle velocity from an already calculated field while in an explicit scheme we use only the old force from the previous time. The later scheme is thus faster and simpler, but requires smaller time-step (Δt). Schemes like the Runga-Kutta family of methods are implicit and therefore not suited for our problem at hand. Among the explicit methods, the *Leapfrog method* and the *Boris method* are the most frequently used ones and these are the ones we will inspect.

Figure 3.5: The three first b-splines.

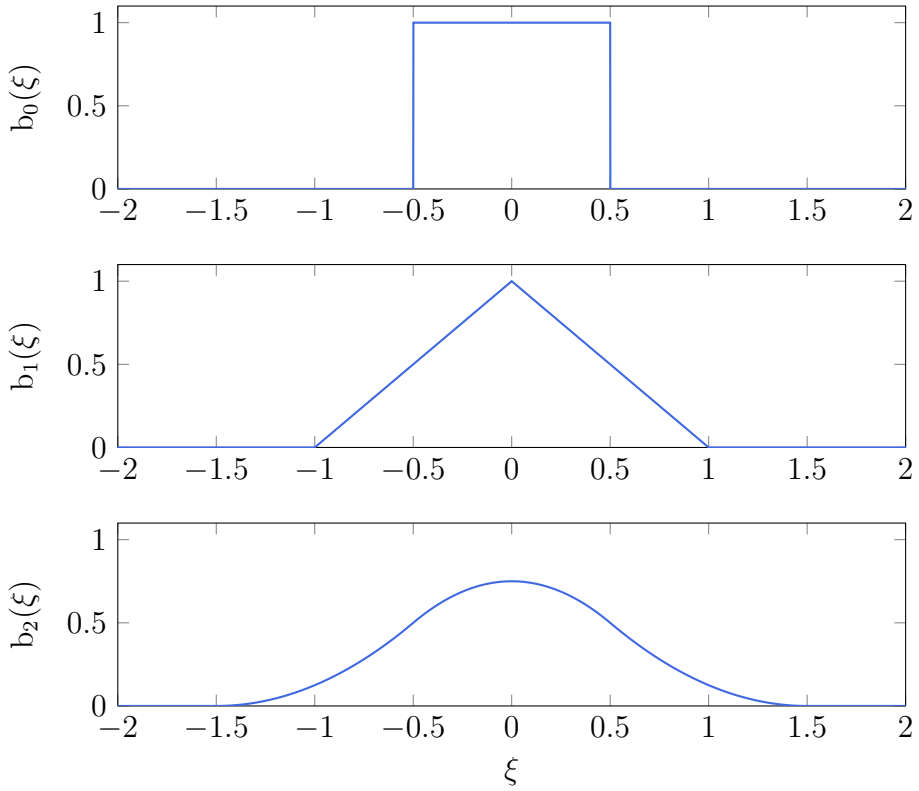

Leapfrog scheme

The two first-order differential equations that we need to be integrated which we have described in section 2.2.2 and written here as

$$m\frac{\mathrm{d}\mathbf{v}}{\mathrm{d}t} = \mathbf{F} \tag{3.2.2}$$

$$\frac{\mathrm{d}\mathbf{r}}{\mathrm{d}t} = \mathbf{v} \tag{3.2.3}$$

where $\mathbf{F}$ is the force which might consist of the electric and magnetic force. Descritising the above equations by using *finite-difference* method for each particle i we yield

$$m_i\frac{\mathbf{v}_i^{n+\frac{3}{2}} - \mathbf{v}_i^{n+\frac{1}{2}}}{\Delta t} = \mathbf{F}_i^{n+1}$$

$$\frac{\mathbf{r}_i^{n+1} - \mathbf{r}_i^{n}}{\Delta t} = \mathbf{v}_i^{n+\frac{3}{2}}$$

as depicted in fig. 3.6 which shows the method's time centring. As mathematically described above, velocities are defined by half-integral time-level while positions

and fields are defined at integral time-level. There are thing to evaluate regarding

Figure 3.6: Illustration of the integration method used in the Leapfrog scheme. Velocity is evaluated at half times while position at integral time steps.

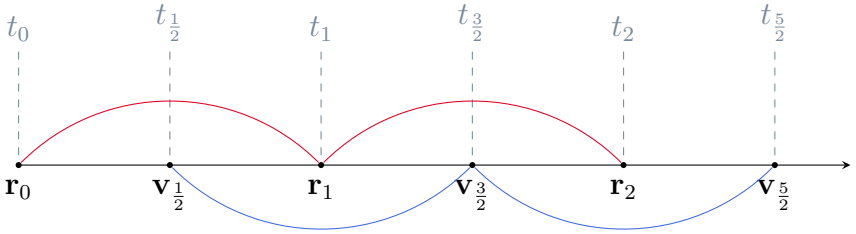

this method. First, the initial condition for the velocity and position at $t = 0$ must be such that it fits the flow as we will push back $\mathbf{v}(0)$ to $\mathbf{v}(-\frac{\Delta t}{2})$ by using the initial $\mathbf{F}$ calculated (Birdsall and Langdon, 2004). Second, the energy calculated from the velocity and field i.e. kinetic and potential energy, must be adjusted at the same time (Birdsall and Langdon, 2004). When it comes to accuracy we have two sources, round-off errors and truncation errors, both of which are local errors. The former arises due to finite word-length of words within a computer and the later is caused by descritisation of continuous variables. The leapfrog method is a second-order accurate approximation to the equations of motion described above. For an elaborate examination of the method in terms of accuracy, stability and the relativistic approach see Hockney and Eastwood, 1988; Grigoryev, Vshivkov, and Fedoruk, 2002; Jardin, 2010.

Boris scheme

In magnetised plasma simulation the Boris method is the dominant method of choice which has been examined thoroughly in Qin et al., 2013 in which they show it conserves the phase-space volume. The equations we start with are the same as the one in Leapfrog namely eqs. (3.2.2) and (3.2.3). Only here we have $\mathbf{F} = q(\mathbf{E} + \mathbf{v} \times \mathbf{B})$ as the Lorentz force. The left-hand side is kept as in the Leapfrog scheme while the magnetic term is centred by averaging $\mathbf{v}_i^{n+\frac{3}{2}}$ and $\mathbf{v}_i^{n+\frac{1}{2}}$ such that eq. (3.2.2) is written as

$$\frac{\mathbf{v}_i^{n+\frac{3}{2}} - \mathbf{v}_i^{n+\frac{1}{2}}}{\Delta t} = \frac{q_i}{m_i}\left[\mathbf{E} + \frac{\mathbf{v}_i^{n+\frac{3}{2}} + \mathbf{v}_i^{n+\frac{1}{2}}}{2} \times \mathbf{B}\right] \tag{3.2.4}$$

One could decompose the above into three scalar equations and solve them simultaneously for each component of the axis or to subtract the drift velocity from $\mathbf{v}$ there are quite a few ways (see Birdsall and Langdon, 2004). The most

Figure 3.7: Diagram from which $\tan(\theta/2)$ is obtained. (Recreated from Birdsall and Langdon, 2004, p.60).

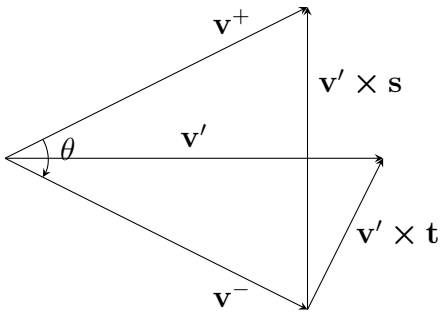

common way is by separation of the electric and magnetic forces by substitution of

$$\mathbf{v}_i^{n+\frac{3}{2}} = \mathbf{v}_i^+ + \frac{q_i \mathbf{E}}{m_i}\frac{\Delta t}{2} \tag{3.2.5a}$$

$$\mathbf{v}_i^{n+\frac{1}{2}} = \mathbf{v}_i^- - \frac{q_i \mathbf{E}}{m_i}\frac{\Delta t}{2} \tag{3.2.5b}$$

into eq. (3.2.4) which will cancel out $\mathbf{E}$ and leave us with

$$\frac{\mathbf{v}_i^+ - \mathbf{v}_i^-}{\Delta t} = \frac{q_i}{2m_i}(\mathbf{v}_i^+ + \mathbf{v}_i^-) \times \mathbf{B} \tag{3.2.6}$$

describing the rotation. For computation we add half the electric impulse to the previous computed velocity by using eq. (3.2.5a) to obtain $\mathbf{v}^-$ then rotate by eq. (3.2.6) to obtain $\mathbf{v}^+$ and finally add the remaining electric impulse eq. (3.2.5b) to obtain the new computed velocity, $\mathbf{v}_i^{n+\frac{3}{2}}$.

Implementation-wise we would like to find a vector $\mathbf{v}'$ bisecting the angle formed between pre- and post-rotation velocity. This angle of rotation θ as shown in fig. 3.7 is given by

$$\tan\left(\frac{\theta}{2}\right) = -\frac{q_i B}{m_i}\frac{\Delta t}{2}$$

or in vector form

$$\mathbf{t} \equiv -\hat{\mathbf{b}}\tan\left(\frac{\theta}{2}\right) = \frac{q_i \mathbf{B}}{m_i}\frac{\Delta t}{2}$$

Now as we have assumed an arbitrary direction of $\mathbf{B}$ and $\mathbf{v}$ we can write the bisector vector which is produced by the incrementation of $\mathbf{v}^-$ (Birdsall and Langdon, 2004) and which is perpendicular to both $(\mathbf{v}^+ - \mathbf{v}^-)$ and $\mathbf{B}$ as

$$\mathbf{v}' = \mathbf{v}^- + \mathbf{v}^- \times \mathbf{t}$$

Furthermore, to satisfy the requirement that the magnitude of velocity remains constant in the rotation we must have a vector $\mathbf{s}$ parallel to $\mathbf{B}$, and $(\mathbf{v}^+ - \mathbf{v}^-)$ is parallel to $\mathbf{v}' \times \mathbf{B}$ such that we yield

$$\mathbf{v}^+ = \mathbf{v}^- + \mathbf{v}' \times \mathbf{s}$$

where

$$\mathbf{s} = \frac{2\mathbf{t}}{1 + t^2}$$

The method is well documented in Qin et al., 2013 and the relativistic approach is covered in Birdsall and Langdon, 2004

3.2.3 Integration of the field equations

In the frame of the electro-static model section 3.1.2 together with the equations eqs. (3.1.5) to (3.1.7). One common way to descritise the equations is by use of finite-difference method which we will do here in two dimensions, however, three dimensional is straightforward (Birdsall and Langdon, 2004). By using the five-point stencil on the grid as shown in fig. 3.8 then eq. (3.1.5) becomes

$$\frac{\phi_{j-1,k} - 2\phi_{j,k} + \phi_{j+1,k}}{\Delta x^2} + \frac{\phi_{j,k-1} - 2\phi_{j,k} + \phi_{j,k+1}}{\Delta y^2} = -\frac{\rho_{j,k}}{\varepsilon} \tag{3.2.7}$$

There are many methods one can use to solve the above equation, many of which are discussed in Hockney and Eastwood, 1988, chap.6. The equation can be solved for all types of boundary conditions including one in which we have a biased-potential on the spacecraft.

Figure 3.8: 5-point stencil illustrated in 2D.

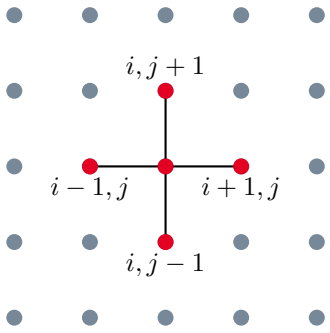

In the case of eq. (3.1.6) we can descritise it by using the two-point stencil for each direction as

$$(E_x)_{j,k} = \frac{\phi_{j-1,k} - \phi_{j+1,k}}{2\Delta x} \tag{3.2.8a}$$

$$(E_y)_{j,k} = \frac{\phi_{j,k-1} - \phi_{j,k+1}}{2\Delta y} \tag{3.2.8b}$$

The fields and potentials are located at the same points. As fig. 3.2 shows we will weight the fields back to the particles by using a weighting scheme.

3.2.4 Weighting

From fig. 3.2 we see that there are two parts we are still missing in our calculation, namely the charge density on the discrete grid points and the force at the particles on the grid points. The former is obtained by using the particle positions and the latter is yielded by the calculated fields (Birdsall and Langdon, 2004). The scheme for the weighting is usually chosen to be the same for both the density and force calculations to avoid the occurrence of a self-force, see Birdsall and Langdon, 2004, chap.10-11.

We have already visited the particle shapes in section 3.2.1 and mentioned the CIC scheme. The CIC is also the one used in our code for the charge assignment and we will here elaborate on it. For the zero-order weighting what we essentially do is count the number of particles within a grid distance about the jth grid point which is $\pm\Delta x/2$ in the x direction and assign that number to that grid, hence the name, *nearest-grid-point* (NGP). This is illustrated in fig. 3.5 as the first plot. Computationally, this scheme is fast since in one-dimension only one grid is looked up to assign the particle to (Birdsall and Langdon, 2004), but it is also very noisy because of the jumps given rise to by particles passing through a grid boundary.

For most purposes a first-order, CIC, weighting is adequate. By using CIC we reduce the noise level, but increase the computation time as a result of looking up two grid points for each particle (in one-dimension). In 2D, for a spatial grid which has grid points (X_j, Y_k) with grid spacing Δx in the x direction and similarly in the y direction, we can weight the charges at the point (x, y) by

$$\begin{aligned}
\rho_{j,k} &= \rho_c \frac{(X_{j+1} - x)(Y_{k+1} - y)}{\Delta x \Delta y} \\
\rho_{j+1,k} &= \rho_c \frac{(x - X_j)(Y_{k+1} - y)}{\Delta x \Delta y} \\
\rho_{j,k+1} &= \rho_c \frac{(X_{j+1} - x)(y - Y_k)}{\Delta x \Delta y} \\
\rho_{j+1,k+1} &= \rho_c \frac{(x - X_j)(y - Y_k)}{\Delta x \Delta y}
\end{aligned}$$

where $\rho_c = q_i/(\Delta x \Delta y)$ is the charge density uniformly filling a grid (Birdsall and Langdon, 2004).

Computationally before the weights are calculated and the charges assigned, the nearest left-hand grid point j is located first, therefore, $x_i > X_j$ always. We have illustrated the above method together with NGP in fig. 3.9. In summary

Figure 3.9: Charge assignment for linear weighting in 2D. The coloured areas assigned to their dedicated nodes, i.e. a to A, b to B etc. with the red dot indicating the particle (Inspired by Birdsall and Langdon, 2004, p.309).

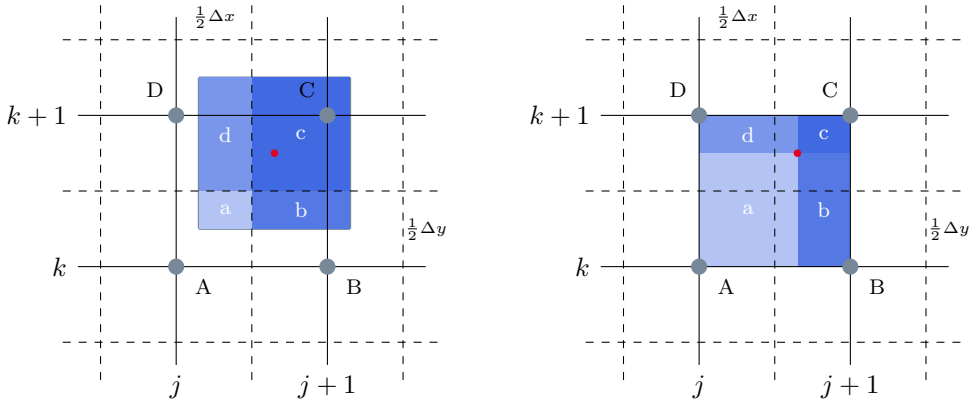

(a) CIC **(b)** PIC

we can find the grid charge density ρ_j with a shape function $S(X_j - x_i)$ by using the charges q_i at x_i from

$$\rho_j \equiv \rho(X_j) = \sum_i q_i S(X_j - x_i)$$

where the shape function S can be any other than the CIC we have above or NGP. Having found the charge density we can then use it to find the force on the particle by interpolation from the grid electric field as

$$F_i = q_i \Delta x \sum_j E_j S(X_j - x_i)$$

in which we will use the same shape function as above. There is nothing holding us back from using different shape functions, however, it can lead to a gravitation-like instability and gives rise to a self-force as mentioned before (Birdsall and Langdon, 2004).

3.2.5 Charging model

The charging model to calculate the spacecraft floating potential is incorporated in our simulation by using the classical capacitive matrix method (Hockney and Eastwood, 1988). Simply, the surface charging is calculated directly from the deposited charges on the surface. The technique involves the pre-calculation of a capacity matrix $\mathbf{C}$ that will relate the potential and charge on a number of points in the interior.

Capacitance matrix

We start by noting the electric potential ϕ and the charge density ρ can be related by a matrix $\mathbf{A}$ as

$$\rho_i = \sum_{j=1}^{N_g} \mathbf{A}_{ij}\phi_j, \qquad i = 1, \ldots, N_g$$

where i and j are the indices of the grid points and N_g is the total number of grid points (Hockney and Eastwood, 1988). In the same manner, inversly, we can calculate ϕ as

$$\phi_i = \sum_{j=1}^{N_g} \mathbf{B}_{ij}\rho_j, \qquad i = 1, \ldots, N_g$$

such that $\mathbf{B} = \mathbf{A}^{-1}$.

During the redistribution, there are no changes in the charges inside and outside of the body, only ρ_s which is assigned on the body surface is changed (Yohei Miyake and Usui, 2009). As a result the correction relation of the electric potential, $\delta\phi_s$, to the charge density, $\delta\rho_s$, is given by

$$\delta\phi_{s,i} = \sum_{j=1}^{N_s} \mathbf{B}_{ij}\delta\rho_{s,j}, \qquad i = 1, \ldots, N_s$$

where N_s is the number of grid points on the surface and as such $N_s < N_g$. Further we note that the equipotential is applied on the conductive surface, thus even though ϕ is also subject to change outside the body, we constrain ourselves by the condition of the equipotential and focus only on the potential values on the surface grid points i.e., $i = 1, \ldots, N_s$.

Next we introduce the matrix $\mathbf{B}'$ as the upper-left block of the matrix $\mathbf{B}$. Then the specialised capacitance matrix $\mathbf{C}$ for the grids on the surface can be obtained by $\mathbf{C} = \mathbf{B}'^{-1}$. Finally the relation between $\delta\phi_s$ and $\delta\rho_s$ is given by

$$\delta\rho_{s,i} = \sum_{j=1}^{N_s} \mathbf{C}_{ij}\delta\phi_{s,j}, \qquad i = 1, \ldots, N_s.$$

A direct way to arrive at the capacitance matrix is to place a unit charge on each grid point on the conductive surface with zero charge on the other grid points and solve for the potential. The potential values on the grid points form the elements of one column of the inverse capacity matrix $\mathbf{B}'$ and we repeat the process until all elements are found and lastly the capacitance matrix is found by $\mathbf{C} = \mathbf{B}'^{-1}$ (Hockney and Eastwood, 1988; Yohei Miyake and Usui, 2009).

Chapter 4

Numerical experiments

In the following chapter we will take into account the previous chapters and more specifically target the problem at hand, namely satellite and rocket simulations by using the DiP3D code. We will here introduce the object implementation, experiment set-up, results, and discuss both cases and finally, future work that needs to be done and improvements.

4.1 Experiment set-up

For the simulations that we will be doing we will be using the code DiP3D (Miloch, 2006) which is a PIC program written in C designed to simulate dust and electric probes immersed in plasma. The program reads an `input.txt` file that states the parameters for the simulation to be run and produces `.dat` files containing information for several plasma properties; potential and kinetic energy of the species, density of the species and electric fields for all axes (Miloch, 2006).

We will be using the code and implement an object marking algorithm for easier object implementation to make geometries of the shape of a rocket, represented by a rigid cylinder, and of a satellite, represented by a box, easier. At the end we present the parameters for each of the experimental case.

4.1.1 Object implementation

DiP3D already contains several geometrical shapes hard-coded and ready to be used in the simulations, we would however like to be able to make use of any rigid shape that does not alter in the z-direction. For this we have used the so-called *polygon-fill* algorithm to mark an arbitrary object.

A simple case, a box, contains eight corners, to implement the object we would write the eight coordinates of the eight corners into a `.txt` file which would be read by the file `grid.c` in the program. The coordinates are then stored in an array and the essential idea is to mark the object on the grid by using the corner

Figure 4.1: The marking of an object of length 5x5 on a 16x16 grid.

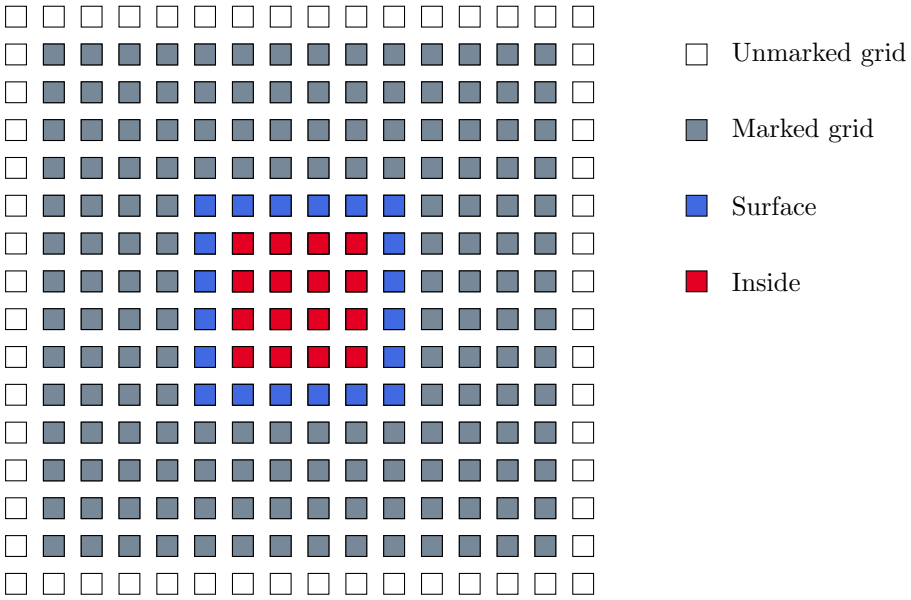

coordinates. The geometry of the object is on the grid points such that the way we mark the object is shown in fig. 4.1

We check if the coordinates of the corner of the object is on the grid by scanning the grid in all three directions and matching the grid coordinates with the object coordinates. If that is the case and the corner coordinates are on the grid then compare the next corner coordinate of the object with the previous and mark with a specific colour or in the numerical case with a number, thus we have outlined the edges and corners of the object. Next we would like to mark the surface and the inside of the object, this is the part that is performed by the polygon-fill algorithm.

Polygon-fill algorithm

First we introduce the pseudo-code of the polygon-fill. The concept depends on the point-in-polygon algorithm (Foley et al., 1995) which is used in order to determine whether a point resides inside a polygon or not. The polygon-fill is done in three parts:

1. Render a row of pixel or in our case, scan one row of the grid which have the same y-coordinate.

2. Loop through the polygon in a clockwise or anti-clockwise direction to find the threshold-crossing nodes i.e. the grid nodes that coincide with the polygon coordinates and store them in an array.

3. Sort the array in increasing x-coordinates.

Figure 4.2: Polygon-fill steps, from ray tracing to filling.

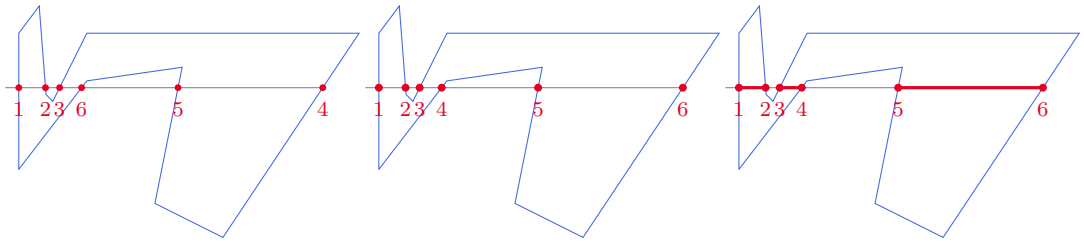

(a) Ray tracing **(b)** Sorting **(c)** Filling

4. Fill between the intersecting grid points of the sorted array.

The process is illustrated in fig. 4.2.

We will here also introduce a pseudo-code, algorithm 1, for the polygon-fill, the code itself written in C is given in Appendix C.1. As written in the pseudo-code, we depend on the x, y and z coordinates provided to us by the `.txt` file in form of an array. The coordinates for the object can be generated in a number of ways depending on the geometry of our object. In our case we generate the cylinder coordinates by using the midpoint-circle algorithm and adding to it the height of the cylinder.

4.1.2 Simulation parameters

For the simulation we make use of the parameters given in table 4.1. We had an electron charge to mass ratio of $-1.758\,500 \times 10^{11}$ C/kg and an ion charge to mass ratio of $3.520\,000 \times 10^{8}$ C/kg. The electron mass was set to $9.111\,112 \times 10^{-31}$ kg and the ion mass was set to $4.551\,673 \times 10^{-28}$ kg. This gives us a mass ratio of $m_i/m_e \approx 500$. For testing purposes we started with a grid size of 64 then for the full simulation went to a 128 grid size. The corresponding system dimension is denoted by L in all directions. Having input the system dimension and grid size we can calculate the grid spacing to be $L/\text{grd size} \approx 0.002\,344$ m. Most of the parameters were taken from the various sources as given in section 2.1 such as Bedingfield, Richard D. Leach, and Margaret B. Alexander, 1996. At 128 we

Table 4.1: Simulation parameters.

	Grid size	L m	Δt s	$t_{\max}$ s	n m^{-3}	N_p	λ_D m	Cs Mach	T_e/T_i
Cylinder	128	0.3	2.38E-9	6.38E-5	2E11	2E6	7.43E-03	1.9	10
Box	128	0.3	6.28E-10	6.28E-5	2E11	9E6	7.43E-03	1.9	10

Algorithm 1 Polygon-fill with bubble sort

```
1: function scanRow(corners, ngx, ngy, voxel,newN)
2:     for J ← 0, ngy do                          ▷ Build a list of nodes in nodeX
3:         for i ← 0, corners do
4:             if y_i < J  and  y_j ≥ J  or  y_j < J  and  y_i ≤ J  then
5:                 nodeX ← (x_i + (J − y_i)/(y_j − y_i)(x_j − x_i))
6:             end if
7:         end for
8:         i ← 0
9:         while i < nodes − 1 do                 ▷ Sort using Bubble sort
10:            if nodeX_i > nodeX_{i+1} then
11:                swap ← nodeX_i
12:                nodeX_i ← nodeX_{i+1}
13:                nodeX_{i+1} ← swap
14:            else
15:                i ← i + 1
16:            end if
17:        end while
18:        for i ← 0, nodes do                    ▷ Fill between the nodes
19:            if nodeX_i ≥ ngx then break
20:            end if
21:            if nodeX_{i+1} > 0 then
22:                if nodeX_i < 0 then
23:                    nodeX_i ← 0
24:                end if
25:                if nodeX_{i+1} > ngx then
26:                    nodeX_{i+1} ← ngx
27:                end if
28:                for I ← nodeX_i, nodeX_{i+1} do
29:                    voxel(I, J) ← newN         ▷ fil in with the desired value
30:                end for
31:            end if
32:        end for
33:    end for
34: end function
```

had around 2 partiles per cell in the case of the cylinder and 4 particles per cell in the case of the box. The velocity is found from section 2.3.1 from which then we use the sound speed in plasma

$$C_s = \sqrt{\frac{(T_e + \frac{5}{3}T_i)}{m_i}} \tag{4.1.1}$$

which gives us then the velocity in Mach number

$$M = \frac{v}{C_s}$$

where v is the spacecraft velocity. At an altitude of 400 km above Earth we have a velocity of $7668\,\mathrm{m\,s^{-1}}$. The parameters are then inserted into the `input.txt` file and read by the program.

4.2 Results

We here present the results of the two cases mentioned above. Both simulations were run on a supercomputer on two nodes. We will look at the potential, particle density and other possible properties of the interaction between the plasma and the objects. The results below were retrieved by using ParaView, an open-source program for interactive, scientific visualisation. This was done by converting the `.dat` files to `.raw` files which could be read by the program to plot the data. In the figures we will see a clear Mach cone trailing the object as a result of the supersonic speed. The angle between the edge of the Mach cone and the line through the centre of the spacecraft is called the Mach angle.

All the figures in the following subsections are conceived from ParaView and are thus subject to some restrictions. Notably, the ranges of the axis are given in grid length, which corresponds to 128 grid points in all domain directions unless otherwise stated, see table 4.1 for the parameters. Furthermore, the figures presented here are taken from the last time step, we will specify it more clearly if necessary or it deviates from it.

The plasma frequency, eq. (2.2.6), can be fetched from the calculated data set and has the value $\omega_{pe} = 2.522\,745 \times 10^7\,\mathrm{s^{-1}}$ for the electron and, $\omega_{pi} = 1.128\,687 \times 10^6\,\mathrm{s^{-1}}$ for the ion. Subsequently we can use the values to find the plasma period for the two species by using $\tau = 2\pi/\omega$, yielding us $\tau_{pe} = 2.49 \times 10^{-7}\,\mathrm{s}$ and $\tau_{pi} = 5.57 \times 10^{-6}\,\mathrm{s}$, corresponding to the electron and ion plasma period respectively. Additionally, the simulation time was around 30000 iterations for the cylinder and around 100000 iterations for the cube. We start averaging and save data after every 500 time step, this gives us $3.1 \times 10^{-7}\,\mathrm{s}$ and $1.15 \times 10^{-6}\,\mathrm{s}$ for the box and cylinder respectively.

4.2.1 Cylinder

In fig. 4.3a we present the potential across the cylinder with $r = 16$ positioned near the centre in the grid at grid point 60. The figure shows the average potential at the last time step corresponding to $t = 6.307 \times 10^{-5}\,\mathrm{s}$. We have sliced it in the middle across the x-axis. The direction of the flow is in the positive z-direction with the plasma potential set to 0V, however, as the colour bar shows in fig. 4.3a

there are some fluctuations above zero potential as a result of the numerical noise given rise to by the number of finite sized particles per cell. The flow around the

Figure 4.3: Cross-section of potential along z-axis and the corresponding potential profile around two opposite sides of the cylinder.

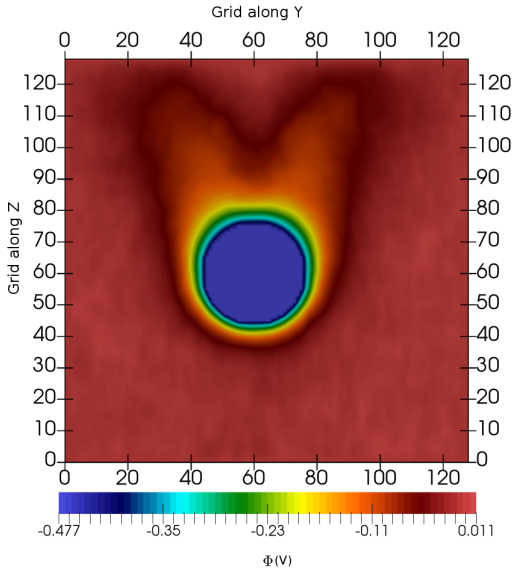

(a) Potential cut along z-axis in the direction of flow.

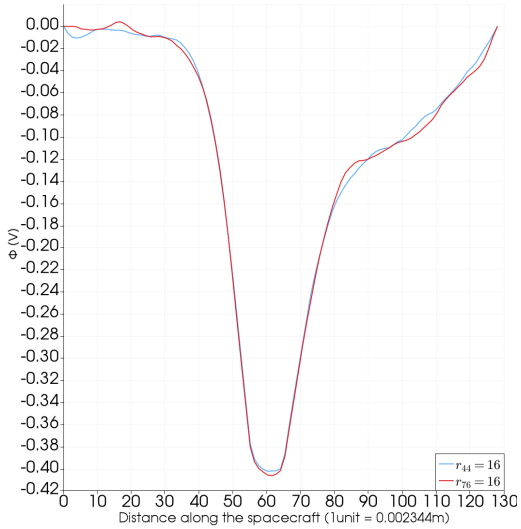

(b) Asymmetry in the flow.

object is also asymmetric and can be seen more clearly in fig. 4.3b in which we have the potential in the y-axis and x-axis is the direction of flow i.e. along the positive z-direction. We have here plotted the potential along the two opposite sides of the cylinder in which the red line in the figure shows the potential across the right side of the object in fig. 4.3a at grid point 76 and the blue line shows the potential on the left side of the cylinder at grid point 44. The details of fig. 4.3b show that there are some fluctuations behind the object as well in front. There is also a significant drop in potential signifying the negatively charged surface of the cylinder.

The potential dip shown in fig. 4.3b is on the surface, however, if we now take a potential cut across the centre of the cylinder at $r = 0$ corresponding to grid point 60 in which we have the largest cross-sectional area in the direction of the flow we get the plot as in fig. 4.4a Where the axis are the same as in fig. 4.3b with x-axis in the figure being in the direction of the flow corresponding to the z-axis in the simulation. The minimum negative potential in the figure has the value $\Phi = -0.476\,803\,\mathrm{V}$ and the maximum value $\Phi = 0.010\,637\,1\,\mathrm{V}$. The maximum value corresponding to the plasma potential, which ideally should be zero (Shul and Pearton, 2000). We previously outlined that we have taken the last time step for plotting, assuming that the system has reached steady state and that

Figure 4.4: Potential across the middle of the rocket along the flow and the negative potential profile over time.

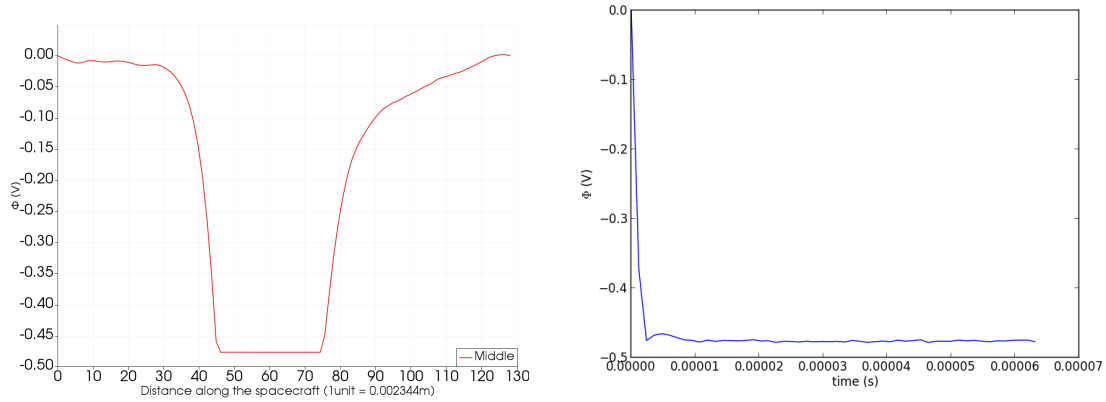

(a) Potential across the centre of the spacecraft, notice the drop, reaching the floating potential.

(b) Potential over time plot showing the potential reaching steady state.

the potential variations are minimum. This is indeed the case as seen in fig. 4.4b which shows the minimum potential over time reaching the steady state and affirming that our last time step is indeed in the steady state phase.

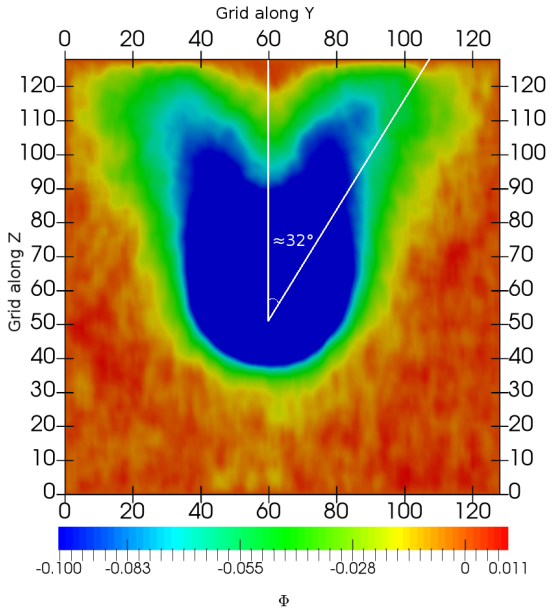

Figure 4.5: The Mach angle approximated, by shifting the potential for easier visualisation of the Mach cone edges.

The wake structure behind the object is also clearly visible in fig. 4.3a forming

Figure 4.6: Density of ions and electrons around cylinder

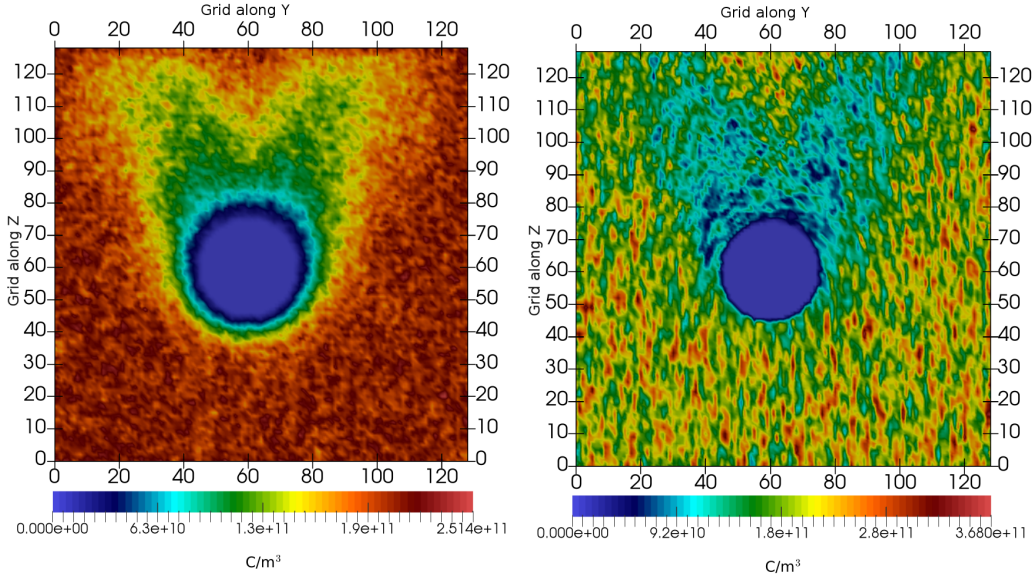

(a) Electron density **(b)** Ion density

a significant potential fluctuation behind the rocket. As a result of the velocity difference between ions and electrons we therefore see some positive potential behind the spacecraft. Since we are dealing with supersonic velocities we expect to be able to determine a Mach angle from the figures given and indeed by shifting the potential in fig. 4.3a to make the Mach cone more clear and using the outer edge we can approximate the Mach angle. The angle is found by using the measurement tool in GIMP (GNU Image Manipulation Program) and is presented in fig. 4.5. The figure dimensions are the same as in fig. 4.3a with corresponding axes labelling. The difference being the shifted potential for clearer indication given by the colourbar making the wake formation more clear.

The density for the charged particles is shown in fig. 4.6 where we have the density for the electron in fig. 4.6a and for the ion in fig. 4.6b, both in the same domain and axis length. Particularly of interest is the fluctuations of the ion density behind the object and as mentioned before, we see there is a number of ions accumulated behind the object as a result of the velocity difference. In fig. 4.7 we have plotted the cross-section view of the density across the middle of the cylinder and once again we see the ion density profile having high fluctuations.

We also observe an induced electric dipole moment if we look at the total density $\Delta n = n_i - n_e$ data which has been made to look more clear in fig. 4.8a. Where we have adjusted the density range to go from minimum to zero for a more visual clarity. The impact surface of the object shows a larger negative density than than the back of the object as a consequence of the flow hitting the object in the front and thus accumulating negative charge on the surface.

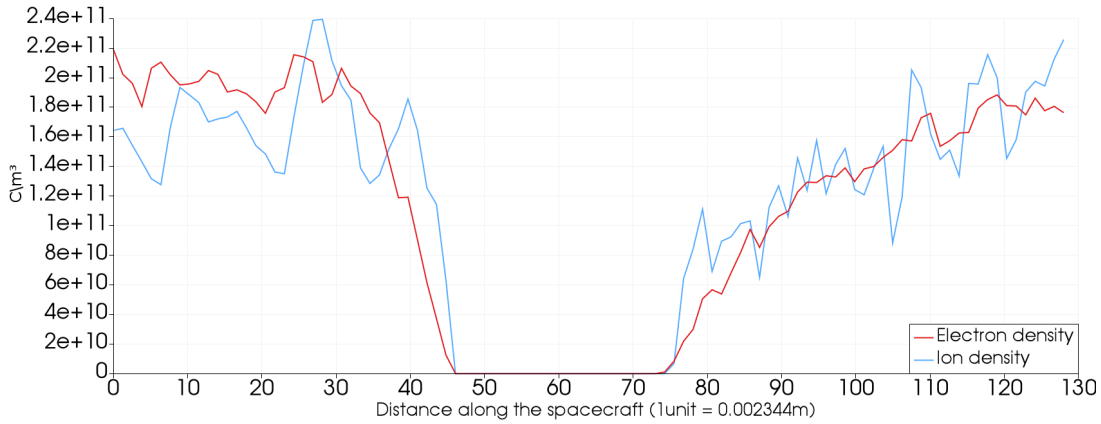

Figure 4.7: Ion and electron density profile.

This had previously been observed in 2D (Miloch, 2006). The negative charge is also visible around the object, as a result of the shape of the object and the trajectory of the electrons, but to a lesser degree. This total density data that showed accumulation of negative charged particles in the front of the object can

Figure 4.8: Total density and the electric field along the direction of flow, i.e. z-axis

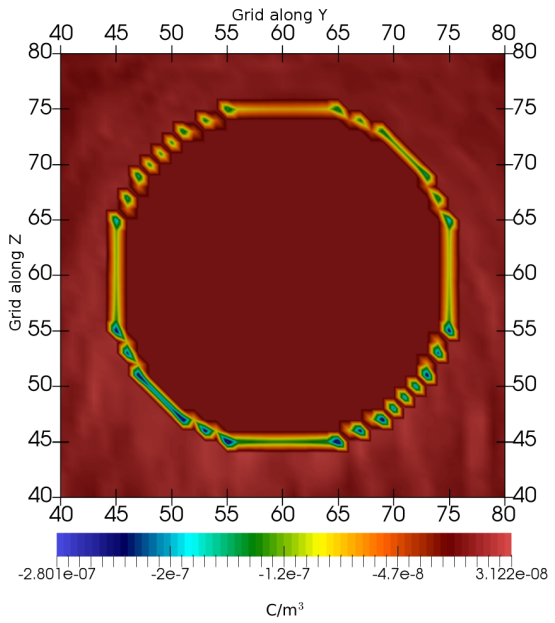

(a) Section view of the surface charge density showing the induced electric dipole moment (density range has been modified to show the negative density).

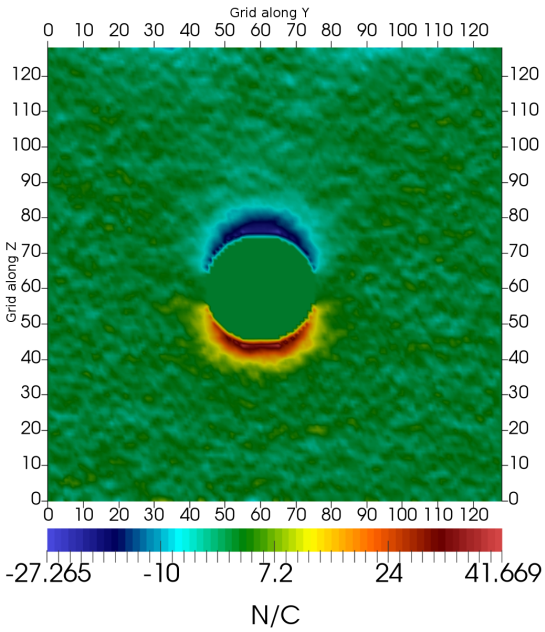

(b) Electric field cross section along the middle of the cylinder in the direction of the flow.

be further elaborated by the electric field data given here along the z-axis, in the direction of flow with similar dimensions and labels as fig. 4.3a. The plot in fig. 4.8b shows the electric field data along the z-direction and we see here a very strong electric field in the upstream as compared to the downstream. The electric field is essentially a reflection of the potential surrounding the spacecraft given by $\boldsymbol{\nabla}\Phi = -\mathbf{E}$, albeit along the direction of flow as in fig. 4.8b.

4.2.2 Box

Since we are dealing with similar parameters in both simulations we expect to see similar results, particularly when it comes to the minimum value of the potential and Mach angle. The box has different dimensions than the cylinder, it is smaller in dimensions and almost near the thick sheath limit. As it should be, we see similar results starting with the potential data as shown in fig. 4.9a with a similar potential range as in the previous case. In this case however, the wake is much sharper forming around the object as a result of the size of the object and the rigidity of its clear edges and corners. The corresponding asymmetry can be seen in fig. 4.9b similar with the previous case the asymmetry is taken at the two opposite edges of the box, the left edge at grid point 59 and the right edge at 70, thus showing off the potential variation in the direction of the flow on the surface of those two edges. Furthermore the minimum potential in this case has the value

Figure 4.9: Potential distribution and potential profile around the edges.

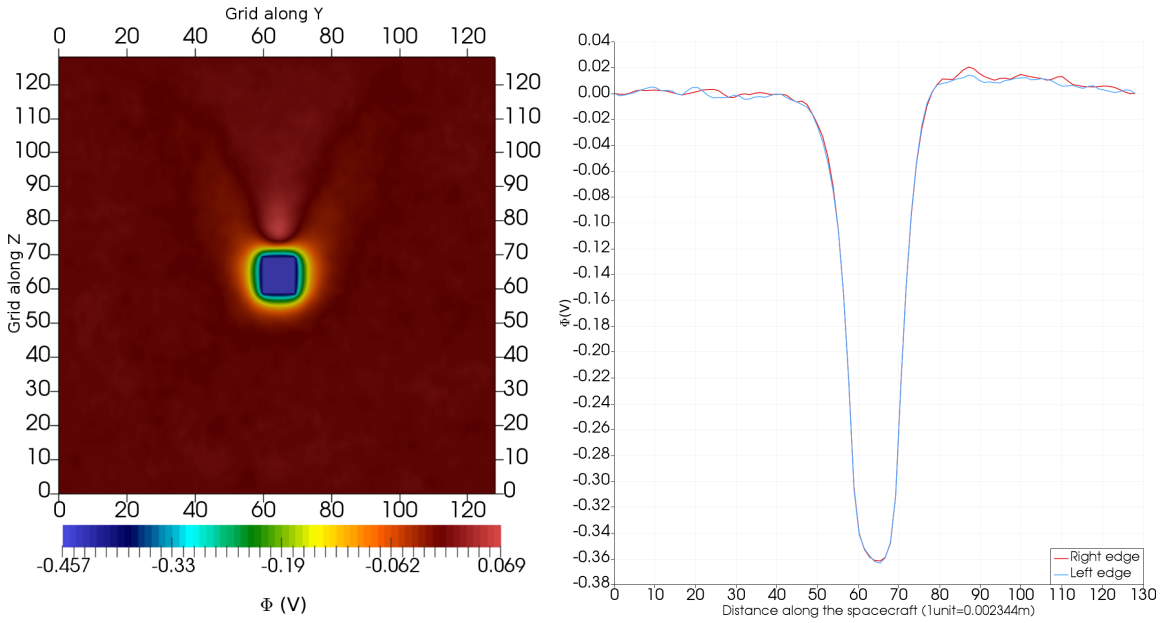

(a) Potential distribution around the box.

(b) Asymmetry along the box edges in the direction of flow.

Figure 4.10: Potential cut along the direction of the flow through the centre of the object and the negative potential profile over time.

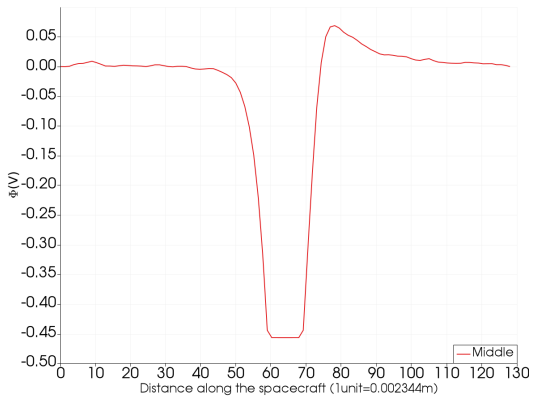

(a) Potential cut through the middle of the box.

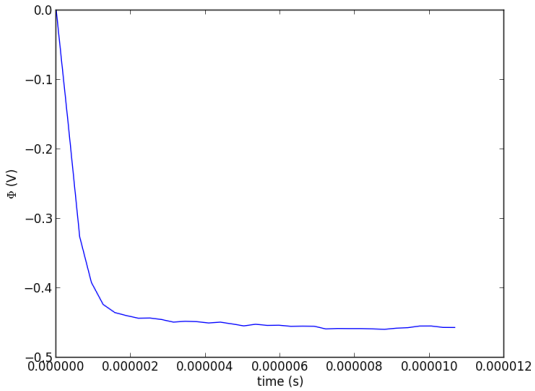

(b) Potential over time plot showing the potential reaching steady state.

$\Phi = -0.456\,539\,\mathrm{V}$ which is very close to that of the cylinder, however given the dimensions of the box it deviates slightly. In comparison to the cylinder there is a significant rise in the potential behind the object and this can be seen in fig. 4.10a together with the dip in potential. The minimum potential that is reached has been averaged over previous time-steps as we previously have mentioned and as such the potential plots that are given here, just as in the case of the cylinder, are the averaged potential. We have in fig. 4.10b plotted the minimum potential over the simulation period and we can see that at the last time step we have already attained steady state.

As previously mentioned, since both simulations are run with $M = 1.9$ we expect to see a similar Mach angle as in the cylinder case and indeed that is the case as shown in fig. 4.11 The potential in the figure has been shifted to the same range as in fig. 4.5 and it shows a sharp cone edge compared to the cylinder case which made it easier to approximate the Mach angle by using GIMP. The density variations can be seen in fig. 4.12 where we have the density variation data for the last time step at $t = 1.0362 \times 10^{-5}\,\mathrm{s}$ for both the electrons and ions. As it was with the previous case, we see a vivid accumulation of positive charges behind the object and lots of fluctuations around it in fig. 4.12b. In fig. 4.13 we have plotted the ion and electron density profile across the middle of the box in the direction of the flow. We see a peak in the ion density profile arising right behind the object, the ion focus point. When plotting the density data and adjusting the range we get fig. 4.14a which shows us the total density $\Delta n = n_i - n_e$ where we have adjusted the range of the charge per meter cubed for more clarity. The figure has been sliced in the middle and a few grid points to each side to bring the object in focus. We see a peak in the negative potential on the corners of

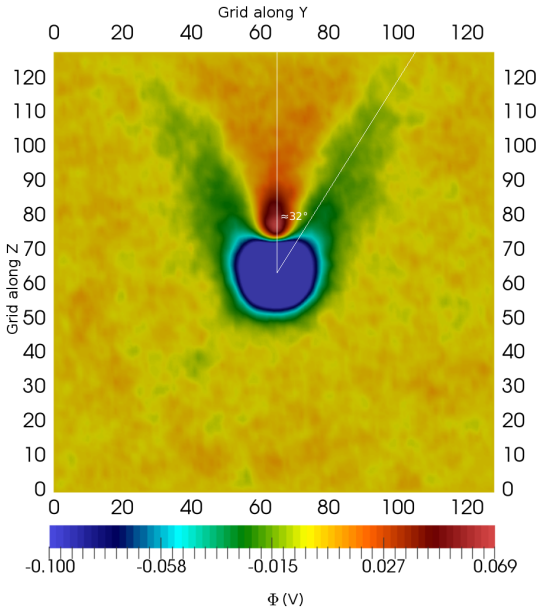

Figure 4.11: The Mach angle approximated, by shifting the potential for easier visualisation of the Mach cone edges.

(a) Electron density variation. **(b)** Ion density variation

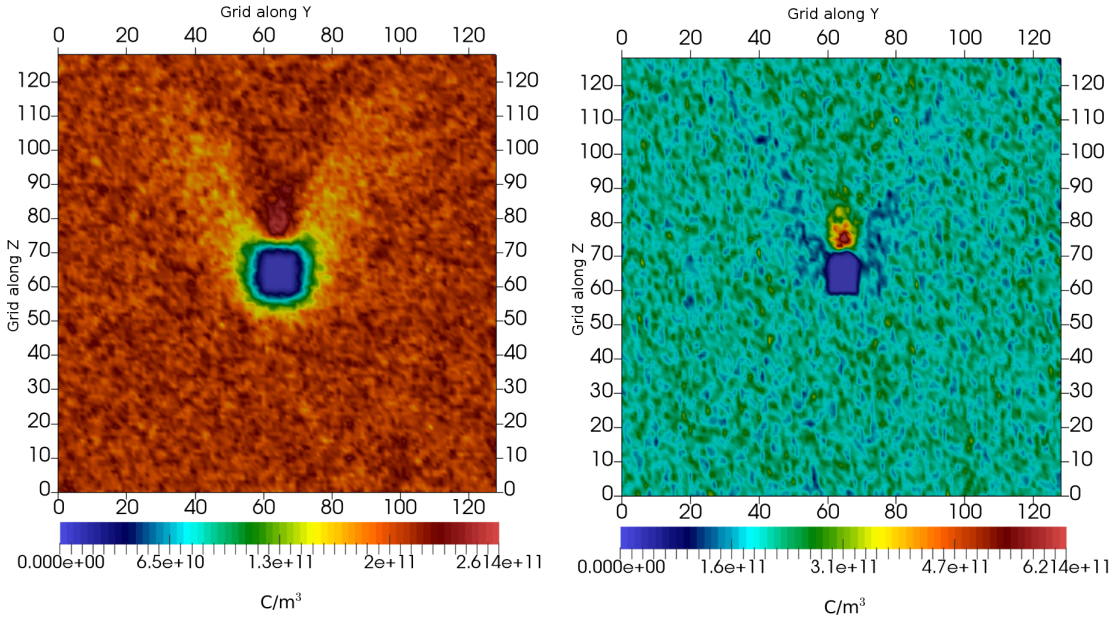

Figure 4.12: Density variations for both electrons and ions.

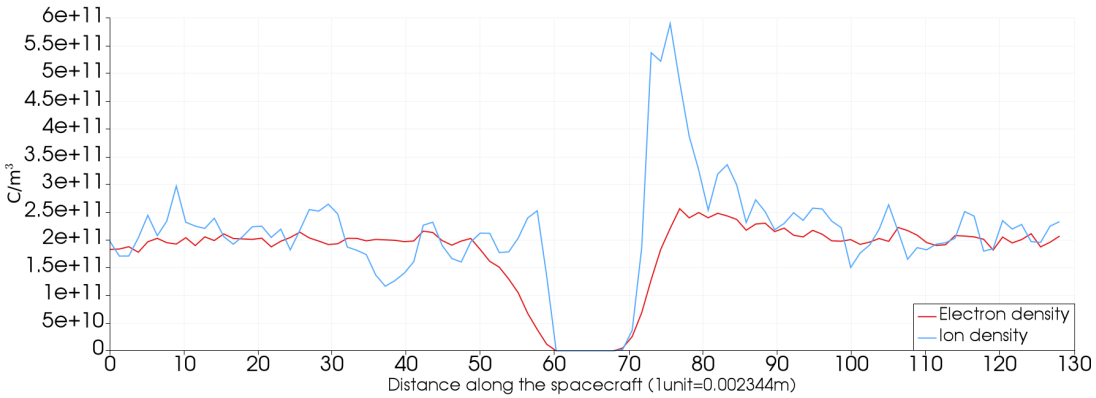

Figure 4.13: Ion and electron density profile along the flow through the middle of the object.

the box arising due to the flow and the shape of the object. Compared to the more refined object in section 4.2.1 where we saw a rise in the negative potential in the upstream part, we here see it in all corners.

Figure 4.14: Total density and electric field in the y-z plane.

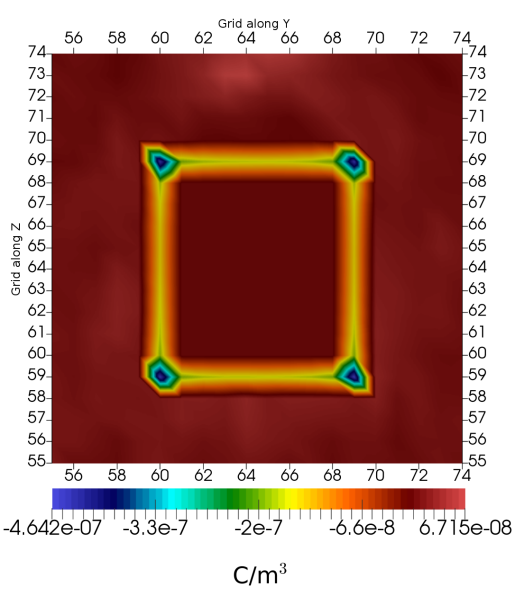

(a) Total density profile for the object indicating negative potential on the corners.

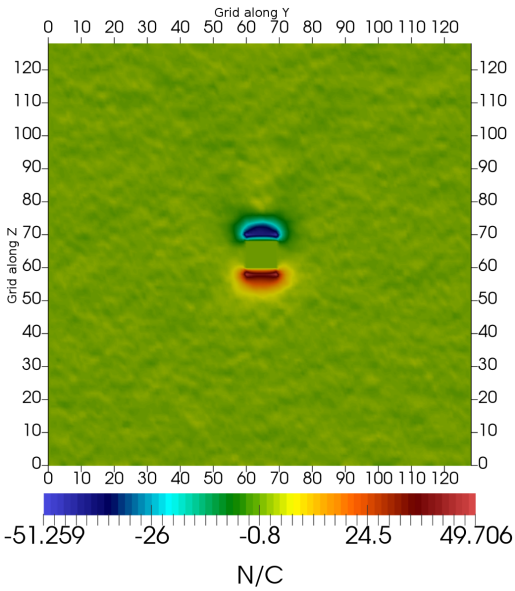

(b) Electric field along the direction of flow.

The potential gradient reflects itself in the electric field, fig. 4.14b, just as in the cylinder case. The anisotropic property of the electric field is less apparent here than in the previous case, particularly when it comes to the magnitude where

we do not see a peculiar shift in in the electric field, i.e. the difference between the negative and positive poles are less than in the case of the cylinder.

4.3 Discussion

We have presented the results in section 4.2 and we will here elaborate and discuss the results obtained. We will look into previous work done that correspond with the current results obtained and look into similarities and differences between the two cases and the previous studies done.

4.3.1 Previous work and comparison

The first results we presented in section 4.2 showed figs. 4.3a and 4.9a for the two cases we had simulated. In both cases we observed the wake structure, floating potential, electric field in upstream and downstream, and asymmetry, the latter being a result of the fluctuations raised by numerical errors.

Observations and connection with theory

In the case of the cylinder we had anisotropic potential where the potential had different values around the object, particularly inside the wake. The same had been observed in the case of the box. In both cases this anisotropic potential was reflected again in the density of the two objects. For the cylinder we could observe the depletion of electron and ions in figs. 4.6a and 4.6b. Looking at the density for the electron we see a decrease in electron density inside the wake as well as in the upstream, which forms the sheath. On the opposite charge, the ions in fig. 4.6b, we see an almost zero density inside the wake as well as around the object in the upstream as well as downstream. The reason for this occurrence lies in the mobility of the electrons as compared to the ions. The electrons have much larger velocity and thus able to penetrate the wake formation while the ions are heavier and this leads to a depletion in the region of the wake. We essentially have a sink of particles as the particles are absorbed by the object and this effect can be observed in both cases as evident in figs. 4.6a, 4.6b, 4.12a and 4.12b for the cylinder and box respectively. As the density of the electrons build up inside the wake while there are still ions outside of the wake, an induced electric field is initiated. This is the ambipolar electric field and it causes the forthcoming electrons to slow down and in which case only high velocity electrons can penetrate the wake. This is on par with the theory we revised in section 2.3.2 and the corresponding illustration of the process in fig. 2.7 which showed the charge accumulation on a wall.

However, in the case of the box, we have a region of ion focusing right behind the object. This can be explored in more detail by referring to the potential

profile, and the density profile for the ions cut through the middle of the box in figs. 4.10a and 4.12b. In figs. 4.10a and 4.12b, there is a sharp rise in the ion density and potential respectively, occurring at around grid point 70 along the z-axis, which is right behind the object. This effect could not be observed in detail while looking at the density profile of the cylinder in fig. 4.7. This is likely due to the difference in the geometry of the objects. The box is a cube of equal length in all directions, while the dimensions of the cylinder are different and the geometry is smoother in terms of grid resolution. Another factor that could have affected the rise of an electron wake behind the rocket covering the ion focusing region could be the flow velocity relative to the object size. At higher velocities we would perhaps expect to see a much stronger wake around the rocket, however, that would be unrealistic as velocities above the one used in the simulations would put us below LEO as can be calculated from the equations in section 2.3.1.

Despite the differences in the wake structure, we discover some fluctuations in the density profile for the cylinder as well and it varies greatly towards the end of the grid, while in the box case, it seems to stabilise and follow the density profile of the electron in terms of amplitude. The fluctuations could be a result of the numerical inaccuracy in terms of number of particles per cell since as we have mentioned in table 4.1 we run the simulations with only a few million of particles. Another important thing to notice here is as we mentioned in section 4.2 we write the data after every 500 iterations, this has implications on the fluctuations for it is related to the plasma period of the ions and electrons which we wrote in the previous section. Now, the data is being saved every 500 iterations which corresponds to 3.1×10^{-7} s and 1.15×10^{-6} s for the box and cylinder respectively. Since we have a plasma period of $\tau_{pi} = 5.57 \times 10^{-6}$ s for the ion and $\tau_{pe} = 2.49 \times 10^{-7}$ s for the electron we notice that in both cases we do not save the data before a full ion plasma period has been reached. This could be one of the reasons why we see a significant fluctuations in the ion density profiles in both simulations as compared to the electron where the amplitude is more or less steady as given by the numbers above it reaches a full electron plasma period before the data is saved. Had we run the simulations with drastically more particles, we would expect to see predictable fluctuations in the data. However, the results would not differ too far away from our current data set, as in the present simulations, we are solving the field equations by using the five-point stencil as described in section 3.2.3 and the values are thus averaged. Using more particles would also drive the simulation towards the fluid description.

A distinct observation we have omitted so far from the discussion is the potential dip across the spacecraft which can be seen in the cut potential profile across the middle of the objects in the direction of the flow in figs. 4.4a and 4.10a for the rocket and satellite respectively. We had previously revised this potential dip in section 2.3.4 as floating-potential and we briefly touched upon it in sec-

tion 4.2. In the case of the cylinder in the previous section we yielded the value $\Phi = -0.476\,803\,\mathrm{V}$ as the minimum for the potential, and this value correspond to the floating-potential. We can now verify this by using the theory and the floating-potential equation discussed in section 2.3.4. Since we are dealing with the cylinder, we can approximate the floating potential analytically by noting that the rocket is in the thin sheath regime and thus its dimensions is much larger than the Debye length. This allows us to use the planar sheath theory from section 2.3.4 and the modified floating potential equation that accounts for the potential drop in the pre-sheath, yielding us

$$\Phi_{fl} = -\frac{kT_e}{2e}\left[\ln\frac{m_i}{2\pi m_e} + 1\right] + \Phi_0 \tag{4.3.1}$$

$$= -0.537\,114\,\mathrm{V} \tag{4.3.2}$$

where Φ_0 is the plasma potential and is set to zero in our simulations (Shul and Pearton, 2000). Which is very close to the numerical result obtained from the simulation with a difference of $|\Delta\Phi_{fl}| = 0.060\,311\,\mathrm{V}$. The difference is a result of the analytical result being considered in the stationary case, in other words, in the case where there is no flow $M = 0$. In the case of the box, it might perhaps be different as the dimensions of the box is different. The box has a length of ten grid points in each direction corresponding to a length of $0.023\,44\,\mathrm{m}$ and comparing this with the Debye length used in the simulation which has the value $0.007\,43\,\mathrm{m}$ we see that it might actually lie in the border between thin and thick sheath region. The object is still larger than the Debye length and as such we should retain a similar value as in the case of the cylinder. In section 4.2.2 we noted the minimum negative potential for the box being $\Phi = -0.456\,539\,\mathrm{V}$ and we see that the floating potential for both the cylinder and the box does not deviate greatly from the analytical value with a difference of only $|\Delta\Phi_{fl}| = 0.080\,57\,\mathrm{V}$ in the case of the box despite the supersonic flow in the simulation and the eligibility of the analytical expression in the region. Were the dimensions of the box shorter than the Debye length then we would have to use the OML theory for verifying the floating potential as described in section 2.3.4.

Examining the potential for both cases we see a very different potential distribution behind the object. In the cylinder case there is a lot of fluctuations behind the object, as we discussed, resulting from the numerical errors while in the case of the box we see a significant rise in the potential. This ion focus region forming right behind the box, as evident in fig. 4.9a, arises not only due to geometry, but also the temperature. For large temperature ratios, as in our case, where we have $\frac{T_e}{T_i} = 10$ this is to be expected as it results in different thermal velocities of the particles and hence also different charge accumulation in different regions. For the region of interest to us, LEO, we would have a temperature ratio of approximately 2, however, because of the appeal of analysable results we have taken the temperature ratio as given in table 4.1. Had we taken the

more realistic temperature ratio we would not have had the observable results provided in section 4.2, particularly when it comes to the ion focus region and distinct wake structure.

We wrote in section 4.1.2 that we had a mass ratio of around 500 and this has been chosen for performance reasons. The real mass ratio between an ion and an electron is around 1836 (Gräff, Kalinowsky, and Traut, 2016). As reviewed above, the time scale that needs to be resolved is typically the electron plasma period, but since we have ions in our simulations it results in an additional longer time scale of the order of the ion plasma period. The plasma periods are proportional to the square-root of the mass, i.e. $\omega_p \propto \sqrt{m}$ (Bret and Dieckmann, 2010). Thus, applying a more realistic mass ratio would have resulted in a much longer simulation time.

In both simulations we use a flow speed of $M = 1.9$ and since we are in supersonic regime we expect to see a Mach angle of

$$\mu = \sin^{-1}\left(\frac{1}{M}\right) = 0.55$$

which converts to 32°. We had approximated this angle by using GIMP in the previous section and the approximation seems to fit well with the theoretical result, particularly for the box as there was a clearer Mach cone. It should however be noted that by using GIMP we approximated the angle graphically and thus it could digress by one or two degrees from the theoretical value.

The electric field for the two objects arising due to the charge distribution which causes the anisotropic potential distribution can be seen in figs. 4.8b and 4.14b for the cylinder and box respectively. The upstream part of the cylinder has significantly stronger field than the downstream and this can be seen again in the total density, fig. 4.8a, where the upstream has significantly more negative charge density than the downstream. We would expect to find the same in the case of the box, however, since the geometry is different we find that the electric field does not digress much in the case of the box, and this is mirrored in the charge density of the box in fig. 4.14a where we see that the charge density only occurs at the corners of the object and not on the edges of the upstream and downstream. Since we are using Cartesian grid we have build our geometry as described in section 4.1.1 by using the corners and are accordingly also subject to restrictions in the resolution, particularly when it comes to the cylinder. Given the above restrictions we cannot avoid corners even in the case of the cylinder which is why we can recapture the same charge density on the corners as seen in fig. 4.8a. The reason for the irregular distribution of the charge density lies also in the interaction of the flow around a refined or rigged object such as in our case.

Since our simulations are in the ES regime with no external magnetic field, it is far from the reality that is space. Had we included magnetic field in our

simulation, as the magnetic field described in section 2.1.2 we would have yielded very different results. Not only would the trajectory of the particles now be different, but they would be subject to the electromagnetic drift as described in section 2.2.2, that is if the fields were perpendicular to each other. This complexity could give rise to a different wake structure because of the magnetised electrons that drift with $\mathbf{v} = \frac{\mathbf{E}\times\mathbf{B}}{B^2}$ that follows from the electromagnetic field.

Correspondence with previous studies

The upstream part of the cylinder had more negative potential than the downstream as a consequence of the flow and the roughness of the object as observed in the box case where we had clear negative potential in the corners. This electric dipole moment had previously been observed in 2D (Miloch, 2006). There is also depletion of ion density observed in the wake as seen in figs. 4.6b and 4.12b which also has been shown in the studies of Y. Miyake et al., 2013; Wojciech J. Miloch, 2010. It is not only the ions that seem to be depleted in the wake, there is also depletion of electron density due to the ambipolarity of the electric field which results in acceleration of the electrons farther from the wake. In a paper describing the wake and the corresponding potential published by Eriksson et al., 2006 in which an electrostatic wake model is discussed affirms our findings in of the results above. The Mach cones observed in this thesis in which the object is larger than the characteristic Debye length has been studied by Allen, 2013. Even though the paper is based on gas dynamics theory and discusses the truncation of the Mach cone as a consequence, it does compare it with the PIC codes that have affirmed similar findings, still, we would like to argue that the Mach cone shape and the corresponding inner cones that arise are not only dependent on the temperature ratio, but also the shape of the object.

The anisotropic charging taking place in both the cylinder/rocket and box/satellite case aligns with the previous studies conducted in this field which has been observed by Y. Miyake et al., 2013; Wojciech J. Miloch, 2010 and others (Marchand et al., 2014). The central theme in the same references is also the wake formation behind the objects, varying in scale ranging from dust particles (Wojciech J. Miloch, 2010) to the Moon (Holmström et al., 2012), albeit in the latter work, a hybrid model was used which omitted some of the kinetic properties. In all the works we see similar observations when it comes to the Mach cone, potential, and ion focusing despite the different scales used in the simulations for different problems.

An important aspect of the simulation that we cannot neglect is of course the spacecraft charging leading to error in measurements. As we have seen in the result there is a significant wake forming behind the spacecraft. Had the spacecraft had Langmuir probes, or booms, used for measurements this would have caused errors in the measured data as a consequence of the wake disturbance on the surrounding plasma environment. This effect has been studied previously

by N. Meyer-Vernet, 1976 and simulations done by using the PIC have also been carried out by Y. Miyake et al., 2013, the latter showing the effects of the wake arising from the wire booms and the consequences it has on the electrostatic wake that is formed behind the spacecraft. The study done by N. Meyer-Vernet, 1976 show that as the spacecraft propels and spins in the plasma with the wire booms on the sides measuring plasma properties, there will be modulation. In references to the previous section we saw that different regions gave rise to different potentials around the spacecraft. In this scenario if we had booms on the sides of the spacecraft for measurement it would be subject to modulation by the crossing of the wire booms into the region of the wake. In the case of steady state with no wake the modulation would not be observed since we would be subject to equal potential in all directions, as contrary in the case of having a wake structure. The Cluster satellite had experienced modulation specially in the polar region. Papers related to the Cluster are published by Y. Miyake et al., 2013; Eriksson et al., 2006.

Chapter 5

Summary and conclusion

In this chapter we will summarise this thesis and go swiftly through the results obtained and finally conclude and ignite some ideas for future works.

5.1 Summary

In the first part of the simulation we presented the results obtained from the two different cases. Concerned with the geometry and dimensions of our objects we examined how their shapes affected the physical properties of the spacecrafts in plasma such as the potential, density, electric field and the aerodynamic structure, the wake, and its property, the Mach angle.

We examined the potential across the spacecrafts and discovered how they deviated from one another. For the rocket we examined the potential across the rocket and how a sheath is formed in the upstream and downstream by the electrons. The sheath was more thin in the upstream than the downstream, partially because of the wake structure forming behind it, but also because of the geometry. The same was observed in the case of the satellite where the sheath formation of negatively charged particles formed around the satellite. In the case of the latter though the thickness of the sheath was more or less equal in the upstream and downstream of the satellite. This could be observed by examining the electric field around the box in the direction of the flow. The bipolar electric field that originated from the anisotropic potential field had virtually equal intensity both in the upstream and downstream in the case of the satellite while the balance was more unequal in the case of the rocket. This was a consequence of the ion focusing forming behind the satellite as compared to the rocket case in which we had a electron wake formation as seen in fig. 4.6a and thereby leaving no room for the ion focusing to form. We mentioned that a factor for this could have been the object dimension relative to the flow velocity together with the temperature ratio. We know from previous work that the temperature ratio defines the wake structure and specially the ion focusing region as studied by Wojciech J. Miloch,

2010; Allen, 2013.

We further studied the wake around the two spacecrafts and how distinct it was in the case of the satellite than in the case of the rocket. Notably, there was a larger area of electron wake in the case of the rocket than in the case of the satellite which can be seen in figs. 4.6a and 4.12a. The basis of the observation was assigned to the geometry, dimension and flow, as these played larger roles when it came to the other properties such as the ambipolar electric field and potential. A consequence of this was the depletion of ions inside the wake and this could be observed in the density data as given in figs. 4.6b and 4.12b.

The depletion of ions inside the wake and the concentration of electrons inside the wake gives rise to a charge separation which forms an ambipolar electric field. This field will cause the forthcoming electrons to slow down or accelerate depending on the direction. Overall though, the total force on the particles would be zero as there is an equal force imposed by the ions outside the wake.

The ambipolar electric field and the anisotropic potential field has been observed by others, specially when it comes to the influence of the electrostatic wake on wire booms as employed by spacecrafts such as Cluster. Papers covering the wake formation around booms are published by Y. Miyake et al., 2013; Eriksson et al., 2006. The anisotropic potential that arises can have different effects on a spacecraft as the we covered in section 2.3.3 which includes spacecraft charging leading to damage, and modulation in measurements. The modulations are well covered by N. Meyer-Vernet, 1976 in which he examines the cause of the modulation by noting that during the spinning of the spacecraft the wire booms may enter the region of the wake which maintains a different potential than the region outside of the wake. In other words, the modulations arise from the rotation of the rocket and the direction of the booms through the wake structure forming behind the spacecraft.

5.2 Conclusion and future work

The simulations performed in this thesis by using the newly implemented algorithm for the object building seemed to play well with the original code as was written by Miloch, 2006. We examined two cases in the simulation corresponding to a rocket and a satellite in a LEO environment and studied some of the physics of the plasma on the spacecraft. We affirmed some of the foreseen results as predicted by the theory and previous works, such as the floating potential, electric field, wake structure and ion focusing region. We realised in the simulations that the object geometry played a very large role in the formation of the wake and charge distribution around the object. Specifically we discovered how different the electron wake structure was between the two cases and how intricate it would be if a magnetic field was involved.

The anisotropic potential giving rise to the electric field was very different in

the two cases which also gave rise to very different wake formations one completely void of any ions, fig. 4.6, and the other containing a focused ion region fig. 4.12. We suspected the cause being the flow velocity in the case of the rocket and in the case of the satellite we would suspect the lack of a large electron wake being the dimension of the box.

Despite the fluctuations in the various data set by only using 2×10^6 to 9×10^6 number of particles, we arrived at reasonable results. Increasing the particles would have helped in smoothing the result variations, it would however not improved our results significantly. Instead we would liked to have saved the data at shorter intervals corresponding to the ion plasma period such that we could perhaps minimise the fluctuations and thus see if there indeed is an ion wake structure further behind the object or not. When it comes to the parameter of the simulations, they were chosen as close to the LEO environment as possible, despite some of the evident differences in terms of temperature ratio and mass ratio that were chosen as prescribed for performance reasons. It would be interesting to see if we could include the full photoemission effect that takes place in the GEO region and perform a simulation related to that. A problem would be the flow velocity as in GEO we have spacecraft velocity equal to the rotational velocity of the Earth, but we covered in section 2.3.3 that bulk charging could occur during shadows, but for this we would need to expand the code further to include this effect and research into this area is still in its infancy.

Geometry wise the algorithm can be improved to include variations in the z-axis such that we could build more complex geometries by linking it to an external CAD program. Another approach would be to actually read the data file from an external CAD program such as AutoCAD. Ideally it would be better to rewrite the code to make use of finite-element method instead of finite-difference on a Cartesian grid as it is here. This would allows us to expand get detailed analysis of very complex and realistic shapes. The use of FEM to simulate complex shapes in plasma has already proven to coincide with experiments performed in laboratory to simulate ion thrusters and even spacecrafts. Some of the research has already been published by D. Han, Wang, and He, 2016; Daoru Han et al., 2016.

Nevertheless the present code is very well established when it comes to the study of the dust particles in space plasma and has previously been covered by the original author of the code in W. J. Miloch et al., 2009. If we however wish to expand the code into more intricate regions and include complex geometries we should research into other methods such as those mentioned above.

Appendix A

Derivation of the orbit equation

Newton's law of universal gravitation is given by

$$\mathbf{F}_{21} = -\frac{Gm_1m_2}{\|\mathbf{r}\|^2}\hat{\mathbf{u}} = -\frac{Gm_1m_2}{r^2}\hat{\mathbf{u}} \tag{A.0.1}$$

which defines a force acting on a body with mass m_2 by a body with mass m_1. We note that since we are using inertial coordinate system we can easily differentiate the position vector $\mathbf{r}$ without consideration for the derivative of each axes of the coordinate system. By applying Newton's second law on the body with mass, m_2, we get

$$-\frac{Gm_1m_2}{r^2}\hat{\mathbf{u}} = m_2\ddot{\mathbf{r}}_\mathbf{2} \tag{A.0.2}$$

By Newton's third law of action-reaction we have $\mathbf{F}_{12} = -\mathbf{F}_{21}$ thus for the body of mass m_1 we have

$$\frac{Gm_1m_2}{r^2}\hat{\mathbf{u}} = m_1\ddot{\mathbf{r}}_\mathbf{1} \tag{A.0.3}$$

We can then solve the above equations by multiplying eq. (A.0.2) with m_1 and eq. (A.0.3) with m_2 then subtracting the second equation from the first, yielding us

$$\ddot{\mathbf{r}} = -\frac{G(m_1+m_2)}{r^2}\hat{\mathbf{u}} = -\frac{\mu}{r^2}\hat{\mathbf{u}} \tag{A.0.4}$$

eq. (A.0.4) describes the motion of m_2 relative to m_1. We have here defined the gravitational parameter $\mu = G(m_1 + m_2)$ or in the case of Earth-satellite $\mu = Gm_\oplus$, where $m_\oplus$ is the Earth mass, we have omitted the satellite mass as it is negligible. We have to note that we have made assumptions in the derivation such as the bodies being spherically symmetric with uniform density and that there are no other forces acting on the bodies except the gravitational force. (Vallado, 2001).

Before proceeding, we shortly review the specific angular momentum as it is constant and independent of mass (Curtis, 2010; Vallado, 2001). This can easily

Figure A.1: Cone-section showing the different possible orbits (modified from GitHub by Ridlo W. Wibowo).

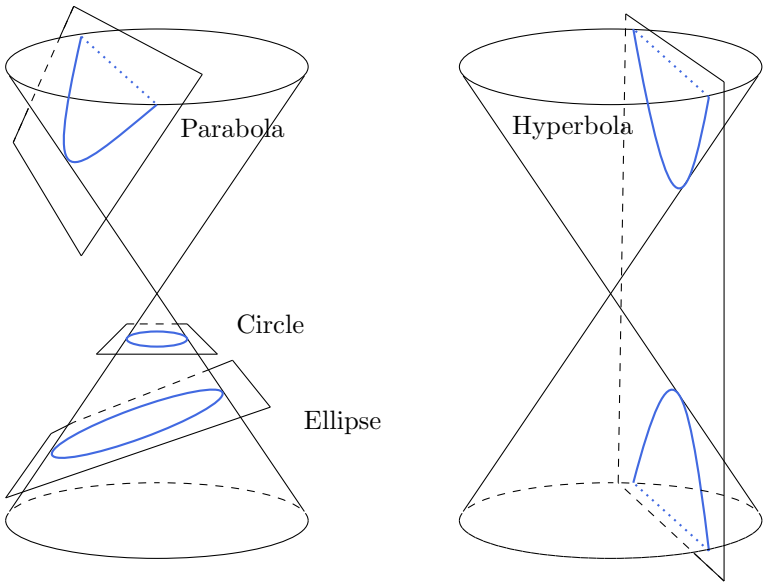

be verified by taking $\times\mathbf{r}$ of eq. (A.0.4)

$$\mathbf{r} \times \ddot{\mathbf{r}} + \mathbf{r} \times \frac{\mu}{r^3}\mathbf{r} = 0 \tag{A.0.5}$$

the latter term vanishes as $\mathbf{r} \times \mathbf{r} = 0$ and furthermore we know from the product rule of differentiation $\frac{\mathrm{d}}{\mathrm{d}t}(\mathbf{r} \times \dot{\mathbf{r}}) = \dot{\mathbf{r}} \times \dot{\mathbf{r}} + \mathbf{r} \times \ddot{\mathbf{r}} = \mathbf{r} \times \ddot{\mathbf{r}}$ We can see that we can insert the above derivative into eq. (A.0.5), but then the result would be zero, thus the internal quantity must be a constant, $\mathbf{h}$. In other words, $\frac{\mathrm{d}\mathbf{h}}{\mathrm{d}t} = 0$, or $\mathbf{r} \times \dot{\mathbf{r}} =$ constant Curtis, 2010. Rearranging and substituting eq. (A.0.5) and we will have

$$\mathbf{h} = \mathbf{r} \times \mathbf{v} \tag{A.0.6}$$

which means that at any given time the two vectors $\mathbf{r}$ and $\mathbf{v}$ lie in the same plane and their cross product is perpendicular to that plane and for a satellite its motion is always confined to this plane, the orbital plane. (Vallado, 2001; Curtis, 2010) Most of the relevant orbits can be looked at by the intersection of a plane and a cone as in fig. A.1. By which we can derive the conic sections: circle, ellipse, parabola and hyperbola. Kepler's first law states that planets orbit in an ellipse, one of the conic sections. The two-body equation A.0.4 describes the path of a small body orbiting a larger body, thus we can derive a trajectory equation that describes these motions. We cross eq. (A.0.4) with eq. (A.0.6)

$$\ddot{\mathbf{r}} \times \mathbf{h} + \frac{\mu}{r^3}\mathbf{r} \times \mathbf{h} = 0 \tag{A.0.7}$$

By using the same argument as the one during the specific angular momentum the first term is then simply

$$\frac{\mathrm{d}}{\mathrm{d}t}(\dot{\mathbf{r}} \times \mathbf{h}) = \ddot{\mathbf{r}} \times \mathbf{h}$$

because $\dot{\mathbf{h}} = 0$. For the second term we substitute eq. (A.0.6) into eq. (A.0.7) and we note from vector calculus the cross product identity $\mathbf{r} \times (\mathbf{r} \times \mathbf{v}) = \mathbf{r}(\mathbf{r} \cdot \mathbf{v}) - \mathbf{v}(\mathbf{r} \cdot \mathbf{r})$. By using these and simplifying we get

$$\frac{\mu}{r^3}(\mathbf{r} \times \mathbf{h}) = \frac{\mu}{r^2}\dot{r}\mathbf{r} - \frac{\mu}{r}\mathbf{v} = -\mu\frac{\mathrm{d}}{\mathrm{d}t}\left(\frac{\mathbf{r}}{r}\right)$$

where we have identified the quotient rule for the last part. Now that we have an expression both for the first and second term we can substitute the two into eq. (A.0.7) and produce

$$\frac{\mathrm{d}}{\mathrm{d}t}(\dot{\mathbf{r}} \times \mathbf{h}) = \mu\frac{\mathrm{d}}{\mathrm{d}t}\left(\frac{\mathbf{r}}{r}\right) \tag{A.0.8}$$

Integrating both sides gives us

$$\dot{\mathbf{r}} \times \mathbf{h} - \mu\frac{\mathbf{r}}{r} = \mathbf{C} \tag{A.0.9}$$

where the vector $\mathbf{C}$ is an arbitrary constant of integration having dimensions μ and lies on the orbital plane since the right-hand side is normal to the angular momentum (Vallado, 2001; Curtis, 2010). Now we take $\cdot\mathbf{h}$ of the above equation and

$$(\dot{\mathbf{r}} \times \mathbf{h}) \cdot \mathbf{h} - \mu\frac{\mathbf{r}}{r} \cdot \mathbf{h} = \mathbf{C} \cdot \mathbf{h}$$

Both the first and second term of the left-hand side vanish as a result of perpendicularity and we retrieve $\mathbf{C} \cdot \mathbf{h} = 0$ this means that $\mathbf{C}$ is perpendicular to $\mathbf{h}$ which is normal to the orbital plane. We can now rearrange eq. (A.0.9) and get

$$\frac{\mathbf{r}}{r} + \mathbf{e} = \frac{\dot{\mathbf{r}} \times \mathbf{h}}{\mu} \tag{A.0.10}$$

where $\mathbf{e} = \frac{\mathbf{C}}{\mu}$ is the eccentricity vector. To get the scalar of this we take the $\cdot\mathbf{r}$ of the above equation and employ the vector identity $\mathbf{r} \cdot (\dot{\mathbf{r}} \times \mathbf{h}) = ()\mathbf{r} \times \dot{\mathbf{r}}) \cdot \mathbf{h} = \mathbf{h} \cdot \mathbf{h} = h^2$, resulting in

$$r + \mathbf{r} \cdot \mathbf{e} = \frac{h^2}{\mu}$$
$$r + re\cos(\theta) = \frac{h^2}{\mu}$$

where we have made use of the dot product definition. Rearranging the above once again and we retrieve the orbit equation

$$r = \frac{h^2}{\mu} \frac{1}{1 + e\cos(\theta)} \tag{A.0.11}$$

here θ is the true anomaly (Curtis, 2010) i.e. the angle between the eccentricity vector and the variable position vector. An important parameter in eq. (A.0.11)is the eccentricity, e, which indicates the orbit's "roundness" or its deviation from begin a circle. What we have derived describes the path of the body m_2 around m_1 relative to m_1 e.g. a satellite around Earth. It is essentially a mathematical statement of Kepler's first law which we have extended beyond an ellipse to any cone section as in fig. A.1.

Appendix B

Derivation of Boltzmann moments

We have the BTE as

$$\frac{\partial f_s}{\partial t} + \frac{\partial}{\partial x_i}(f_s v_i) + \frac{\partial}{\partial v_i}(f_s a_i) = C_s(f) \tag{B.0.1}$$

where we are using the tensor notation where x_i for $i = 1, 2, 3$ and s denotes species. To find the corresponding equations; the continuity equation, momentum equation and energy conservation equation, we take the moments of the above. We define the moments by multiplying the distribution function with velocities and integrating over the velocity space (Fitzpatrick, 2015).

In the subsequent derivations we wish to extract time evolution of the mass density, the fluid velocity and the specific internal energy, denoted by ρ,$\mathbf{u}$ and ε respectively. To find these we have to multiply eq. (B.0.1) with $\xi(\mathbf{v})$ where ξ represents any constant of power of $\mathbf{v}$, which for the above will be

$$\xi = m \qquad \xi = \mathbf{v} \qquad \xi = \frac{1}{2}m|\mathbf{v}|^2 \tag{B.0.2}$$

and then integrating over all $\mathbf{v}$. Any linear combinations of the above will work too. We will also note that

$$\int \xi C_s(f)\, \mathrm{d}^3 v = 0$$

in which ξ is a conserved quantity in a collision such that the above is valid in a non-relativistic regime involving short-range forces. In other words, collisions do not contribute to any time rate of change of any of the above conserved quantities during the collision process.

The continuity equation

Multiplying eq. (B.0.1) with $\xi = m_s v_i^0$ and we obtain

$$\frac{\partial}{\partial t}\int m_s f_s \,\mathrm{d}^3 v + \frac{\partial}{\partial x_i}\int m_s f_s v_i \,\mathrm{d}^3 v + \int \frac{\partial}{\partial v_i} m_s f_s a_i \,\mathrm{d}^3 v = 0 \tag{B.0.3}$$

We cannot perform much simplification to the current equation, however, if we denote a new term namely the number density (Fitzpatrick, 2015) n_s,

$$n_s(x_i, t) = \int f_s(x_i, v_i, t)\,\mathrm{d}^3 v \tag{B.0.4}$$

which is the number of particles in the velocity space and the corresponding mass density $\rho_s = m_s n_s$. The average of an arbitrary quantity such as Q is given by

$$\langle Q \rangle = \frac{1}{n_s}\int Q f_s(x_i, v_i, t)\mathrm{d}^3 v$$

such that substituting Q with v_i yields

$$\rho_s u_{i,s}(x_i, t) = \rho_s \langle v_i \rangle = \int v_i f_s(x_i, v_i, t)\,\mathrm{d}^3 v \tag{B.0.5}$$

where $u_{i,s}$ is the flow velocity. We can now simplify eq. (B.0.3) by recognising the above two such that the first term is simply

$$\frac{\partial}{\partial t}\int m_s f_s \,\mathrm{d}^3 v = \frac{\partial \rho_s}{\partial t}$$

and the second term

$$\frac{\partial}{\partial x_i}\int m_s f_s v_i \,\mathrm{d}^3 v = \frac{\partial}{\partial x_i}(\rho_s u_{i,s})$$

furthermore the third term of eq. (B.0.3) becomes

$$\iiint_V \boldsymbol{\nabla} \cdot (\mathbf{a}_s f_s)\,\mathrm{d}^3 v = \iint_S \hat{\mathbf{n}} \cdot (\mathbf{a}_s f_s)\,\mathrm{d}A = 0$$

Here we have applied the divergence theorem where $\mathrm{d}A$ is the surface area of the velocity space, furthermore we have assumed that $f_s \to 0$ as $v \to \infty$ since f_s vanishes faster than any power of $\mathbf{v}$. Gathering the above having applied the collision conversation law we initially mentioned, we retrieve the continuity equation (Fitzpatrick, 2015)

$$\frac{\partial \rho_s}{\partial t} + \frac{\partial}{\partial x_i}(\rho_s u_{i,s}) = 0 \tag{B.0.6}$$

The equation implies that local matter content due to fluid flow occurs in a continuous fashion. The mass flows thereby in a well-defined manner across the surface of the volume as opposed to disconnected in which it would disappear suddenly and reappear in some completely different region.

The momentum conservation equation

We multiply eq. (B.0.1) with $\xi = m_s v_j$ to obtain

$$m_s \frac{\partial}{\partial t} \int f_s v_j \, \mathrm{d}^3 v + m_s \frac{\partial}{\partial x_i} \int f_s v_i v_j \, \mathrm{d}^3 v + m_s \int \frac{\partial}{\partial v_i} f_s v_j a_i \, \mathrm{d}^3 v = 0 \tag{B.0.7}$$

From the previous case we can already recognise the first term as

$$\frac{\partial}{\partial t} \int m_s f_s v_j \, \mathrm{d}^3 v = \frac{\partial}{\partial t} (\rho_s u_{j,s})$$

For the second term we introduce the relative velocity $w_s = v - u_s$ such that (see Fitzpatrick, 2015)

$$\frac{\partial}{\partial x_i} (\rho_s \langle v_j v_i \rangle) = \frac{\partial}{\partial x_i} (\rho_s u_{i,s} u_{j,s} + \rho_s \langle w_{i,s} w_{j,s} \rangle)$$

the inner term $\rho_s \langle w_{i,s} w_{j,s} \rangle$ denotes the pressure tensor which depends only on the random velocity of the particles (Shu, 2009). It is convenient to rewrite it as

$$\rho_s \langle w_{i,s} w_{j,s} \rangle = \frac{1}{3} \rho_s \langle |\mathbf{w}_s|^2 \rangle - P \delta_{ij} - \rho_s \langle w_{i,s} w_{j,s} \rangle$$

The first term on the RHS is the pressure $P \equiv \frac{1}{3} \rho_s \langle |\mathbf{w}_s|^2 \rangle$ and the second term is the viscous stress tensor $\nu \equiv P \delta_{ij} - \rho_s \langle w_{i,s} w_{j,s} \rangle$ where δ_{ij} is the Kronecker delta. For the third term in eq. (B.0.3) we make use of the divergence theorem together with the previous argument that $f_s \to 0$ as $v_i \to \infty$ to obtain

$$m_s a_i \int \left[\frac{\partial}{\partial v_i} (v_j f_s) - \delta_{ij} f_s \right] \mathrm{d}^3 v = -a_i \delta_{ij} \int m_s f_s \, \mathrm{d}^3 v = \rho_s a_j \tag{B.0.8}$$

Setting the pieces together yields

$$\frac{\partial}{\partial t} (\rho_s u_{j,s}) + \frac{\partial}{\partial x_i} (\rho_s u_{j,s} u_{i,s} + P \delta_{ij} - \nu_{ij}) = \rho_s a_j$$

Which is the momentum equation that tells us that the time derivative of a conserved quantity together with the divergence of a flux equals a source term (Shu, 2009).

The energy equation

To find the energy equation we multiply eq. (B.0.1) with $\xi = \frac{1}{2} m |\mathbf{v}|^2$. For a detailed derivation of the following see Shu, 2009. The general idea is however to make use of the divergence theorem and conservation of collision energy, mass and momentum to yield

$$\frac{\partial}{\partial t} \left(\frac{1}{2} \rho_s |\mathbf{u}|^2 + \frac{3}{2} P \right) + \frac{\partial}{\partial x_i} \left[\frac{1}{2} \rho_s |\mathbf{u}|^2 u_i + u_j (P \delta ij - \nu_{ij}) + \frac{3}{2} P u_i + F_i \right] = -\rho_s u_i a_i \tag{B.0.9}$$

where $F_i = \rho\langle w_i \frac{1}{2}|\mathbf{w}|^2\rangle$ is the conduction heat flux. The above equation states that the total fluid energy density is the sum of a part due to $\rho_s|\mathbf{u}|^2$, which is the bulk motion, and a part due to random motions $\rho\varepsilon = \frac{3}{2}P$. The flux of the energy in the ith direction consists of $(\frac{1}{2}\rho_s|\mathbf{u}|^2)u_i$, $(\rho\varepsilon + P)u_i$ and $-u_i\nu_{ij}$ corresponding to the mean velocity, enthalpy, and the viscous contribution respectively (Shu, 2009).

Appendix C

Code

C.1 polyfill.c

```
#include <stdio.h>
#include <stdlib.h>
#include "const.h"

#define min(a,b) (((a)<(b))?(a):(b))
#define max(a,b) (((a)>(b))?(a):(b))

/*
--------------------------------------------------------------------------
                The following function will scan and fill the region of
                the object, boundary, and outside as desired.
                x: array of x-coordinates
                y: array of y-coordinates
                vox: zero 3D array with index sorting provided by ix(0,i,j,k)
                corners: number of corners for the desired region of confinment
                max_corners: the maximum number of corners the object could have
                ngx: number of grid points in the x direction
                ngy: number of grid points in the y direction
                newN: the new number you would like to replace the previous number with
                z: z direction coordinate.
--------------------------------------------------------------------------
*/
void scanFill(int *x, int *y, int *vox, int corners, int max_corners,int ngx, int ngy,int
 ↪   newN, int z){
        int  nodes, nodeX[max_corners], gridX, gridY, i, j, swap ;
        //  Scan through the grid in the y-direction.
        for (gridY=0; gridY<ngy; gridY++) {

                //  Build a list of nodes.
                nodes=0; j=corners-1;
                for (i=0; i<corners; i++) {
                        if ( (y[i]<(double) gridY && y[j]>=(double) gridY) ||
 ↪   (y[j]<(double) gridY && y[i]>=(double) gridY)){
                                nodeX[nodes++]=(int)
 ↪   (x[i]+(gridY-y[i])/(y[j]-y[i])*(x[j]-x[i]));
                        }
                        j=i;
                }

                //  Bubble-sort the nodes.
```

```
38                  i=0;
39                  while (i<nodes-1) {
40                          if (nodeX[i]>nodeX[i+1]) {
41                                  swap=nodeX[i]; nodeX[i]=nodeX[i+1]; nodeX[i+1]=swap;
42                                  if (i) i--;
43                          }
44                          else {
45                                  i++; }
46                          }
47
48                  //  Fill in between the nodes.
49                  for (i=0; i<nodes; i+=2) {
50                          if   (nodeX[i  ]>=ngx) break;
51                          if   (nodeX[i+1]> 0 ) {
52                                  if (nodeX[i  ]< 0 ) nodeX[i  ]=0 ;
53                                  if (nodeX[i+1]> ngx) nodeX[i+1]=ngx;
54                                  for (gridX=nodeX[i]; gridX<nodeX[i+1]; gridX++){
55                                          vox[ix(0,gridX,gridY,z)]=newN;
56                                  }
57                          }
58                  }
59          }
60  }
61
62  // Finding the max and minimum value of an array
63  int amax(int *arr,int elements){
64          int i, max;
65          max = 0;
66          for (i = 0; i < elements; ++i ){
67                  if (arr[i]>max){
68                          max=arr[i];
69                  }
70          }
71          return max;
72  }
73
74  int amin(int *arr,int elements){
75          int i, min;
76          min = ngx_MAX;
77          for (i = 0; i < elements; ++i ){
78                  if (arr[i]<min){
79                          min=arr[i];
80                  }
81          }
82          return min;
83  }
```

C.2 grid.c (modified part)

```
556                 int ilevoxeli=0;
557                 int flag=0;
558                 int done=0;
559                 int ii,jj,kk;
560                 int corners=240;
561                 int in, s;
562
563                 corner_x=ivecmem(0,corners-1);
564                 corner_y=ivecmem(0,corners-1);
565                 corner_z=ivecmem(0,corners-1);
566                 //read in the coordinates from file
```

```
567                 FILE *coor = fopen("cylinder_z50.txt", "r");
568                 for (in = 0; in < corners; ++in){
569                         fscanf(coor, "%d %d %d", &corner_x[in], &corner_y[in],
    ↪   &corner_z[in]);
570                 }
571                 fclose(coor);
572 
573                 //-----------------------Object marking starts here-----------------------
574                 // Here we construct the box around the object
575                 // for later versions might need to substitute
576                 // box with an bigger sized object outline.
577                 int le=corners-1; //last element
578                    int *xbox, *ybox;
579                    int boxcorners = 4;
580                    xbox = ivecmem(0,boxcorners-1);
581                    ybox = ivecmem(0,boxcorners-1);
582                    xbox[0] = amin(corner_x,corners/2)-bufzone;
    ↪   ybox[0]=amax(corner_y,corners/2)+bufzone;
583                    xbox[1] = amax(corner_x,corners/2)+bufzone;
    ↪   ybox[1]=amax(corner_y,corners/2)+bufzone;
584                    xbox[2] = amax(corner_x,corners/2)+bufzone;
    ↪   ybox[2]=amin(corner_y,corners/2)-bufzone;
585                    xbox[3] = amin(corner_x,corners/2)-bufzone;
    ↪   ybox[3]=amin(corner_y,corners/2)-bufzone;
586 
587                 for (kk = 0; kk < ngz; ++kk){
588                         // The following loop will initialise the outline marking of the
    ↪   box
589                         if ( (kk>=amin(corner_z,corners) && kk<=amax(corner_z,corners))){
590                                 for (ii = 0; ii < ngx; ++ii){
591                                         for (jj = 0; jj < ngy; ++jj){
592                                                 for (s = 0; s < boxcorners; ++s){
593                                                         if ( ((ii>=min(xbox[s],xbox[le]))
    ↪   && (ii<=max(xbox[s],xbox[le])) && (jj==ybox[s]) )||
594                                                                 (((ii==xbox[s]) &&
    ↪   (jj>=min(ybox[s],ybox[le])) && (jj<=max(ybox[s],ybox[le])))) ){
595                                                                         phivoxel[ix(0,ii,jj,kk)]
    ↪   = 1;
596                                                         }
597                                                 le=s;
598                                                 }
599                                         }
600                                 }
601 
602                                 // The line will fill the outlined box with the value 1
603                                 scanFill(xbox, ybox, phivoxel, boxcorners,
    ↪   4,ngx,ngy,1,kk);
604                                 // The line will fill all of the object incl. edges and
    ↪   inside with value 3
605                                 scanFill(corner_x, corner_y, phivoxel, corners/2,
    ↪   corners,ngx,ngy,3,kk);
606 
607                                 // Changing the value of the edges to have the value 2
608                                 for (ii = 0; ii < ngx; ++ii){
609                                         for (jj = 0; jj < ngy; ++jj){
610                                                 for (s = 0; s < corners; ++s){
611                                                         if (
    ↪   ((ii>=min(corner_x[s],corner_x[le])) && (ii<=max(corner_x[s],corner_x[le])) &&
    ↪   (jj==corner_y[s]) )||
612                                                                 (((ii==corner_x[s]) &&
    ↪   (jj>=min(corner_y[s],corner_y[le])) && (jj<=max(corner_y[s],corner_y[le])))) ){
613                                                                         phivoxel[ix(0,ii,jj,kk)]
    ↪   = 2;
```

```
                                                    }
                                                le=s;
                                            }
                                        }
                                    }
                            }
                            // The following will mark the box in the z dir.
                               if ((kk>=amin(corner_z,corners)-bufzone &&
    ↪   kk<amin(corner_z,corners)) || (kk<=amax(corner_z,corners)+bufzone &&
    ↪   kk>amax(corner_z,corners))){
                                    scanFill(xbox, ybox, phivoxel, boxcorners,
    ↪   4,ngx,ngy,1,kk);
                               }
                               // This one will mark the surface at min max z dir.
                               if (kk==amin(corner_z,corners) || kk==amax(corner_z,corners)){
                                    scanFill(corner_x, corner_y, phivoxel, corners/2,
    ↪   corners,ngx,ngy,2,kk);

                               }
                    }
                       //----------------Object marking ends here
    ↪   ----------------------------------------

                    for ( ii = 0; ii < ngx; ++ii){
                            for ( jj = 0; jj < ngy; ++jj){
                                    for ( kk = 0; kk < ngz; ++kk){
                                            if (phivoxel[ix(0,ii,jj,kk)]==2){
                                                    ilevoxeli++;
                                            }
                                    }
                            }
                    }

                    FILE *objmarktest = fopen("obj_mark_test.txt","w");
                    //TEST: print it on screen for
                    int ko;
                    for (ko = amin(corner_z,corners); ko < amax(corner_z,corners)+1; ++ko){

                            for(ii=0; ii<ngx; ii++)
                              {
                                    for(jj=0; jj<ngy; jj++)
                                      {
                                    // printf("%d ", phivoxel[ix(0,ii,jj,10)]);
                                    fprintf(objmarktest,"%d",phivoxel[ix(0,ii,jj,ko)]);
                                      }
                                    // printf("\n");
                                    fprintf(objmarktest, "\n");

                            }
                    }
                    fclose(objmarktest);
                    printf("ilevoxeli %d \n", ilevoxeli);
                    getchar();
```

Bibliography

[1] J. E. Allen. "On supersonic plasma flow around an obstacle". In: *Journal of Plasma Physics* 79.3 (June 2013), pp. 315–319. ISSN: 0022-3778, 1469-7807. DOI: 10.1017/S0022377812001031. URL: https://www.cambridge.org/core/journals/journal-of-plasma-physics/article/on-supersonic-plasma-flow-around-an-obstacle/270CC06591DC39AF1F6B082E19E5EE31 (visited on 09/22/2016).

[2] J. E. Allen. "Probe theory - the orbital motion approach". en. In: *Physica Scripta* 45.5 (1992), p. 497. ISSN: 1402-4896. DOI: 10.1088/0031-8949/45/5/013. URL: http://stacks.iop.org/1402-4896/45/i=5/a=013 (visited on 08/05/2016).

[3] Wolfgang Baumjohann and Rudolf A Treumann. *Basic space plasma physics*. Imperial College Press, 1996.

[4] Keith Bedingfield, Richard D. Leach, and Margaret B. Alexander. *Spacecraft System Failures and Anomalies Attributed to the Natural Space Environment*. Tech. rep. Aug. 1996. URL: http://ntrs.nasa.gov/search.jsp?R=19960050463 (visited on 08/02/2016).

[5] C. K. Birdsall and A. B. Langdon. *Plasma Physics via Computer Simulation*. Google-Books-ID: S2lqgDTm6a4C. CRC Press, Oct. 1, 2004. 506 pp. ISBN: 978-0-7503-1025-3.

[6] J. A. Bittencourt. *Fundamentals of Plasma Physics*. en. New York, NY: Springer New York, 2004. ISBN: 978-1-4419-1930-4 978-1-4757-4030-1. URL: http://link.springer.com/10.1007/978-1-4757-4030-1 (visited on 07/23/2016).

[7] Professor Asgeir Brekke. "The Sun and the solar wind". en. In: *Physics of the Upper Polar Atmosphere*. Springer Atmospheric Sciences. DOI: 10.1007/978-3-642-27401-5_1. Springer Berlin Heidelberg, 2013, pp. 1–50. ISBN: 978-3-642-27400-8 978-3-642-27401-5. URL: http://link.springer.com/chapter/10.1007/978-3-642-27401-5_1 (visited on 07/15/2016).

[8] A. Bret and M. E. Dieckmann. "How large can the electron to proton mass ratio be in Particle-In-Cell simulations of unstable systems?" In: *Physics of Plasmas* 17.3 (2010), p. 032109. ISSN: 1070664X. DOI: 10.1063/1.3357336. arXiv: 1002.4741. URL: http://arxiv.org/abs/1002.4741 (visited on 09/28/2016).

[9] Francis F. Chen. *Introduction to Plasma Physics and Controlled Fusion*. en. Boston, MA: Springer US, 1984. ISBN: 978-1-4419-3201-3 978-1-4757-5595-4. URL: http://link.springer.com/10.1007/978-1-4757-5595-4 (visited on 07/22/2016).

[10] Mengu Cho. "Failure mechanisms and protection methods of spacecraft power system". In: *Electrical Insulating Materials, 2005.(ISEIM 2005). Proceedings of 2005 International Symposium on*. Vol. 1. IEEE. 2005, pp. 45–48.

[11] Howard D. Curtis. "Chapter 2 - The Two-Body Problem". In: *Orbital Mechanics for Engineering Students (Second Edition)*. Aerospace Engineering. Boston: Butterworth-Heinemann, 2010, pp. 61–153. ISBN: 978-0-12-374778-5. URL: http://www.sciencedirect.com/science/article/pii/B9780123747785000027 (visited on 07/19/2016).

[12] John M. Dawson. "Particle simulation of plasmas". In: *Reviews of Modern Physics* 55.2 (Apr. 1, 1983), pp. 403–447. DOI: 10.1103/RevModPhys.55.403. URL: http://link.aps.org/doi/10.1103/RevModPhys.55.403 (visited on 08/19/2016).

[13] Sherman E DeForest. "Spacecraft charging at synchronous orbit". In: *Journal of Geophysical Research* 77.4 (1972), pp. 651–659.

[14] A. I. Eriksson et al. "Electric field measurements on Cluster: comparing the double-probe and electron drift techniques". In: *Ann. Geophys.* 24.1 (Mar. 7, 2006), pp. 275–289. ISSN: 1432-0576. DOI: 10.5194/angeo-24-275-2006. URL: http://www.ann-geophys.net/24/275/2006/ (visited on 09/25/2016).

[15] Richard Fitzpatrick. *Plasma Physics: An Introduction*. English. 1 edition. Boca Raton: CRC Press, Aug. 2015. ISBN: 978-1-4665-9427-2.

[16] James D. Foley et al. *Computer Graphics, reissued 2nd Ed.* 2 edition. Reading, Mass: Addison Wesley, Sept. 1995. 1200 pp. ISBN: 978-0-201-84840-3.

[17] Henry B. Garrett and Albert C. Whittlesey. *Guide to Mitigating Spacecraft Charging Effects*. English. 1 edition. Hoboken, N.J: Wiley, May 2012. ISBN: 978-1-118-18645-9.

[18] G. Gräff, H. Kalinowsky, and J. Traut. "A direct determination of the proton electron mass ratio". In: *Zeitschrift für Physik A Atoms and Nuclei* 297.1 (), pp. 35–39. ISSN: 0939-7922. DOI: 10.1007/BF01414243. URL: http://link.springer.com/article/10.1007/BF01414243 (visited on 09/28/2016).

[19] Yu N. Grigoryev, V. A. Vshivkov, and M. P. Fedoruk. *Numerical Particle-in-Cell Methods: Theory and Applications*. Reprint 2012 ed. edition. Utrecht; Boston: de Gruyter, July 26, 2002. 260 pp. ISBN: 978-90-6764-368-9.

[20] D. Han, J. Wang, and X. He. "A Nonhomogeneous Immersed-Finite-Element Particle-in-Cell Method for Modeling Dielectric Surface Charging in Plasmas". In: *IEEE Transactions on Plasma Science* 44.8 (Aug. 2016), pp. 1326–1332. ISSN: 0093-3813. DOI: 10.1109/TPS.2016.2580698.

[21] Daoru Han et al. "A 3D immersed finite element method with non-homogeneous interface flux jump for applications in particle-in-cell simulations of plasma–lunar surface interactions". In: *Journal of Computational Physics* 321 (Sept. 15, 2016), pp. 965–980. ISSN: 0021-9991. DOI: 10.1016/j.jcp.2016.05.057. URL: http://www.sciencedirect.com/science/article/pii/S0021999116302029 (visited on 09/26/2016).

[22] R. W. Hockney and J. W. Eastwood. *Computer Simulation Using Particles*. en. Google-Books-ID: nTOFkmnCQuIC. CRC Press, Jan. 1988. ISBN: 978-1-4398-2205-0.

[23] M. Holmström et al. "The interaction between the Moon and the solar wind". In: *Earth, Planets and Space* 64.2 (Feb. 2012), pp. 237–245. ISSN: 1343-8832, 1880-5981. DOI: 10.5047/eps.2011.06.040. arXiv: 1104.1440. URL: http://arxiv.org/abs/1104.1440 (visited on 09/22/2016).

[24] Stephen Jardin. *Computational Methods in Plasma Physics*. English. 1 edition. Boca Raton: CRC Press, June 2010. ISBN: 978-1-4398-1021-7.

[25] Giovanni Lapenta. *Particle In Cell Methods*. URL: http://citeseerx.ist.psu.edu/viewdoc/download?doi=10.1.1.471.420&rep=rep1&type=pdf (visited on 08/22/2016).

[26] Giovanni Lapenta, J. U. Brackbill, and Paolo Ricci. "Kinetic approach to microscopic-macroscopic coupling in space and laboratory plasmasa)". In: *Physics of Plasmas (1994-present)* 13.5 (May 1, 2006), p. 055904. ISSN: 1070-664X, 1089-7674. DOI: 10.1063/1.2173623. URL: http://scitation.aip.org/content/aip/journal/pop/13/5/10.1063/1.2173623 (visited on 08/21/2016).

[27] R. D. Leach and M. B. Alexander. *Failures and anomalies attributed to spacecraft charging*. Tech. rep. Aug. 1995. URL: http://ntrs.nasa.gov/search.jsp?R=19960001539 (visited on 08/02/2016).

[28] Ling-Hsiao Lyu. *Elementary space plasma physics*. Chapter 2. Airiti Press Incorporated, 2014.

[29] R. Marchand et al. "Cross-comparison of spacecraft-environment interaction model predictions applied to Solar Probe Plus near perihelion". In: *Physics of Plasmas (1994-present)* 21.6 (June 1, 2014), p. 062901. ISSN: 1070-664X, 1089-7674. DOI: 10.1063/1.4882439. URL: http://scitation.aip.org/content/aip/journal/pop/21/6/10.1063/1.4882439 (visited on 09/22/2016).

[30] N. Meyer-Vernet. "Rocket spin effects on the current collected by a cylindrical probe in the ionosphere". In: *Journal of Geophysical Research* 81.4 (Feb. 1, 1976), pp. 450–456. ISSN: 2156-2202. DOI: 10.1029/JA081i004p00450. URL: http://onlinelibrary.wiley.com/doi/10.1029/JA081i004p00450/abstract (visited on 09/22/2016).

[31] Nicole Meyer-Vernet. *Basics of the Solar Wind*. Cambridge Books Online. Cambridge University Press, 2007. ISBN: 9780511535765. URL: http://dx.doi.org/10.1017/CBO9780511535765.

[32] Tsoline Mikaelian. "Spacecraft Charging and Hazards to Electronics in Space". In: *arXiv:0906.3884 [physics]* (June 2009). arXiv: 0906.3884. URL: http://arxiv.org/abs/0906.3884 (visited on 08/05/2016).

[33] Miloch. "Numerical Studies of Charged Dust Particles in Plasmas". MA thesis. University of Oslo, 2006.

[34] W. J. Miloch et al. "Charging of insulating and conducting dust grains by flowing plasma and photoemission". In: *New Journal of Physics* 11.4 (2009), p. 043005. ISSN: 1367-2630. DOI: 10.1088/1367-2630/11/4/043005. URL: http://stacks.iop.org/1367-2630/11/i=4/a=043005 (visited on 09/26/2016).

[35] Wojciech J. Miloch. "Wake effects and Mach cones behind objects". In: *Plasma Physics and Controlled Fusion* 52.12 (2010), p. 124004. ISSN: 0741-3335. DOI: 10.1088/0741-3335/52/12/124004. URL: http://stacks.iop.org/0741-3335/52/i=12/a=124004 (visited on 09/22/2016).

[36] Yohei Miyake and Hideyuki Usui. "New electromagnetic particle simulation code for the analysis of spacecraft-plasma interactions". In: *Physics of Plasmas (1994-present)* 16.6 (June 1, 2009), p. 062904. ISSN: 1070-664X, 1089-7674. DOI: 10.1063/1.3147922. URL: http://scitation.aip.org/content/aip/journal/pop/16/6/10.1063/1.3147922 (visited on 09/23/2016).

[37] Y. Miyake et al. "Plasma particle simulations of wake formation behind a spacecraft with thin wire booms". In: *Journal of Geophysical Research: Space Physics* 118.9 (Sept. 1, 2013), pp. 5681–5694. ISSN: 2169-9402. DOI: 10.1002/jgra.50543. URL: http://onlinelibrary.wiley.com/doi/10.1002/jgra.50543/abstract (visited on 09/22/2016).

[38] *NASA Sounding Rockets User Handbook*. NASA Goddard Space Flight Center Wallops Flight Facility Wallops Island, VA 23337, July 2015. URL: http://sites.wff.nasa.gov/code810/files/SRHB.pdf.

[39] Hans L. Pécseli. *Waves and Oscillations in Plasmas*. English. 1 edition. Boca Raton: CRC Press, Sept. 2012. ISBN: 978-1-4398-7848-4.

[40] Gerd Prölss. *Physics of the Earth's space environment: an introduction*. Springer Science & Business Media, 2012.

[41] Hong Qin et al. "Why is Boris algorithm so good?" In: *Physics of Plasmas (1994-present)* 20.8 (Aug. 1, 2013), p. 084503. ISSN: 1070-664X, 1089-7674. DOI: 10.1063/1.4818428. URL: http://scitation.aip.org/content/aip/journal/pop/20/8/10.1063/1.4818428 (visited on 08/17/2016).

[42] Frank H. Shu. *The Physics of Astrophysics Volume II: Gas Dynamics*. First edition. University Science books, Oct. 15, 2009. 476 pp. ISBN: 978-1-891389-67-2.

[43] Randy J. Shul and Stephen J. Pearton, eds. *Handbook of Advanced Plasma Processing Techniques*. Berlin, Heidelberg: Springer Berlin Heidelberg, 2000. ISBN: 978-3-642-63096-5 978-3-642-56989-0. URL: http://link.springer.com/10.1007/978-3-642-56989-0 (visited on 09/28/2016).

[44] David A Vallado. *Fundamentals of astrodynamics and applications*. Vol. 12. Springer Science & Business Media, 2001.

[45] A. Whittlesey, H. B. Garrett, and P. A. Robinson. "The Satellite Space Charging Phenomenon, And Design And Test Considerations". In: *, IEEE 1992 International Symposium on Electromagnetic Compatibility, 1992. Symposium Record*. Aug. 1992, pp. 526–527. DOI: 10.1109/ISEMC.1992.626161.